nanomaterials

Review

One-, Two-, and Three-Dimensional Self-Assembly of Atomically Precise Metal Nanoclusters

Ayano Ebina [1], Sakiat Hossain [1], Hikaru Horihata [1], Shuhei Ozaki [1], Shun Kato [1], Tokuhisa Kawawaki [1,2,3] and Yuichi Negishi [1,2,3,*]

[1] Department of Applied Chemistry, Faculty of Science, Tokyo University of Science, Kagurazaka, Shinjuku-ku, Tokyo 162-8601, Japan; ayano0may9@gmail.com (A.E.); hisakiat@gmail.com (S.H.); konpei1082saikou@gmail.com (H.H.); shuheiozaki@icloud.com (S.O.); syunpeeee9@gmail.com (S.K.); kawawaki@rs.tus.ac.jp (T.K.)

[2] Research Institute for Science & Technology, Tokyo University of Science, Shinjuku-ku, Tokyo 162-8601, Japan

[3] Photocatalysis International Research Center, Tokyo University of Science, 2641 Yamazaki, Noda, Chiba 278-8510, Japan

[*] Correspondence: negishi@rs.tus.ac.jp

Received: 14 May 2020; Accepted: 27 May 2020; Published: 3 June 2020

Abstract: Metal nanoclusters (NCs), which consist of several, to about one hundred, metal atoms, have attracted much attention as functional nanomaterials for use in nanotechnology. Because of their fine particle size, metal NCs exhibit physical/chemical properties and functions different from those of the corresponding bulk metal. In recent years, many techniques to precisely synthesize metal NCs have been developed. However, to apply these metal NCs in devices and as next-generation materials, it is necessary to assemble metal NCs to a size that is easy to handle. Recently, multiple techniques have been developed to form one-, two-, and three-dimensional connected structures (CSs) of metal NCs through self-assembly. Further progress of these techniques will promote the development of nanomaterials that take advantage of the characteristics of metal NCs. This review summarizes previous research on the CSs of metal NCs. We hope that this review will allow readers to obtain a general understanding of the formation and functions of CSs and that the obtained knowledge will help to establish clear design guidelines for fabricating new CSs with desired functions in the future.

Keywords: metal cluster; one-dimensional connected structure; two-dimensional connected structure; three-dimensional connected structure; metal–organic framework; photoluminescence; electrical conductivity

1. Introduction

1.1. Metal Nanoclusters for Nanotechnology

Nanotechnology is technology to precisely manufacture small structures. In many countries, nanotechnology is being promoted as a national policy. Progress of nanotechnology allows information and functions to be integrated in smaller spaces, making it possible to manufacture devices with more functions at the same scale. In addition, since nanotechnology makes it possible to integrate the same function in a smaller volume than is the case for current devices, it is expected that devices will be downsized, which will increase their portability. This eliminates the need for the user to be dependent on the device location, which could solve the problems such as crowding and traffic jams and allow users to manage their time more effectively. In addition, the progress of nanotechnology has many advantages, such as saving resources and energy and decreasing waste and environmental damage [1].

Techniques to fabricate small materials can be roughly divided into two categories. One category is top-down methods, in which a desired structure is produced by decreasing the size of a larger substrate (Figure 1). Nanotechnology has been supported by the development of top-down methods. For example, increased functionality and miniaturization of electronic devices have been realized by the progress of top-down techniques. However, when a fine structure is manufactured by using tools (light, electron beam, scanning probe microscope, etc.), it is difficult to manufacture nanostructures with finer accuracy than that of the tools. Therefore, in recent years, bottom-up methods that assemble nanostructures from atoms and molecules have attracted attention (Figure 1) [1].

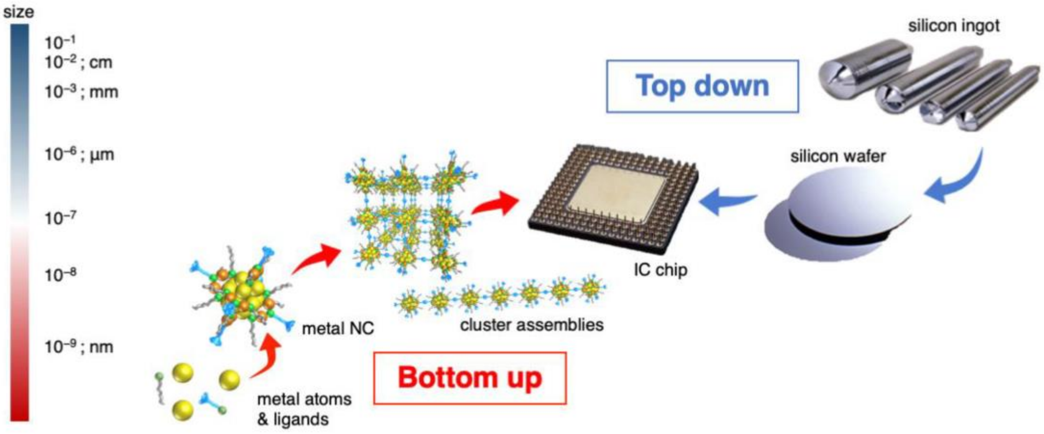

Figure 1. Fine processing techniques, including top-down (cyan) and bottom-up (red) methods. IC = integrated circuit.

Metal nanoclusters (NCs), which consist of several, up to about one hundred, metal atoms [1–10], are nanomaterials that can be synthesized by bottom-up methods. Metal NCs are not only small (<2 nm in size), but they also show physical/chemical properties and functions which are different from those of the corresponding bulk metals [11–35]. Furthermore, the physical/chemical properties and functions of metal NCs change considerably depending on the number of constituent atoms [36–65]. Therefore, if the number of constituent atoms of metal NCs is controlled, it is possible to produce various physical/chemical properties and functions by using only one type of metal element. If several types of elements can be used, it becomes possible to obtain more functionalities [66–82]. For these reasons, metal NCs have been attracting considerable attention as a central material in nanotechnology. In recent years, it has become possible to synthesize such metal NCs precisely at the atomic and molecular level by using thiolate (SR) [2,66], alkyne [59,83], phosphine [9,84–92], carbon monoxide [93–100], and dendrimers [7] as protective organic molecules. Investigation of the obtained precise metal NCs has revealed their geometrical structure (aggregation pattern of metal atoms) and the influences of miniaturization [1–65] and alloying [66–82] on the electronic structures and physical/chemical properties of metal NCs. In parallel, research on the applications of the optical properties and catalytic activity of metal NCs is being actively conducted [81,101–108].

1.2. Controlled Assembly of Metal Nanoclusters

As mentioned above, metal NCs show promise as constituent units of functional nanomaterials. Gold (Au) NCs have already been put to practical use in the fields of sensors, catalysts, and paints. On the other hand, at present, electronic devices are manufactured by top-down methods. Therefore, to replace the components of current devices with metal NCs, it is necessary to grow metal NCs to a size that allows their combination with structures manufactured by top-down methods. Moreover, in other applications, the small size of metal NCs often makes them difficult to handle. To realize nanodevices and next-generation materials with the advantageous characteristics of metal NCs, it is essential to establish techniques to assemble metal NCs to a size that makes them easy to handle.

To form a one-dimensional (1D) arrangement of metal NCs, templates [109,110] and host–guest interactions [111] are extremely effective. Two-dimensional (2D) and three-dimensional (3D) arrays of metal NCs can be fabricated by Langmuir–Blodgett [112] and alternate adsorption methods. There are many reports in which metal NCs are arranged in one, two, and three dimensions by using these methods. However, in the structures produced by these methods, the metal NCs are not regularly arranged in a strict sense. Since the conductivity (σ) of metal NCs changes exponentially with the length of the insulating organic ligands [113], the existence of a distribution in the distances between NCs (i.e., the length of the insulating part) is undesirable when applying the assembled metal NCs in electronic devices. Furthermore, although the Langmuir–Blodgett and alternate adsorption methods are suitable for arranging metal NCs in a wide size area, they are not suitable for arranging those in a tiny area.

Metal NCs are regularly arranged in single crystals. Therefore, it is possible to produce precise structures in which metal NCs are regularly connected in one, two, and three dimensions by crystallizing them while including an ingenious means to connect metal NCs. In fact, many crystals in which metal NCs are regularly linked by such a method have been reported in recent years. These structures contain strong bonds, such as Au−Au, Au−silver (Ag), Ag−oxygen (O), Ag−sulfur (S), Ag−chloride (Cl), Ag−nitrogen (N), cesium (Cs)−S, or hydrogen (H) bonds [114], and weak interactions, such as π−π, anion−π, cation···π, aryl CH···Cl, and van der Waals interactions [115] (Figure 2). Similar to supramolecules, molecular assemblies [116], and metal–organic frameworks (MOFs) [117] that are self-assembled from metal ions and organic molecules, connected structures (CSs) of metal NCs can be formed by self-assembly during crystallization, using these bonds and interactions. Such structures, which could also be called "suprametal NC crystals", exhibit physical/chemical properties different from those of an individual metal NC. Thus, the formation of CSs not only increases the size of the structure, but also enables the application of NCs in new fields.

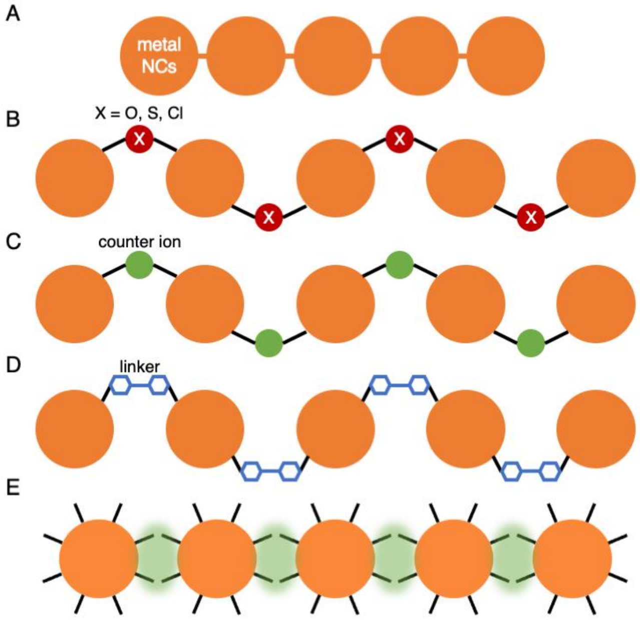

Figure 2. Representative methods for connecting metal NCs: (**A**) formation of metal−metal bond; (**B**) formation of Ag−O, Ag−S, and Ag−Cl bonds; (**C**) control of counterions; (**D**) introduction of linker molecules; and (**E**) use of inter-ligand interactions. In this review, 1D, 2D, and 3D CSs formed by inter-ligand interactions (**E**) are not introduced.

1.3. Contents of This Review

In recent years, it has become possible to control not only the geometrical structure of metal NCs, but also 1D, 2D, and 3D CSs of metal NCs. Further development of these techniques will lead to novel nanomaterials possessing the characteristics of metal NCs. Such development may enable a future in which metal NCs are applied in devices. However, since these studies have been initiated in recent years, there have been few review articles focusing on 1D, 2D, and 3D CSs of metal NCs [118,119].

In this review, we summarize the existing research, with the purposes of understanding the current situation regarding these structures and giving perspective regarding clear design for producing new 1D, 2D, and 3D CSs with desired functions.

This review is structured as follows. Section 2 outlines the fabrication of 1D CSs consisting of metal NCs, their geometrical structures, and physical/chemical properties. Then, Sections 3 and 4 present research on 2D and 3D CSs, respectively. After summarizing this review article in Section 5, a brief future outlook is described in Section 6.

It should be noted that 1D, 2D, and 3D CSs of metal NCs can be formed by methods other than crystallization [120,121]; for example, hydrophilic Au NCs have been arranged in 1D and 3D form by the Xie's group, although these NCs have not been crystallized. However, in this review, only the CSs of metal NCs in crystals are summarized, because our focus is on the regularly CSs in a strict sense. In addition, we described the synthesis methods only for the several examples. Thus, we recommend the readers who want to know the detail of synthesis methods for each example to refer to each original paper.

2. One-Dimensional Structures

The formation of 1D CSs composed of precise metal NCs is important from the viewpoint of the fabrication of controlled nanodevices by bottom-up methods. In this section, we introduce some typical examples of the construction of 1D CSs by the formation of metal–metal bonds (Figure 2A), formation of Ag–O bonds (Figure 2B), control of counterions (Figure 2C), and introduction of linker molecules (Figure 2D). The connection methods, NCs, linkers, year reported, and reference numbers of 1D CSs are summarized in Table 1. Chemical structures of some of the ligands used in these studies are shown in Scheme 1. The chemical structures of organic molecules used as linkers are illustrated in Scheme 2.

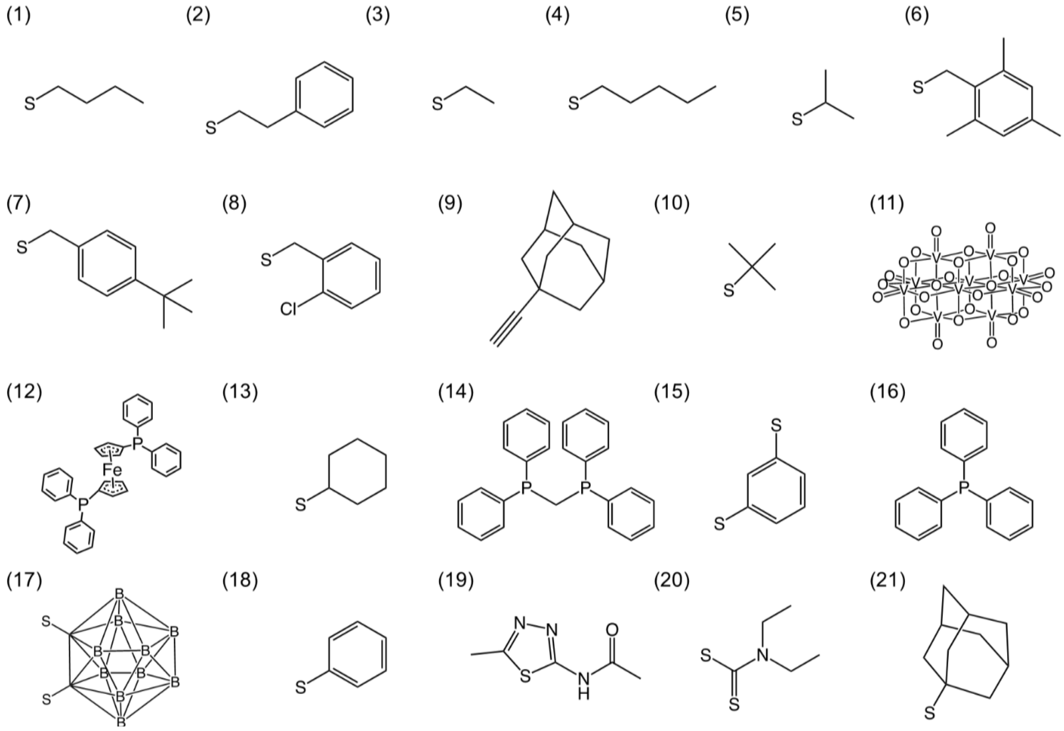

Scheme 1. Molecules used in the synthesis of metal NCs: (**1**) S-Bu, (**2**) PET, (**3**) S-Et, (**4**) S-Pen, (**5**) S-*i*Pr, (**6**) $SCH_2Ph(CH_3)_3$, (**7**) SCH_2Ph^tBu, (**8**) SCH_2PhCl, (**9**) A-Adm, (**10**) S-^{t}Bu, (**11**) $V_{10}O_{28}{}^{6-}$, (**12**) dppf, (**13**) S-*c*-C_6H_{11}, (**14**) DPPM, (**15**) BDT, (**16**) PPh_3, (**17**) DT-*o*-C, (**18**) S-Ph, (**19**) N-L, (**20**) $C_5NS_2H_{10}$, and (**21**) S-Adm.

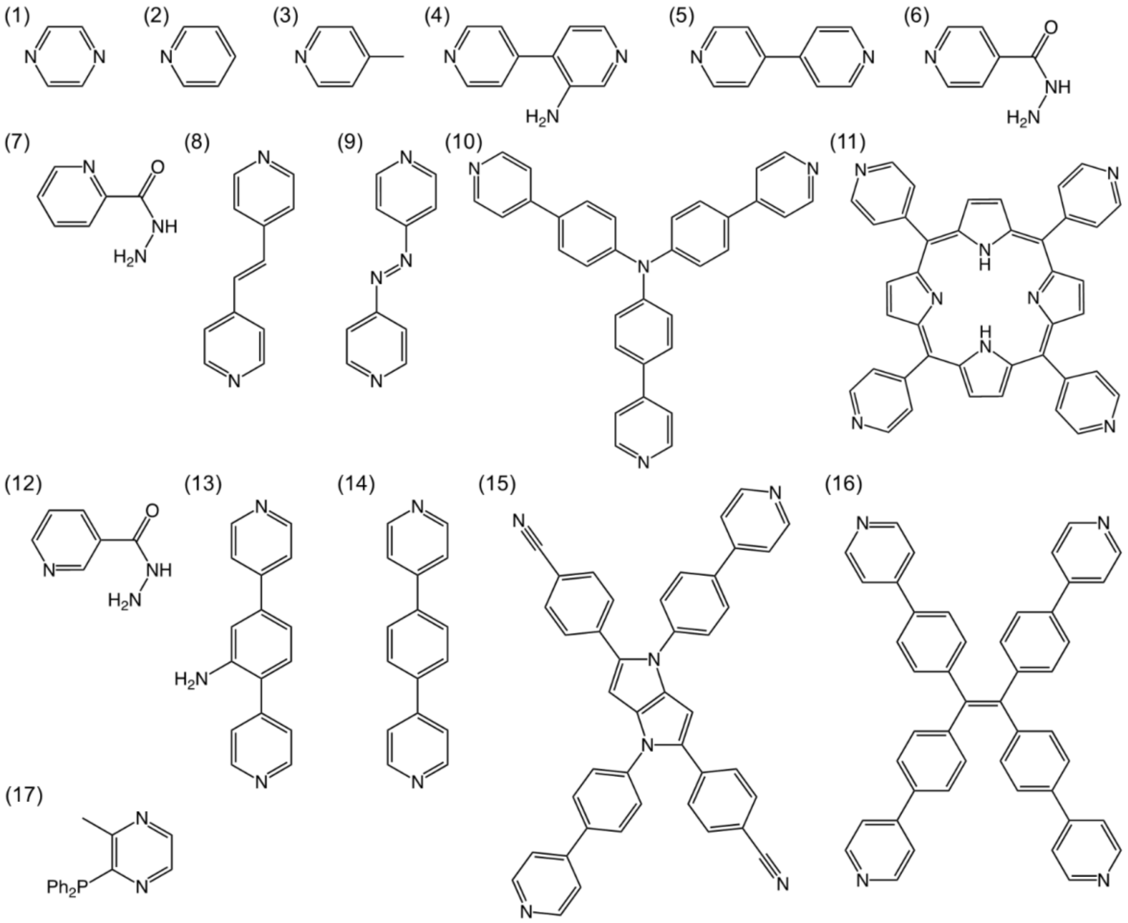

Scheme 2. Linker molecules used to connect metal NCs: (**1**) pyrazine, (**2**) pyridine, (**3**) *p*-methylpyridine, (**4**) bpy-NH_2, (**5**) bpy, (**6**) *p*-iah, (**7**) *o*-iah, (**8**) bpe, (**9**) dipyridin-4-yl-diazene, (**10**) TPPA, (**11**) TPyP, (**12**) *m*-iah, (**13**) bpz-NH_2, (**14**) 1,4-bis(4-pyridyl)benzene, (**15**) CPPP, (**16**) tppe, and (**17**) mdppz.

2.1. Direct Connection via Metal−Metal Bonds

In 2014, Maran et al. [122] fabricated a 1D CS composed of an SR-protected Au 25-atom NC ($[Au_{25}(SR)_{18}]^0$). Since $Au_{25}(SR)_{18}$ NCs exhibit high stability among $Au_n(SR)_m$ NCs, their geometrical/electronic structures and physical/chemical properties have been studied extensively [18,27,123–139]. However, because most of the studies were conducted on $Au_{25}(SR)_{18}$ in solution and there had been few studies on $Au_{25}(SR)_{18}$ in the solid phase, Maran's group studied the behavior of $Au_{25}(SR)_{18}$ in the solid state.

In their study, butanethiolate (S-Bu, Scheme 1(1)) was used as the SR ligand. First, $[Au_{25}(\text{S-Bu})_{18}]^-$ anion was synthesized by reducing the Au(I)- S-Bu complex by using sodium borohydride ($NaBH_4$). Then, $[Au_{25}(\text{S-Bu})_{18}]^-$ anion was oxidized into neutral $[Au_{25}(\text{S-Bu})_{18}]^0$ in open column packed with silica gel, and single crystals were grown by slow evaporation. Figure 3A(a) shows the geometrical structure of $[Au_{25}(\text{S-Bu})_{18}]^0$ obtained by single-crystal X-ray diffraction (SC-XRD). Each $[Au_{25}(\text{S-Bu})_{18}]^0$ has almost the same framework structure as that of $[Au_{25}(SR)_{18}]^0$ protected by other SR ligands; e.g., phenylethanethiolate (PET, Scheme 1(2)) and ethanethiolate (S-Et, Scheme 1(3)) (Figure 3A(b)) [27,53]. However, Au−Au bonds formed between adjacent NCs in the $[Au_{25}(\text{S-Bu})_{18}]^0$ crystal, unlike the case for other $[Au_{25}(SR)_{18}]^0$ crystals (Figure 3A(a),B(a)). This indicates that $[Au_{25}(\text{S-Bu})_{18}]^0$ is a suitable structural unit to form 1D CSs. The Au−Au distance between adjacent NCs of 3.15 Å was within the range of aurophilic interactions (2.9−3.5 Å) and shorter than the non-bonding Au−Au distance (3.80 Å) estimated from the van der Waals radius of Au. This result indicates that a 1D CS was formed in the crystal structure of $[Au_{25}(\text{S-Bu})_{18}]^0$ via Au−Au bonds. To form such a 1D CS, it was considered that the repulsion between the ligands was suppressed and an attractive force between the ligands was induced because the adjacent NCs twisted and approached each other (twist-and-lock mechanism). It was suggested that 1D CSs did not form when S-Et and PET were used (Figure 3A(b),B(b)) because S-Et has a short alkyl group that leads to a weak attractive force between ligands and PET with a bulky functional group has large steric repulsion between ligands. In 2017, these researchers also succeeded in forming a 1D CS of $[Au_{25}(S\text{-}Pen)_{18}]^0$ (S-Pen = pentanethiolate, Scheme 1(4)) [140]. In the same paper, they reported that the distance between NCs was shorter in this 1D CS than in the 1D CS of $[Au_{25}(S\text{-}Bu)_{18}]^0$ (Figure 3C). In addition, in 2019, they formed 1D CSs of $[Au_{24}Hg(S\text{-}Bu)_{18}]^0$ (Hg = mercury) and $[Au_{24}Cd(S\text{-}Bu)_{18}]^0$ (Cd = cadmium), in which one Au of $[Au_{25}(S\text{-}Bu)_{18}]^0$ was replaced with Hg or Cd [141].

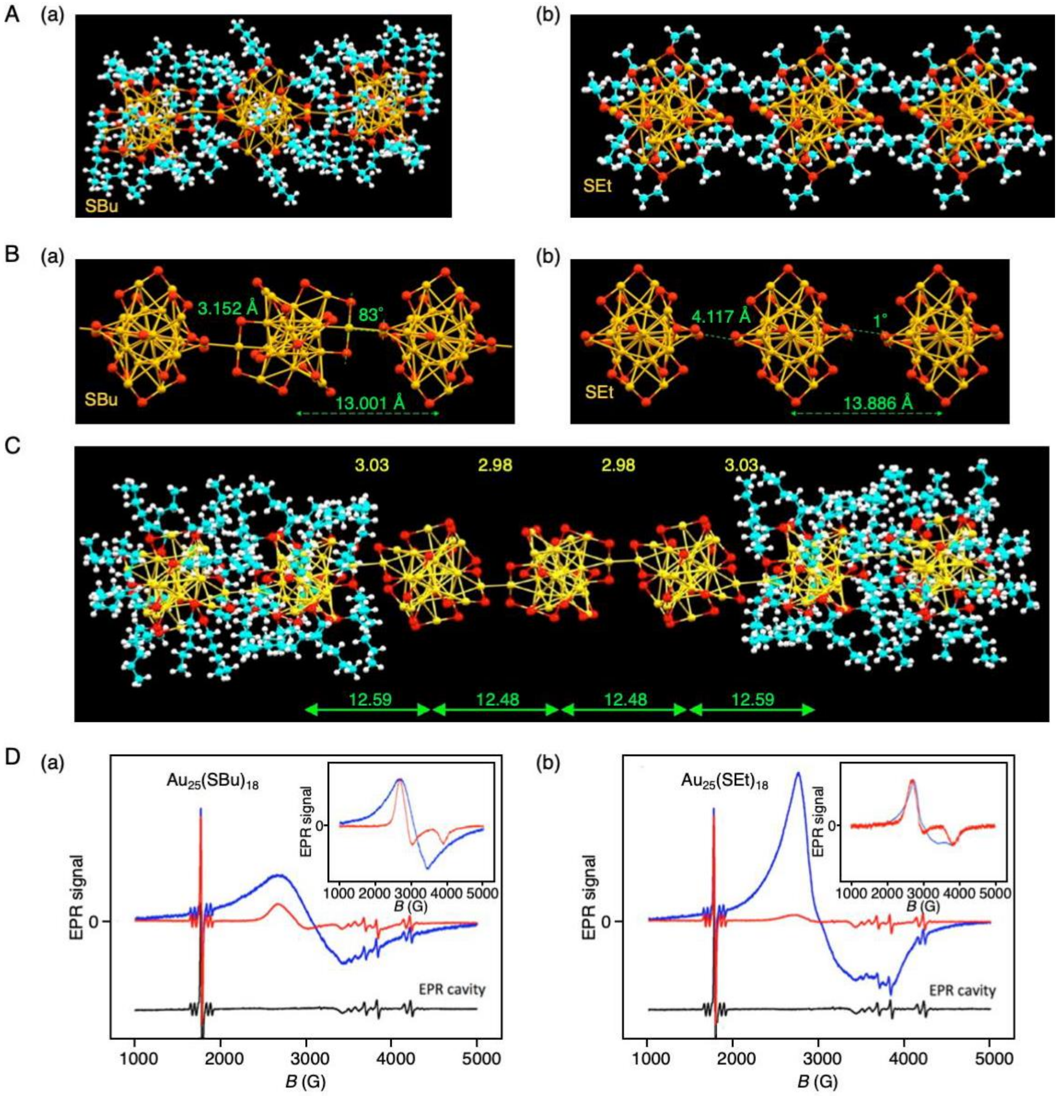

Figure 3. (**A**,**B**) Crystal structures of (a) $[Au_{25}(S\text{-}Bu)_{18}]^0$ and (b) $[Au_{25}(S\text{-}Et)_{18}]^0$. In (**B**), R groups are omitted for clarity. (**C**) Crystal structure of $[Au_{25}(S\text{-}Pen)_{18}]^0$. In (A–C), Au = yellow, S = red, C = light blue, and H = white. (**D**) Comparison of the continuous wave-electron paramagnetic resonance (EPR) spectra of solid (blue traces) and frozen toluene solution (red traces) for (a) $[Au_{25}(S\text{-}Bu)_{18}]^0$ and (b) $[Au_{25}(S\text{-}Et)_{18}]^0$ at −253 °C. The inset shows the same spectra with normalized peak intensity. The black curve corresponds to the EPR cavity signal, which is subtracted in the inset for clarity. All spectra were obtained by using the following parameters: microwave frequency = 9.733 GHz; microwave power = 150 µW; amplitude modulation = 1 G. Reproduced with permission from References [122,140]. Copyright 2014 American Chemical Society and 2017 American Chemical Society.

The same group also revealed that the 1D CSs had electronic structures and physical properties different from those of individual NCs. Since $[Au_{25}(S\text{-}Bu)_{18}]^0$ has unpaired electrons, it exhibits paramagnetism in solution. Conversely, the 1D CS of $[Au_{25}(S\text{-}Bu)_{18}]^0$ was non-magnetic (Figure 3D) [122]. This change was mainly ascribed to the formation of the 1D CS, which led to the close proximity of NCs, allowing the unpaired electrons of adjacent NCs to form electron pairs. Because of the formation of such electron pairs, the conduction band of the 1D CS was full and its valence band was empty, so the obtained 1D CS was predicted to have the properties of a semiconductor [122].

In 2020, we [142] conducted a detailed study on the factors responsible for the formation of 1D CSs via Au−Au bonds by using $[Au_4Pt_2(SR)_8]^0$ (Pt = platinum) as the NC. A similar NC, $[Au_4Pd_2(PET)_8]^0$ (Pd = palladium), was reported by Wu and colleagues in 2017 (Figure 4) [143]. Although it was not mentioned in their paper, $[Au_4Pd_2(PET)_8]^0$ formed a 1D CS in its crystal (Figure 4). Because this type of metal NC has a smaller metal core than that of $[Au_{25}(SR)_{18}]^0$ described above (Figure 4), the distribution of the ligands in this type of NC should change depending on the ligand structure. Moreover, Au and Pt form a stronger bond than that between Au and Pd [144]. Therefore, it was expected that changing Pd to Pt would increase the stability of the NC [145], thereby expanding the variety of ligand functional group structures that can be used in 1D CSs. For these reasons, we chose $[Au_4Pt_2(SR)_8]^0$ as the building block of their 1D CS. The SR ligands shown in Scheme 1(2),(5)–(8) were used. Because the functional group structures of these SR ligands differ greatly, it was expected that there would be different ligand–ligand interactions between the resulting NCs.

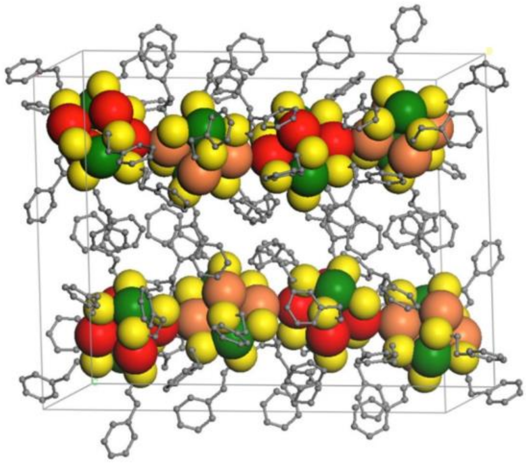

Figure 4. Crystal unit cell of $[Au_4Pd_2(PET)_8]^0$. S = yellow, Au = red and orange, Pd = olive, C = gray. Reproduced with permission from Reference [143]. Copyright 2017 Wiley-VCH.

In the experiment, $[Au_4Pt_2(SR)_8]^0$ NCs with different SRs were precisely synthesized by reducing the metal−SR complex with $NaBH_4$. Each $[Au_4Pt_2(SR)_8]^0$ NC was separated from by-products, using open column chromatography, and then single crystals were grown by vapor diffusion. The SC-XRD of the series of $[Au_4Pt_2(SR)_8]^0$ crystals revealed the following three points for $[Au_4Pt_2(SR)_8]^0$: (1) $[Au_4Pt_2(SR)_8]^0$ is a metal NC that can become a structural unit of 1D CSs via Au−Au bond formation (Figure 5A); (2) although all $[Au_4Pt_2(SR)_8]^0$ NCs have similar structures, the intra-cluster ligand interactions vary depending on the ligand structure. As a result, the distribution of the ligands in $[Au_4Pt_2(SR)_8]^0$ changes depending on the ligand structure; (3) the differences in the ligand distributions influence the inter-cluster ligand interactions, which in turn affect the formation of 1D CSs and change their structure (Figure 5B). These results demonstrate that we need to design intra-cluster ligand interactions, to produce 1D CSs with desired configurations. This study also explored the effects of 1D CS formation on the electronic structure of NCs. The results revealed that the formation of the 1D CS caused the band gap of the NCs to decrease (Figure 5C,D) [142].

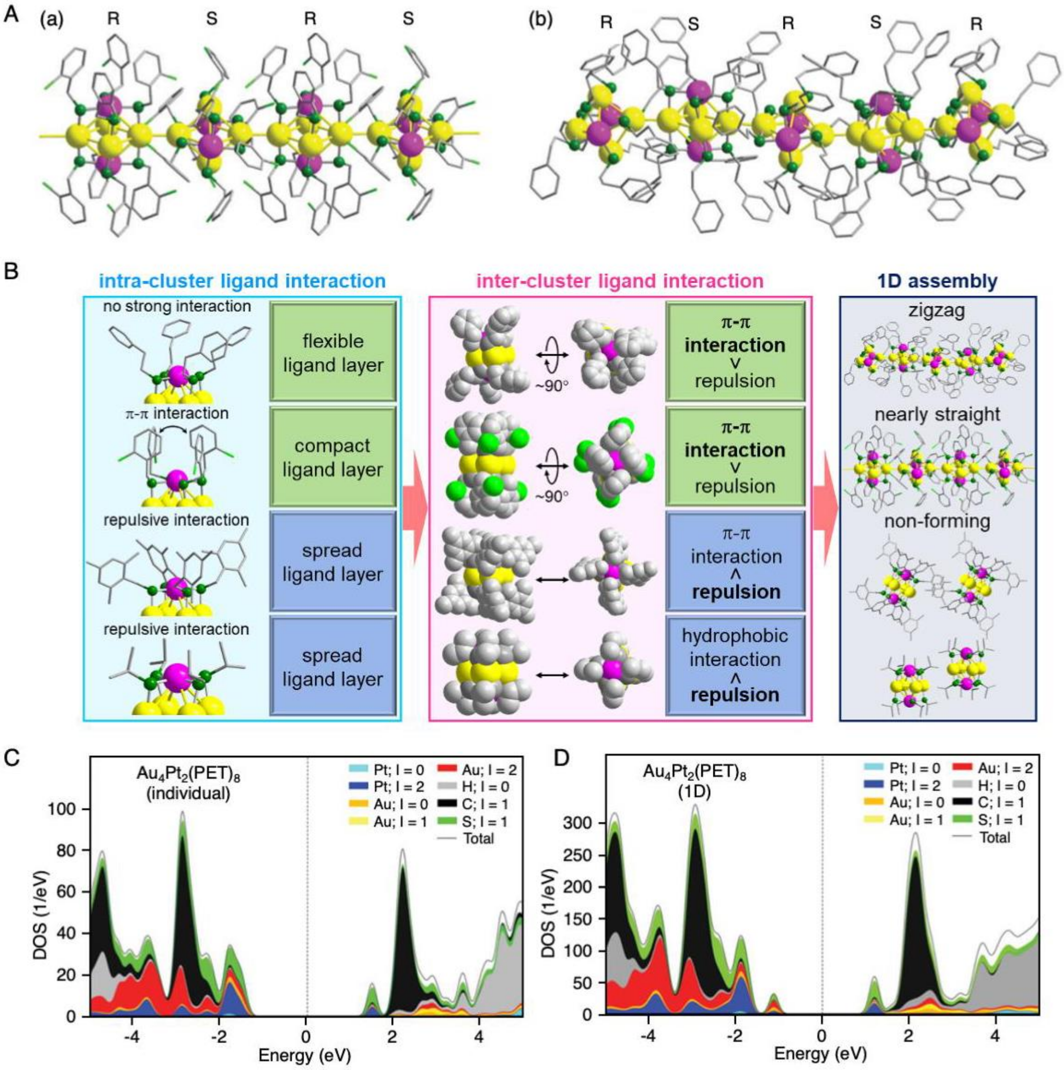

Figure 5. (**A**) Crystal unit cells of (a) $[Au_4Pt_2(SCH_2PhCl)_8]^0$ and (b) $[Au_4Pt_2(PET)_8]^0$. Au = yellow, Pt = magenta, S = green, Cl = light green, C = gray. R and S indicate two enantiomers in each NC. (**B**) Relationships between intra-cluster ligand interactions, which are related to the distribution of the ligands within each cluster, inter-cluster ligand interactions, and 1D assembly. Projected density of states of (**C**) an individual $[Au_4Pt_2(PET)_8]^0$ NC and (**D**) the 1D CS of $[Au_4Pt_2(PET)_8]^0$. Reproduced with permission from Reference [142]. Copyright 2020 Royal Society of Chemistry.

Zhang et al. also very recently reported the formation of 1D CS consisting of the $(AuAg)_{34}(A\text{-}Adm)_{20}$ alloy NCs (A-Adm = 1-ethynyladamantane; Scheme 1(9)) [146]. For $(AuAg)_{34}(A\text{-}Adm)_{20}$ alloy NCs, either monomeric NC or 1D CSs were formed depending on the solvent. Monomeric NC could be converted to 1D CSs by dissolving in an appropriate solvent. In the 1D CS, NCs were connected each other via Ag−Au−Ag bond (Figure 6A,B). They studied the electronic structure of the obtained 1D CS by density functional theory (DFT) calculations, which predicted that the single crystals of 1D CS have a band gap of about 1.3 eV (Figure 6C). Field-effect transistors (FETs) fabricated with single crystals of 1D CS (Figure 6D) showed highly anisotropic *p*-type semiconductor properties with ~1800-fold conductivity in the direction of the polymer as compared to cross directions (Figure 6E), hole mobility of ≈0.02 cm^2/Vs, and an ON/OFF ratio up to ~4000. They noted that the conductivity (1.49×10^{-5} S/m) of these crystals in the *c*-crystallographic axis is one-to-three orders of magnitude higher than the values reported for 1D CS consisting of Au_{21} clusters, where 1D CS was formed by modulating the weak interactions in the ligand layers (see Section 2.3). It was interpreted that the conductivity and charge carrier mobility was increased by several orders of magnitude in their 1D CS via direct linking of the metal NCs by the –Ag–Au–Ag– chains in the crystal. They described in this paper that this result holds promise for further design of functional cluster-based materials with highly anisotropic semiconducting properties.

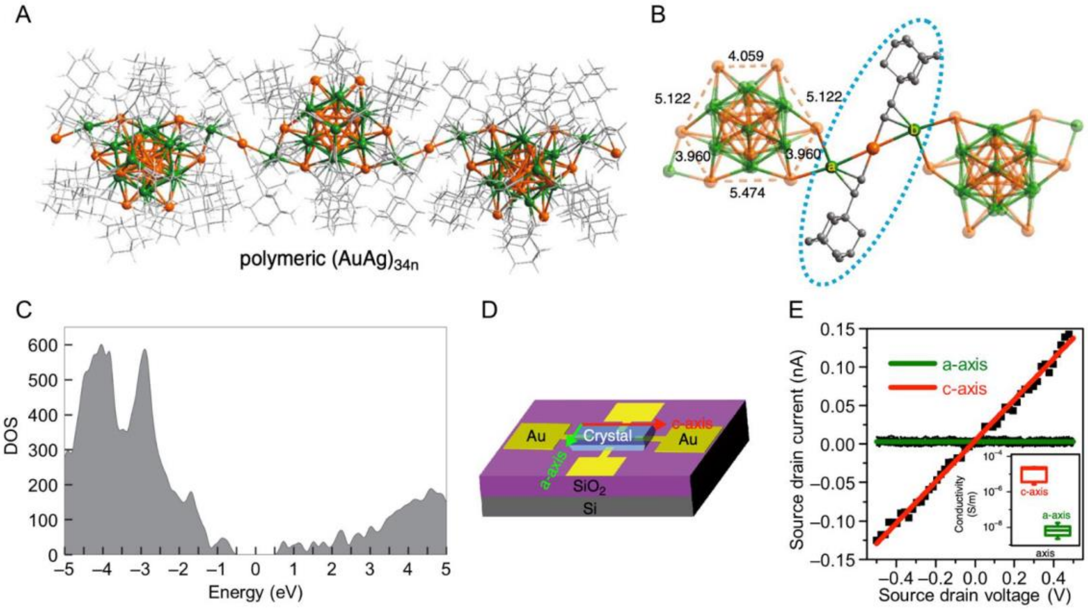

Figure 6. (**A**) Structures of the cluster polymer (approximately orthogonal to the *c*-axis). (**B**) Au–Au distances in the distorted Au_6 hexagon and Ag–Ag distance in the "Ag–Au–Ag" unit of between alloy NCs. Au/Ag = golden and green, C = gray. All hydrogen atoms are omitted for clarity. (**C**) DFT-computed electronic density of states (DOS) of the cluster polymer crystal. Cluster model was used to build the periodic crystal, and the integration over the Brilloin zone was done in a 4 × 4 × 4 Monkhorst–Pack *k*-point mesh. The band gap is centered around zero. (**D**,**E**) Electrical transport properties of the cluster polymer crystals; (**D**) structure of the polymer crystal FET; (**E**) *I*–*V* plot of the polymer crystal along *a*-axis and *c*-axis, respectively, with the range of corresponding conductivity values shown in the inset. Reproduced with permission from Reference [146]. Copyright 2020 Springer-Nature.

2.2. Connection via Ag−O Bonds

When Ag NCs contain acetic acid ions (CH_3COO^-), trifluoroacetic acid ions (CF_3COO^-), or nitrate ions (NO_3^-) in the ligand layer, it is possible to connect Ag NCs by forming Ag−O bonds. Su et al. [147] first reported the formation of such a 1D CS in 2014. In this study, the 1D CS was obtained by crystallization of the product which was obtained by the reaction between AgS-^{t}Bu, $(NH_4)_3[CrMo_6O_{24}H_6]$ (Cr = chromium, Mo = molybdenum), $Ni(CH_3COO)_2$ (Ni = nickel), $AgCF_3COO$, and $AgBF_4$. The each Ag NC had a chemical composition of $Ag_{20}(CO_3)(S\text{-}^tBu)_{10}(CH_3COO)_8(DMF)_2$ (CO_3^{2-} = carbonate anion; S-^{t}Bu = *tert*-butylthiolate, Scheme 1(10), DMF = *N*,*N*-dimethylformamide). The $Ag_{20}(CO_3)$ core of the NC was formed by the aggregation of Ag around CO_3^{2-} (Figure 7A) as an anion template. In the crystal, the Ag NCs were connected in one dimension via two Ag−O−Ag bonds (Figure 7B). The obtained 1D CS was stable in both solid and solution states, had a bandgap of 3.22 eV, and exhibited reversible thermochromic emission.

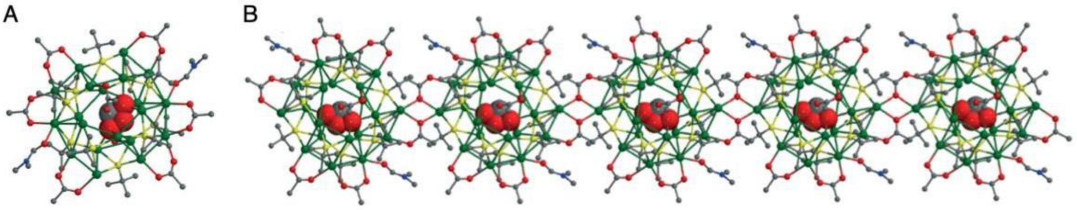

Figure 7. (**A**) Structure of $Ag_{20}(CO_3)(S\text{-}^tBu)_{10}(CH_3COO)_8(DMF)_2$. (**B**) Ball-and-stick view of the 1D chain of $Ag_{20}(CO_3)(S\text{-}^tBu)_{10}(CH_3COO)_8(DMF)_2$. Ag = green, S = yellow, N = blue, O = red, C = gray. Reproduced with permission from Reference [147]. Copyright 2014 Royal Society of Chemistry.

Formation of 1D CSs based on a similar principle was also reported by Mak and co-workers in 2017 [148]. In their report, $Ag_{18}(CO_3)(S\text{-}^tBu)_{10}(NO_3)_6(DMF)_4$ was linked by the formation of Ag−O bonds (Figure 8). The $Ag_{18}(CO_3)$ core contained CO_3^{2-} as an anion template at the center, like $Ag_{20}(CO_3)$. As described in Section 3.1, this group also succeeded in forming a 2D CS of $Ag_{20}(CO_3)$ by changing the SR structure.

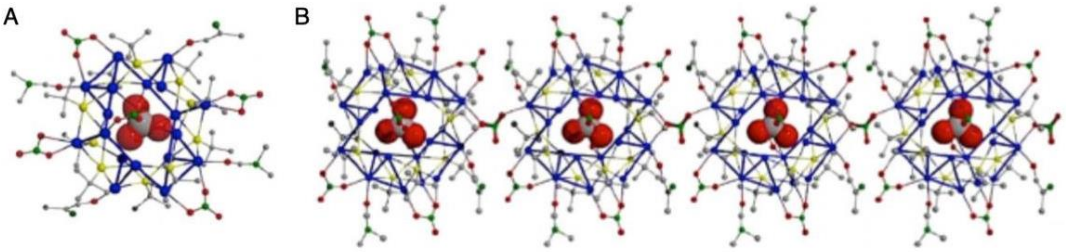

Figure 8. (**A**) Structure of $Ag_{18}(CO_3)(S\text{-}^tBu)_{10}(NO_3)_6(DMF)_4$. (**B**) Ball-and-stick view of the 1D chain of $Ag_{18}(CO_3)(S\text{-}^tBu)_{10}(NO_3)_6(DMF)_4$. Ag = blue, S = yellow, O = red, C = gray, N = green. Reproduced with permission from Reference [148]. Copyright 2017 Wiley-VCH.

Recently, Sun et al. [149] succeeded in the connection of $Ag_{44}(V_{10}O_{28})(S\text{-Et})_{20}(PhSO_3)_{18}(H_2O)_2$ ($V_{10}O_{28}^{6-}$, Scheme 1(11), $PhSO_3^-$ = benzenesulfonic acid ion). In this 1D CS, the $Ag_{44}(V_{10}O_{28})$ core was formed by using the polyoxometalate (POM) $V_{10}O_{28}^{6-}$ as an anion template (Figure 9A). This was the first report of the formation of a structure in which $V_{10}O_{28}^{6-}$ was covered with an Ag NC with SR as a ligand. This 1D CS assembled because two Ag−O bonds were formed between two $PhSO_3^-$ in the ligand layer and one $Ag_{44}(V_{10}O_{28})(S\text{-Et})_{20}$ NC (Figure 9B).

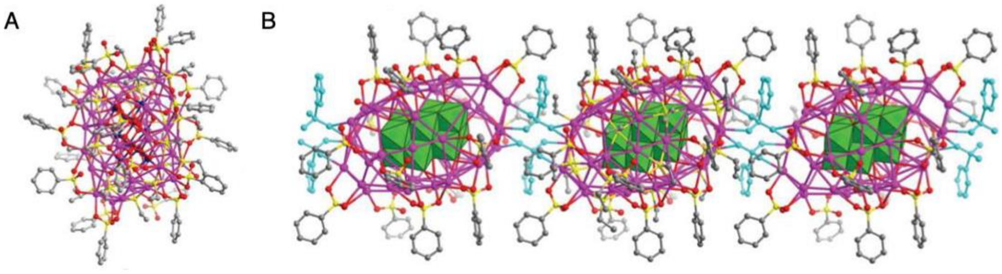

Figure 9. (**A**) Structure of $Ag_{44}(V_{10}O_{28})(S\text{-Et})_{20}(PhSO_3)_{18}(H_2O)_2$ (**B**) 1D chain structure of $Ag_{44}(V_{10}O_{28})(S\text{-Et})_{20}(PhSO_3)_{18}(H_2O)_2$ with all bridging $PhSO_3^-$ ligands highlighted in cyan and $V_{10}O_{28}^{6-}$ anions shown as green polyhedra. Ag = purple, V = dark blue, S = yellow, C = gray, O = red. All H atoms are omitted. Reproduced with permission from Reference [149]. Copyright 2019 Royal Society of Chemistry.

In the 1D CS of $[Au_7Ag_9(dppf)_3(CF_3COO)_7BF_4]_n$ (dppf = 1,1′-bis(diphenylphosphino)ferrocene, Scheme 1(12), BF_4 = tetrafluoroboric acid) reported by Wang et al. [150] in 2019, each NC was also connected via an Ag−O bond (Figure 10A), although this was not direct connection of metal NCs. In the above three NCs (i.e., $Ag_{20}(CO_3)(S\text{-}^tBu)_{10}(CH_3COO)_8(DMF)_2$, $Ag_{18}(CO_3)(S\text{-}^tBu)_{10}(NO_3)_6(DMF)_4$, and $Ag_{44}(V_{10}O_{28})(S\text{-}Et)_{20}(PhSO_3)_{18}(H_2O)_2$), the anion template was contained in the center, whereas $Au_7Ag_8(dppf)_3(CF_3COO)_7$ had an icosahedral metal core composed of Au_7Ag_8. Such an icosahedral core structure is often seen in metal NCs [27,53]. The 1D CS of $[Au_7Ag_9(dppf)_3(CF_3COO)_7BF_4]_n$ was synthesized in one pot. Probably, excess Ag binds to CF_3COO^- in the ligand layer during synthesis, resulting in the formation of a 1D CS composed of $Au_7Ag_8(dppf)_3(CF_3COO)_7$ NCs. The researchers also revealed that this 1D CS possessed a band gap of 2.18 eV (Figure 10B).

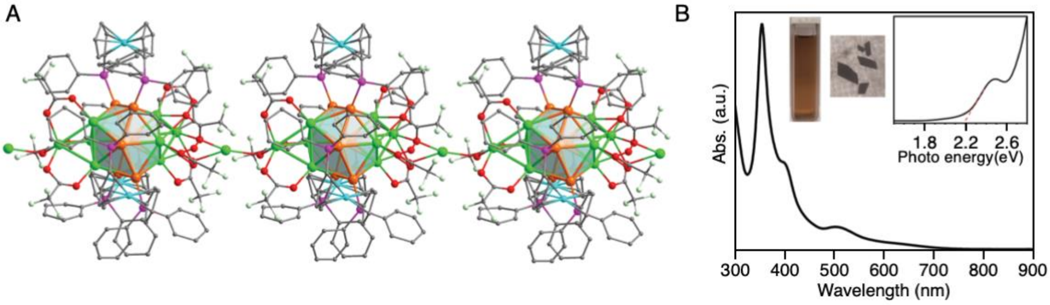

Figure 10. (**A**) View of the whole structure of $[Au_7Ag_9(dppf)_3(CF_3COO)_7BF_4]_n$ (anions and H atoms are omitted for clarity). Ag = green, Au = orange, O = red, P = purple, C = gray, Fe = blue. (**B**) Absorption spectrum of $[Au_7Ag_9(dppf)_3(CF_3COO)_7BF_4]_n$ in CH_2Cl_2 solution. Inset: absorption spectrum on the energy scale (eV) and photographs showing actual colors of $[Au_7Ag_9(dppf)_3(CF_3COO)_7BF_4]_n$ in CH_2Cl_2 and the crystalline state. Reproduced with permission from Reference [150]. Copyright 2019 Royal Society of Chemistry.

2.3. *Control of Counterions*

For certain metal NCs, the total number of valence electrons satisfies the number for the closed-shell electronic structure when it is a cation, so they are generated as a cation [151]. For example, $[Au_{21}(S\text{-}c\text{-}C_6H_{11})_{12}(DPPM)]^+$ ($S\text{-}c\text{-}C_6H_{11}$ = cyclohexanethiolate, Scheme 1(13), and DPPM = bis(diphenylphosphinomethane), Scheme 1(14)) is synthesized as a cation. In 2018, Jin et al. [152] revealed that $[Au_{21}(S\text{-}c\text{-}C_6H_{11})_{12}(DPPM)]^+$ formed a 1D CS in a crystal by assembling as a pair with the counter anion and that the structure of the 1D CS changed depending on the counterion (Figure 11A,B).

In this study, $[Au_{21}(S\text{-}c\text{-}C_6H_{11})_{12}(DPPM)_2]^+[AgCl_2]^-$ and $[Au_{21}(S\text{-}c\text{-}C_6H_{11})_{12}(DPPM)_2]^+[Cl]^-$ were precisely synthesized and single crystals were grown. As shown in Figure 11B, a 1D CS was formed by the alternating connection of $[Au_{21}(S\text{-}c\text{-}C_6H_{11})_{12}(DPPM)_2]^+$ and $[AgCl_2]^-$ in the $[Au_{21}(S\text{-}c\text{-}C_6H_{11})_{12}(DPPM)_2]^+[AgCl_2]^-$ crystal. This 1D CS was considered to assemble via π-π, anion-π, and aryl C-H···Cl interactions. The connection pattern of $[Au_{21}(S\text{-}c\text{-}C_6H_{11})_{12}(DPPM)_2]^+$ in the 1D CS changed slightly when the counterion was Cl^- rather than $[AgCl_2]^-$. It was considered that the connection pattern of $[Au_{21}(S\text{-}c\text{-}C_6H_{11})_{12}(DPPM)_2]^+$ changed because the arrangement of phenyl groups in the NC was affected by the counterion (Figure 11A).

The obtained 1D CSs of $[Au_{21}(S\text{-}c\text{-}C_6H_{11})_{12}(DPPM)_2]^+$ had different electron transport properties depending on the counter anion. The 1D CS of $[Au_{21}(S\text{-}c\text{-}C_6H_{11})_{12}(DPPM)_2]^+[AgCl_2]^-$ had a σ of only ~1.44×10^{-8} S/m, whereas that of $[Au_{21}(S\text{-}c\text{-}C_6H_{11})_{12}(DPPM)_2]^+[Cl]^-$ was σ ~2.38×10^{-6} S/m (Figure 11C). Changing the counter anion from $[AgCl_2]^-$ to $[Cl]^-$ shortened the distance between NCs from 16.80 to 16.39 Å and formed an intra-cluster π-stacking structure that allowed electricity to flow easily (Figure 11B). These two reasons explained why σ of $[Au_{21}(S\text{-}c\text{-}C_6H_{11})_{12}(DPPM)_2]^+[Cl]^-$ was two orders of magnitude higher than that of $[Au_{21}(S\text{-}c\text{-}C_6H_{11})_{12}(DPPM)_2]^+[AgCl_2]^-$ (Figure 11D).

There are not only metal NCs synthesized as cations but also metal NCs synthesized as anions. Because the total number of valence electrons of $[Ag_{29}(BDT)_{12}(PPh_3)_4]^{3-}$ (BDT = 1,3-benzenedithiolate, Scheme 1(15); PPh_3 = triphenylphosphine, Scheme 1(16)) satisfies the number for a closed-shell electronic structure as the anion, it is generated as the anion [153]. In 2019, Zhu et al. [154] reported that mixing this NC with Cs acetate in DMF induced Cs^+ attachment to the NC and PPh_3 desorption from the NC, resulting in the formation of $[Cs_3Ag_{29}(BDT)_{12}(DMF)_x]^0$ (x = 5 or 6) and that the obtained $[Cs_3Ag_{29}(BDT)_{12}(DMF)_x]^0$ formed a 1D CS in its crystal. Figure 12A shows the resulting 1D CS. In the crystal, $[Cs_3Ag_{29}(BDT)_{12}(DMF)_x]^0$ was connected by a series of bonds consisting of $-Cs^+-DMF-Cs^+-S-Ag-Ag-S-$. This 1D CS was considered to be formed because of the electrostatic attraction between $[Ag_{29}(BDT)_{12}(DMF)_x]^{3-}$ and Cs^+, Cs–S bond formation, and Cs···π interactions (Figure 12B).

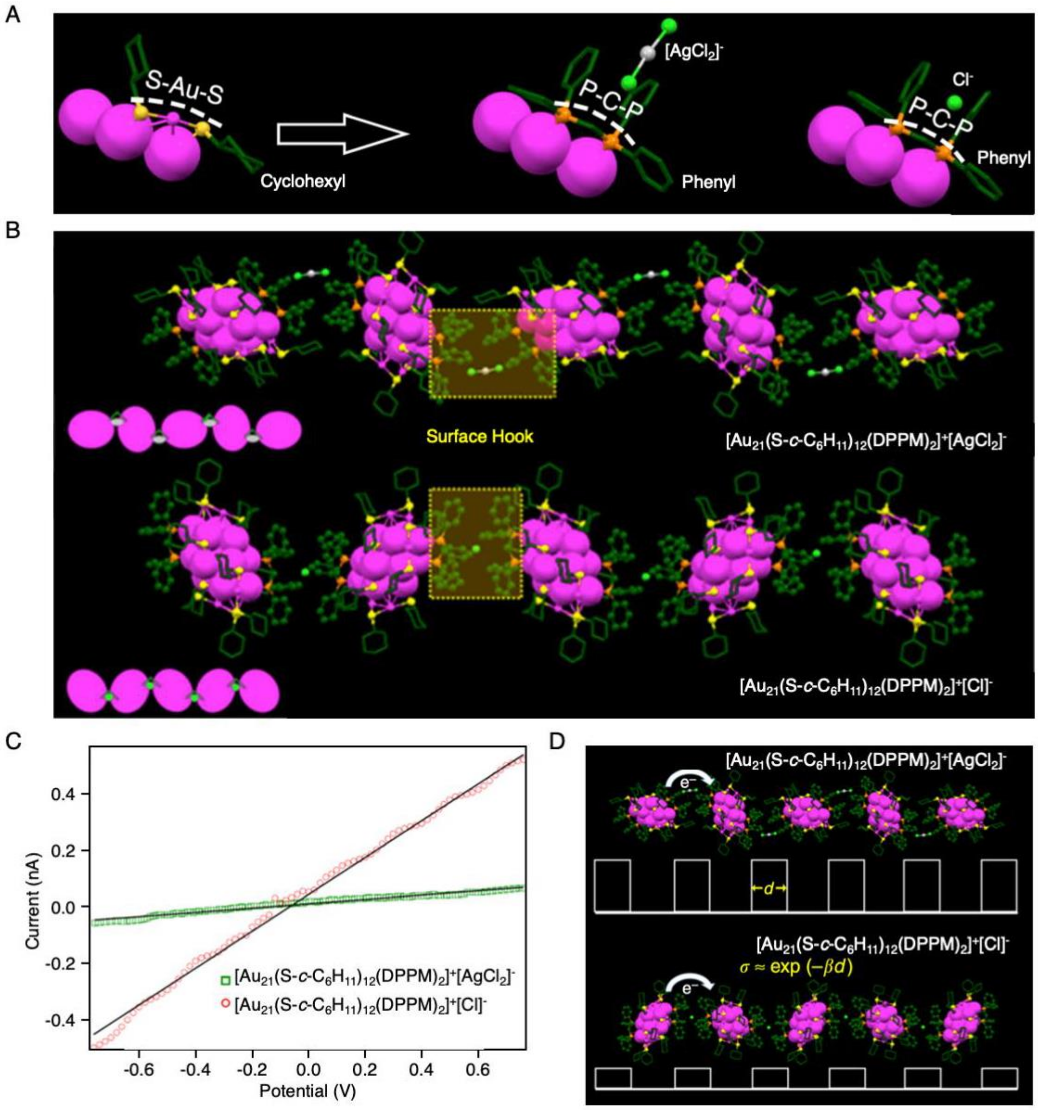

Figure 11. (**A**) Site-specific tailoring of the surface motifs and associated counterions of Au NCs. The two RS-Au-SR (R is cyclohexyl) surface motifs in Au_{23} (precursor NC) were replaced by two DPPM motifs in Au_{21}. Each P atom was connected to two phenyl rings. Dashed lines indicate the motifs. (**B**) Packing of $[Au_{21}(S\text{-}c\text{-}C_6H_{11})_{12}(DPPM)_2]^+[AgCl_2]^-$ and $[Au_{21}(S\text{-}c\text{-}C_6H_{11})_{12}(DPPM)_2]^+[Cl]^-$ in their 1D assemblies. The orientation of Au NCs is modulated by the counterion. Au = magenta, Ag = gray, Cl = light green, S = yellow, P = orange, C = green. All H atoms are omitted for clarity. Yellow areas are the surface hooks connecting neighboring NCs. (**C**) Room-temperature conductivity of single crystals of $[Au_{21}(S\text{-}c\text{-}C_6H_{11})_{12}(DPPM)_2]^+[AgCl_2]^-$ (green) and $[Au_{21}(S\text{-}c\text{-}C_6H_{11})_{12}(DPPM)_2]^+[Cl]^-$ (red). (**D**) Schematic diagram of electron hopping in Au_{21} NC assemblies. Different configurations of the interacting π–π pairs result in tunneling barriers of different heights (white solid squares), thus changing the electron conductivity (e^- represents an electron, σ is the conductivity, d is the interparticle distance, and β is the tunneling decay constant). Reproduced with permission from Reference [152]. Copyright 2018 Springer-Nature.

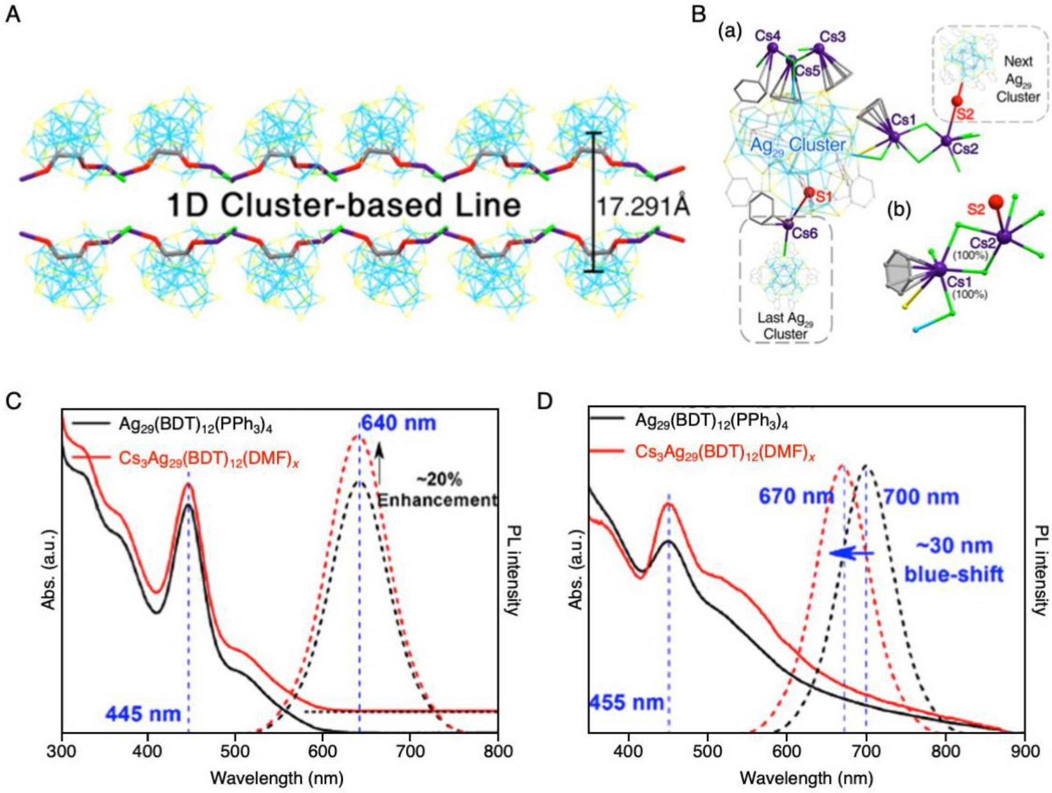

Figure 12. (**A**) 1D linear assembly of $[Cs_3Ag_{29}(BDT)_{12}(DMF)_x]^0$ in the crystal lattice. Ag = light blue/gray, Cs = dark purple, S = yellow and red, O = green. For clarity, all H, C, and N atoms, some Cs^+, and DMF molecules are omitted. Each O atom represents a DMF molecule. (**B**) (a) Overall surface structure of $[Cs_3Ag_{29}(BDT)_{12}(DMF)_x]^0$ and (b) interactions between $Ag_{29}(BDT)_{12}$, Cs_1, Cs_2, and DMF. (**C**) Comparison of optical absorption and emission spectra of $Ag_{29}(BDT)_{12}(PPh_3)_4$ (black) and $Cs_3Ag_{29}(BDT)_{12}(DMF)_x$ (red) NCs dissolved in DMF. (**D**) Comparison of optical absorption and emission spectra of $Ag_{29}(BDT)_{12}(PPh_3)_4$ (black) and $Cs_3Ag_{29}(BDT)_{12}(DMF)_x$ (red) NCs in crystalline films. Reproduced with permission from Reference [154]. Copyright 2019 American Chemical Society.

Both $[Ag_{29}(BDT)_{12}(PPh_3)_4]^{3-}$ and $[Cs_3Ag_{29}(BDT)_{12}(DMF)_x]^0$ solutions showed similar absorption and photoluminescence (PL) spectra (Figure 12C). This indicates that Cs^+ attachment and PPh_3 desorption did not markedly change the electronic structure of the $Ag_{29}(BDT)_{12}$ NCs. In contrast, the absorption and PL spectra of $[Ag_{29}(BDT)_{12}(PPh_3)_4]^{3-}$ and $[Cs_3Ag_{29}(BDT)_{12}(DMF)_x]^0$ in the crystalline state were quite different (Figure 12D). The 1D CS of $[Cs_3Ag_{29}(BDT)_{12}(DMF)_x]^0$ was considered to show different optical behavior from that of the individual $[Ag_{29}(BDT)_{12}(PPh_3)_4]^{3-}$ because of the electronic interactions between adjacent NCs in the 1D CS of $[Cs_3Ag_{29}(BDT)_{12}(DMF)_x]^0$.

2.4. Introduction of Linker Molecules

In the examples described in Section 2.3, 1D CSs were formed by the counterion acting as a linker. When an organic molecule is used as the linker, the distance between NCs in a 1D CS can be freely controlled because the design of the structure of organic molecules is well understood. In fact, the geometry of an MOF is controlled by the design of the linker organic molecule [155]. In recent years, several 1D CSs of metal NCs with organic molecules as linkers have also been reported.

Table 1. Connection modes, NCs, linkers, publication years, and references for 1D CS.

Connection Mode	NC	Linker	Year	Ref.
Formation of metal−metal bond (Figure 2A)	$[Au_{25}(S\text{-}Bu)_{18}]^0$	-	2014	[122]
	$[Au_{25}(S\text{-}Pen)_{18}]^0$	-	2017	[140]
	$[Au_{24}Hg(S\text{-}Bu)_{18}]^0$	-	2019	[141]
	$[Au_{24}Cd(S\text{-}Bu)_{18}]^0$	-		
	$[Au_4Pd_2(PET)_8]^0$	-	2017	[143]
	$[Au_4Pt_2(SCH_2PhCl)_8]^0$	-	2020	[142]
	$[Au_4Pt_2(PET)_8]^0$	-		
	$(AuAg)_{34}(A\text{-}Adm)_{20}$	-	2020	[146]
Formation of Ag−O, Ag−S, Ag−Cl bond, etc. (Figure 2B)	$Ag_{20}(CO_3)(S\text{-}^tBu)_{10}(CH_3COO)_8(DMF)_2$	-	2014	[147]
	$Ag_{18}(CO_3)(S\text{-}^tBu)_{10}(NO_3)_6(DMF)_4$	-	2017	[148]
	$Ag_{44}(V_{10}O_{28})(S\text{-}Et)_{20}(PhSO_3)_{18}(H_2O)_2$	-	2019	[149]
	$Au_7Ag_8(dppf)_3(CF_3COO)_7$	-	2019	[150]
Control of counter ion (Figure 2C)	$[Au_{21}(S\text{-}c\text{-}C_6H_{11})_{12}(DPPM)_2]^+$	$[AgCl_2]^-$	2018	[152]
	$[Au_{21}(S\text{-}c\text{-}C_6H_{11})_{12}(DPPM)_2]^+$	$[Cl]^-$		
	$[Ag_{29}(BDT)_{12}(PPh_3)_4]^{3-}$	$[Cs]^+$	2019	[154]
Introduction of linker molecule (Figure 2D)	$Ag_{14}(DT\text{-}o\text{-}C)_6$	pyrazine [a]	2018	[156]
	$Ag_{18}(PhPO_3)(S\text{-}^tBu)_{10}(CF_3COO)_2(PhPO_3H)_4$	bpy-NH$_2$ [a]	2019	[157]
	$Ag_{15}Cl(S\text{-}^tBu)_8(CF_3COO)_{5.67}(NO_3)_{0.33}(DMF)_2$	bpy [a]	2019	[158]
	$Ag_{10}(CF_3COO)_4(S\text{-}^tBu)_6(CH_3CN)_2$	*p*-iah [a]	2019	[159]
	$Ag_{10}(CF_3COO)_4(S\text{-}^tBu)_6(CH_3CN)$	*o*-iah [a]		
	$Cd_6Ag_4(S\text{-}Ph)_{16}(DMF)_3(CH_3OH)$	bpe [a]	2020	[160]

[a] See Scheme 2.

For example, in 2018, Zang et al. [156] reported a 1D CS in which $Ag_{14}(DT\text{-}o\text{-}C)_6$ NCs (DT-*o*-C = 1,2-dithiolate-o-carborane, Scheme 1(17)) were linked by pyrazine (Scheme 2(1)). In this study, first, $[Ag_{14}(DT\text{-}o\text{-}C)_6(\text{pyridine}/p\text{-methylpyridine})_8]$ (Scheme 2(2),(3)) were identified as Ag NCs with high thermal stability that maintained their framework structure even at 150 °C or higher in air (Figure 13A). Then, they attempted to synthesize Ag NCs in which the pyridine or *p*-methylpyridine ligands of these Ag NCs were replaced by pyrazine. As a result, they obtained a 1D CS in which $Ag_{14}(DT\text{-}o\text{-}C)_6$ NCs were linked by pyrazine (Figure 13B). In the obtained structure, pyrazine was coordinated to each $Ag_{14}(DT\text{-}o\text{-}C)_6$ NC at a diagonal position, which caused the 1D CS to rotate in the clockwise direction with respect to the (001) axis. In this study, the researchers also succeeded in forming 2D and 3D CSs composed of $Ag_{14}(DT\text{-}o\text{-}C)_6$ NCs by changing the structure of the bipyridine ligand, as described later in Sections 3.2 and 4.3, respectively.

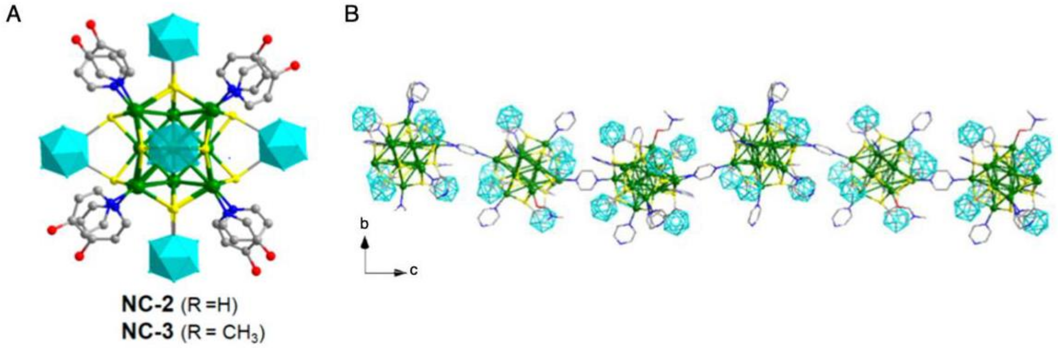

Figure 13. (**A**) Structure of $Ag_{14}(DT\text{-}o\text{-}C)_6(\text{pyridine}/p\text{-methylpyridine})_8$. (**B**) 1D helix of $Ag_{14}(DT\text{-}o\text{-}C)_6$ NC. Ag = green and pink, S = yellow, C = gray, N = blue, carborane = turquoise. Reproduced with permission from Reference [156]. Copyright 2018 American Chemical Society.

Because N readily coordinates to Ag, bipyridine is often used to connect NCs containing Ag. In 2019, Zang and colleagues formed a 1D CS composed of $Ag_{18}(PhPO_3)(S\text{-}^tBu)_{10}(CF_3COO)_2(PhPO_3H)_4$ ($PhPO_3^{2-}$ = phenylphosphinic diion; $PhPO_3H^-$ = phenylphosphinic acid ion) NC nodes with bipyridine(3-amino-4,4′-bipyridine (bpy-NH_2, Scheme 2(4)) linkers [157]. In this experiment, NC synthesis, ligation, and crystallization were performed simultaneously in one pot (Figure 14A). The node $Ag_{18}(PhPO_3)(S\text{-}^tBu)_{10}$ NCs contained $PhPO_3^{2-}$ as an anion template in their center. In the crystal, adjacent $Ag_{18}(PhPO_3)(S\text{-}^tBu)_{10}$ NCs were linked by two bpy-NH_2 to form a 1D CS (Figure 14B).

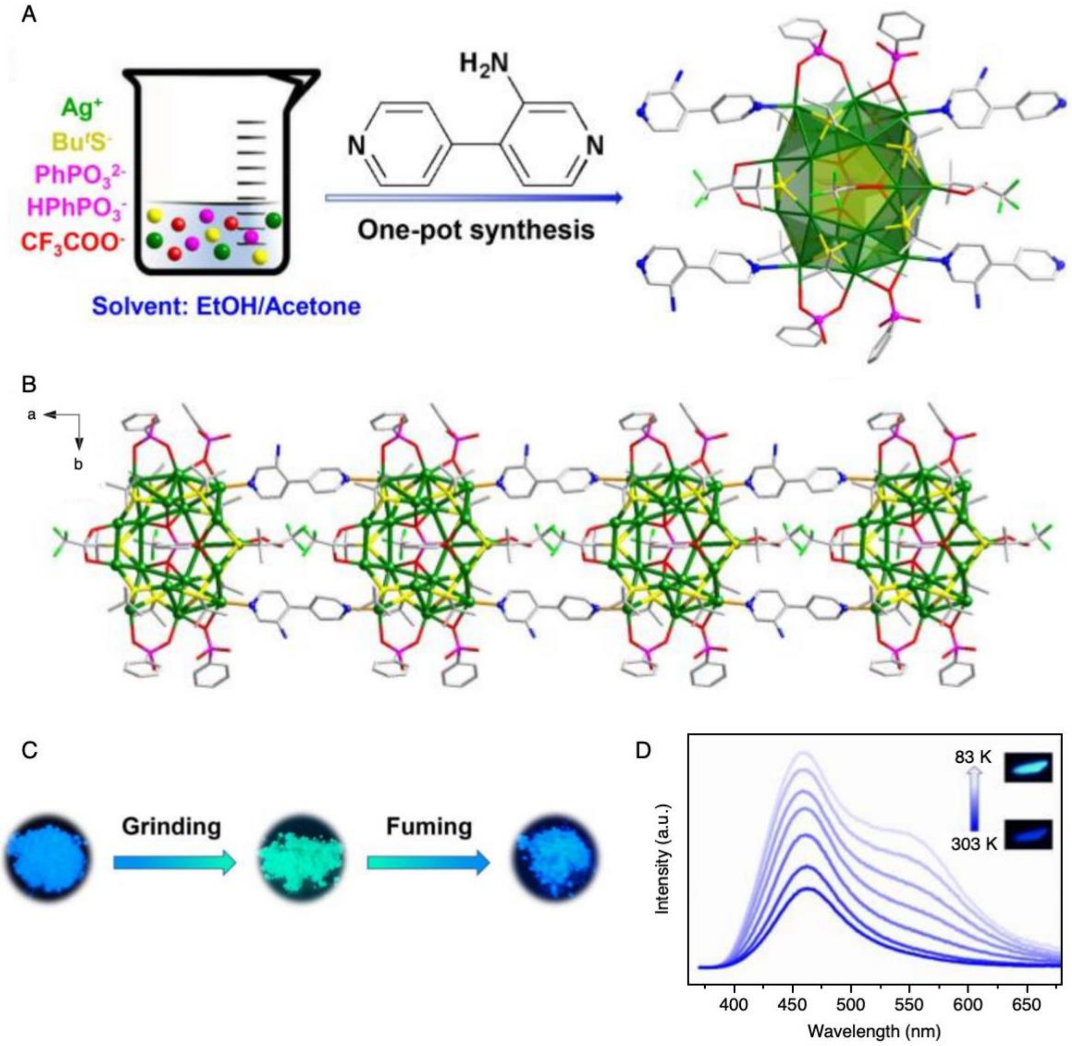

Figure 14. (**A**) Schematic representation of the one-pot synthesis of $[Ag_{18}(PhPO_3)(S\text{-}^tBu)_{10}(CF_3COO)_2(PhPO_3H)_4(bpy\text{-}NH_2)_2]\cdot(PhPO_3H_2)$. (**B**) 1D structure of $[Ag_{18}(PhPO_3)(S\text{-}^tBu)_{10}(CF_3COO)_2(PhPO_3H)_4(bpy\text{-}NH_2)_2]\cdot(PhPO_3H_2)$. Ag = green, S = yellow, C = gray, N = blue, O = red, F = light green, P = purple. H atoms are omitted for clarity. (**C**) Luminescent images of the as-synthesized, ground, and fumed $[Ag_{18}(PhPO_3)(S\text{-}^tBu)_{10}(CF_3COO)_2(PhPO_3H)_4(bpy\text{-}NH_2)_2]$ under ultraviolet light irradiation. (**D**) Temperature-dependent luminescence spectra of $[Ag_{18}(PhPO_3)(S\text{-}^tBu)_{10}(CF_3COO)_2(PhPO_3H)_4(bpy\text{-}NH_2)_2]$ from 30 to −190 °C in the solid state. The inset photographs show the emission of $[Ag_{18}(PhPO_3)(S\text{-}^tBu)_{10}(CF_3COO)_2(PhPO_3H)_4(bpy\text{-}NH_2)_2]$ in the solid state under ultraviolet light irradiation at room temperature and liquid nitrogen temperature. Reproduced with permission from Reference [157]. Copyright 2019 Wiley-VCH.

The obtained 1D CS was stable up to 110 °C in a nitrogen (N_2) atmosphere. When mechanical stimulation was applied to the 1D CS, its PL wavelength changed. When the 1D CS sample subjected to mechanical stimulation was recrystallized, its PL wavelength returned to the original value (Figure 14C). Thus, the PL of the 1D CS composed of $Ag_{18}(PhPO_3)(S\text{-}^tBu)_{10}$ NCs exhibited reversible mechanochromism. Because this 1D CS emitted light at two wavelengths and its PL intensity ratio changed with temperature (thermochromism; Figure 14D), the authors suggested that this 1D CS could be applied as a thermometer.

In 2019, Bakr et al. [158] also reported the connection of Ag NCs by bipyridine. In this study, a 1D CS was synthesized in one pot (Figure 15A). $Ag_{15}Cl(S\text{-}^tBu)_8(CF_3COO)_{5.67}(NO_3)_{0.33}(DMF)_2$ was used as the node, and 4,4′-bipyridine (bpy, Scheme 2(5)) was used as the linker. In $Ag_{15}Cl(S\text{-}^tBu)_8(CF_3COO)_{5.67}(NO_3)_{0.33}(DMF)_2$, Cl^-acted as an anion template. The core of the $Ag_{15}Cl$ NC had a geometry in which one Ag was lost from the $Ag_{16}Cl$ core of the $Ag_{16}Cl(S\text{-}^tBu)_8(CF_3COO)_7(DMF)_4(H_2O)$ NC, which did not form a 1D CS, namely individual $Ag_{16}Cl(S\text{-}^tBu)_8(CF_3COO)_7(DMF)_4(H_2O)$ NCs (Figure 15B). The 1D CS with a ladder structure was formed by combining these $Ag_{15}Cl$ NCs with three adjacent $Ag_{15}Cl$ NCs via four bpy molecules (Figure 15C). It was found that the 1D CS displayed slightly higher thermal stability than that of the $Ag_{16}Cl$ NCs (Figure 15D).

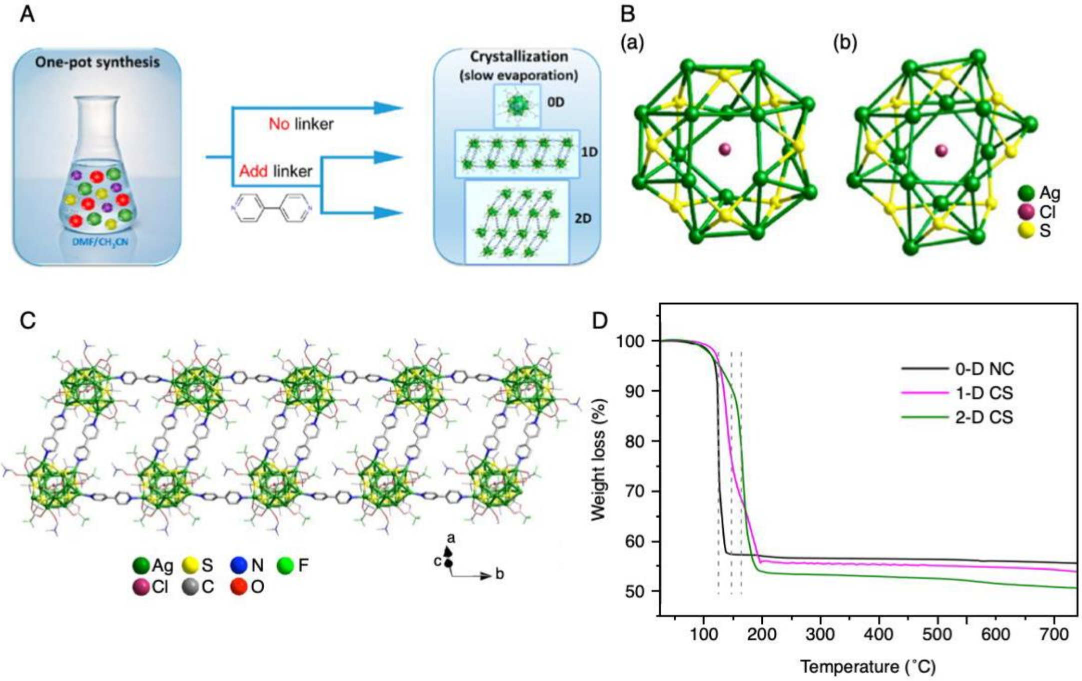

Figure 15. (**A**) Synthesis of Ag NCs and NC-based frameworks. (**B**) Top views of the core structures of (a) $Ag_{16}Cl(S\text{-}^tBu)_8(CF_3COO)_7(DMF)_4(H_2O)$ and (b) $Ag_{15}Cl(S\text{-}^tBu)_8(CF_3COO)_{5.67}(NO_3)_{0.33}(DMF)_2$. (**C**) Crystal structure of the corresponding 1D CS. Free (co-crystallized) DMF molecules are not shown. The green semitransparent spheres in the Ag clusters are shown as a visual guide. H atoms were omitted for clarity. (**D**) Thermogravimetric analysis curves of NCs, 1D CS, and 2D CS (see Section 3.2). Reproduced with permission from Reference [158]. Copyright 2019 American Chemical Society.

In the above three studies, the bipyridines had a rigid framework structure. In 2019, Cao et al. formed 1D CSs of Ag NCs by using pyridine derivatives (*p*-iah = 4-pyridine carboxylic hydrazide, Scheme 2(6); *o*-iah = 2-carboxylic hydrazide, Scheme 2(7)) that contained N in both the rigid pyridine framework and flexible substituents [159]. In this study, the 1D CSs were obtained by reacting $Ag_{12}(S\text{-}^tBu)_6(CF_3COO)_6(CH_3CN)_6$ (CH_3CN = acetonitrile) with the above-mentioned pyridine derivatives. The SC-XRD analysis of the products revealed that $Ag_{10}(CF_3COO)_4(S\text{-}^tBu)_6(CH_3CN)_2$ and $Ag_{10}(CF_3COO)_4(S\text{-}^tBu)_6(CH_3CN)$ were the nodes in the 1D CSs with *p*-iah and *o*-iah, respectively (Figure 16A(a),B(a)). These 1D CSs containing *p*-iah and *o*-iah had cross-helical and parallel chain structures, respectively (Figure 16A(b),B(b)). The latter structure also contained hydrogen bonds (N–H···O) between the parallel linker molecules. It is interesting that different 1D CSs formed depending on the position of N in the linker molecule (Scheme 2(6),(7)).

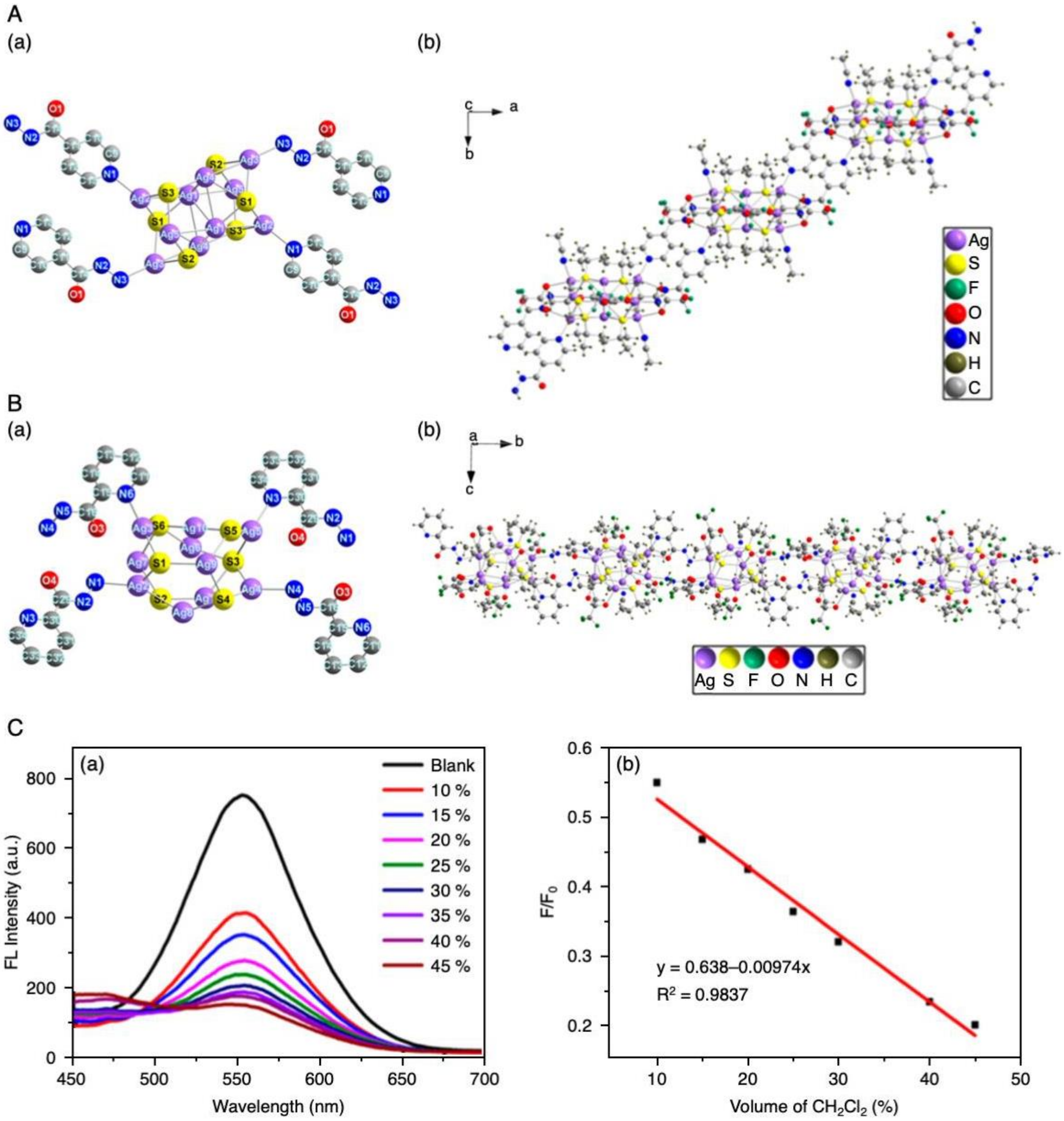

Figure 16. (a) Structural units and (b) spatial stacking diagrams of (**A**) $Ag_{10}(CF_3COO)_4(S\text{-}^tBu)_6(CH_3CN)_2(p\text{-iah})_2$ and (**B**) $Ag_{10}(CF_3COO)_4(S\text{-}^tBu)_6(CH_3CN)(o\text{-iah})_2$. (**C**) (a) PL spectra of $Ag_{10}(CF_3COO)_4(S\text{-}^tBu)_6(CH_3CN)_2(o\text{-iah})_4$ in CCl_4 with various volume fractions of CH_2Cl_2. (b) Linear plot of fluorescence intensity against the volume fraction of CH_2Cl_2 in CCl_4. Reproduced with permission from Reference [159]. Copyright 2019 American Chemical Society.

Both 1D CSs showed PL and that with *o*-iah as the linker exhibited weak green PL in highly polar solvents and strong yellow PL in solvents with low polarity. Based on these characteristics, the authors suggested that the 1D CS with *o*-iah could be used to measure the concentration of dichloromethane (CH_2Cl_2, Figure 16C) or trichloromethane ($CHCl_3$) in tetrachloromethane (CCl_4).

Bipyridines can also be used as linkers to form 1D CSs of Ag chalcogenide NCs. Very recently, Xu and co-workers reported the formation of a zigzag-type of 1D CS with $Cd_6Ag_4(S\text{-Ph})_{16}(DMF)(H_2O)$ (S-Ph = benzenethiolate, Scheme 1(18) and Figure 17A) as a node and *trans*-1,2-bis(4-pyridyl)ethylene (bpe, Scheme 2(8)) as a linker (Figure 17B) [160]. This 1D CS was obtained by the reaction of $Cd_6Ag_4(S\text{-Ph})_{16}(DMF)_3(CH_3OH)$ (CH_3OH = methanol) with bpe. In the obtained 1D CS, N of bpe coordinated to Cd not Ag (Figure 17A). Such a coordination pattern has also been observed in 2D and 3D CSs composed of $Cd_6Ag_4(S\text{-Ph})_{16}$ and bpe previously reported by Zhang et al. [161,162].

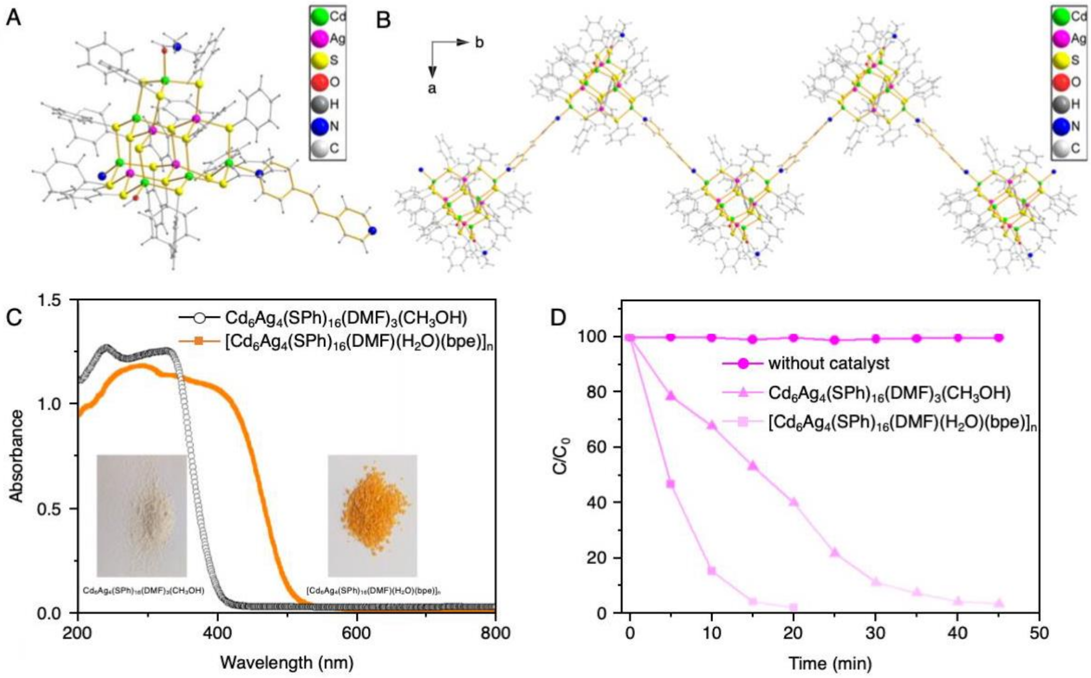

Figure 17. (**A**) Structures of Cd_6Ag_4(S-Ph)$_{16}$(DMF)(H_2O) and (**B**) 1D CS of Cd_6Ag_4(S-Ph)$_{16}$(DMF)(H_2O)(bpe). (**C**) Solid-state ultraviolet-visible diffuse reflectance spectra of the discrete Cd_6Ag_4(SPh)$_{16}$(DMF)$_3$(CH_3OH) (open circles) and 1D CS of Cd_6Ag_4(S-Ph)$_{16}$(DMF)(H_2O)(bpe) (filled squares). (**D**) Comparison of the photocatalytic-degradation efficiencies of the discrete Cd_6Ag_4(S-Ph)$_{16}$(DMF)$_3$(CH_3OH) (triangles), 1D CS of Cd_6Ag_4(S-Ph)$_{16}$(DMF)(H_2O)(bpe) (squares), and without a catalyst (circles). Reproduced with permission from Reference [160]. Copyright 2020 American Chemical Society.

They compared the electronic structures of the resulting 1D CS and individual Cd_6Ag_4(S-Ph)$_{16}$(DMF)$_3$(CH_3OH) NCs. The results revealed that the band gap of the NCs was narrowed by the formation of the 1D CS (Figure 17C). In the 1D CS, the optical absorption onset was redshifted to the visible region. They used the 1D CS as a visible light (>420 nm)-responsive photocatalyst to decompose the organic dye Rhodamine B in water. The 1D CS exhibited higher photocatalytic activity toward Rhodamine B degradation than that of the Cd_6Ag_4(S-Ph)$_{16}$ NCs (Figure 17D) and high stability during the photocatalytic reaction.

3. Two-Dimensional Structures

To date, Ag NCs have been used as the building blocks in almost all 2D CSs. Like Au NCs, Ag NCs have unique electronic and optical properties [68,163–166] and are expected to be applied in various fields. However, Ag NCs are less stable than Au NCs against external stimuli, such as light and solvents. Therefore, studies have been actively conducted to improve the stability of Ag NCs by assembly of CSs and thereby improve their physical properties. In Sections 3.1 and 3.2 we focus on the connection of NCs by Ag−O bond formation (Figure 2B) and introducing linker molecules (Figure 2D), respectively. Table 2 summarizes the connection methods, NCs, linkers, reported years, and reference numbers of the relevant literature. Several of the ligands used in these studies are shown in Scheme 1. The organic molecules used as linkers are depicted in Scheme 2.

3.1. Connection via Ag−O Bonds

In 2017, Mak et al. [148] reported the formation of 2D CSs with $Ag_{20}(CO_3)$(S-*i*Pr)$_{10}$(CF_3COO)$_9$(CF_3COOH)(CH_3OH)$_2$ (S-*i*Pr = isopropylthiolate, Scheme 1(5)) or $Ag_{20}(CO_3)$(S-*c*-C_6H_{11})$_{10}$(CF_3COO)$_{10}$(CF_3COOH)$_2$(H_2O)$_2$ as building blocks in their paper on the formation of 1D

CSs. These NCs contained CO_3^{2-} as an anion template at the center of their cores (Figure 18A,B). The structures of the SR in these two types of $Ag_{20}(CO_3)(SR)_{10}$ NCs were different (S-*i*Pr vs. S-*c*-C_6H_{11}), which influenced the formation angle and bond distance between adjacent NCs in the 2D CSs. The O^- of CF_3COO^- and Ag of an adjacent NC were directly linked via an Ag−O bond with a length of 14 Å. In addition, isolated Ag was trapped between CF_3COO^- of adjacent NCs, so the adjacent NCs were connected via an O−Ag−O bond with a length of 17 Å. The 2D CS consisting of $Ag_{20}(CO_3)(S\text{-}iPr)_{10}(CF_3COO)_9(CF_3COOH)(CH_3OH)_2$ showed dual emission at room temperature. Because both zero-dimensional $[Ag_{20}(S\text{-}^tBu)_{10}(CF_3COO)_2]Cl\cdot(CF_3COO)_7\cdot5CH_3OH$ NCs and the 1D CS of $Ag_{20}(CO_3)(S\text{-}^tBu)_{10}(CH_3COO)_8(DMF)_2$ emit only single emission peaks, it was speculated that the formation of the 2D CS was related to the observed dual emission.

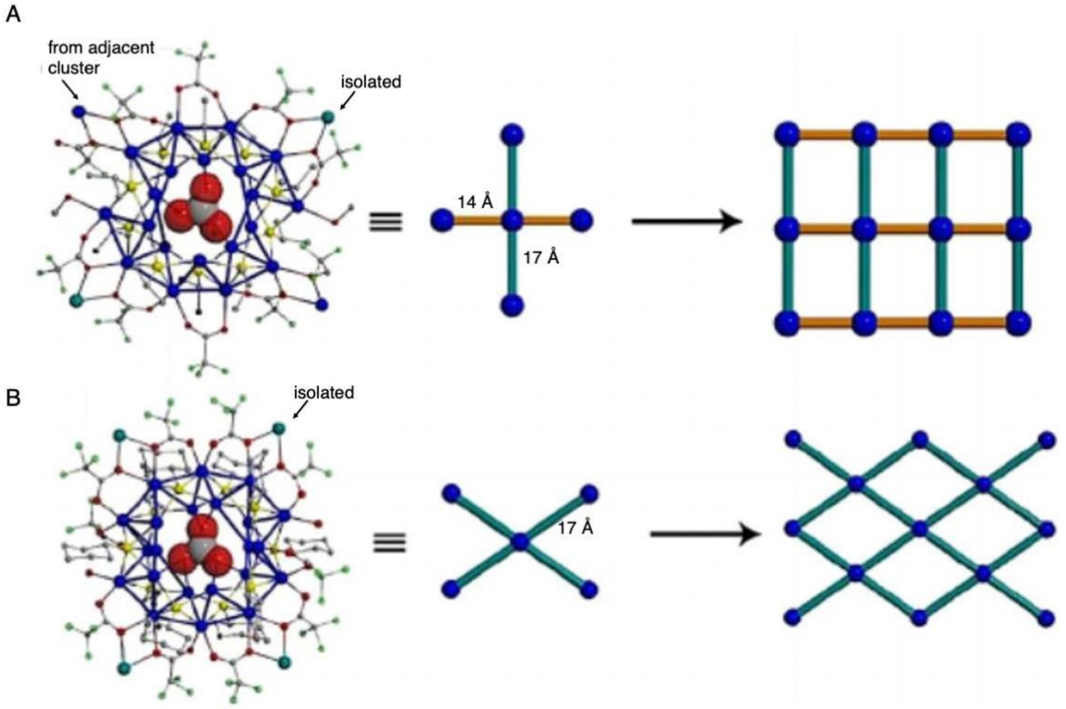

Figure 18. (**A**) The molecular building block in $Ag_{20}(CO_3)(S\text{-}iPr)_{10}(CF_3COO)_9(CF_3COOH)(CH_3OH)_2$ with its four linking sites, and condensation of blocks into a 4,4-net. (**B**) Similar condensation of molecular building blocks of $Ag_{20}(CO_3)(S\text{-}c\text{-}C_6H_{11})_{10}(CF_3COO)_{10}(CF_3COOH)_2(H_2O)_2$. Note the difference between the 'arms' with lengths of 14 Å (orange) and 17 Å (cyan). Ag = blue and cyan, S = yellow, O = red, C = gray, F = green. Reproduced with permission from Reference [148]. Copyright 2017 Wiley-VCH.

In 2019, Sun and co-workers also reported the formation of a 2D CS, using Ag NCs [149]. In this study, a 2D CS consisting of $Ag_{46}(V_{10}O_{28})(S\text{-}Et)_{23}(PhSO_3)_{15}(CO_3)$ was formed (Figure 19), using a different solvent from the case of $Ag_{44}(V_{10}O_{28})(S\text{-}Et)_{20}(PhSO_3)_{18}(H_2O)_2$, which formed a 1D CS (Figure 9). These Ag NCs have the same total number of ligands (S-Et and $PhSO_3^-$) of 38 but different ratios of the ligand types. They considered that the ligand ratio affected the number of Ag atoms in the core and also the connection mode between adjacent NCs.

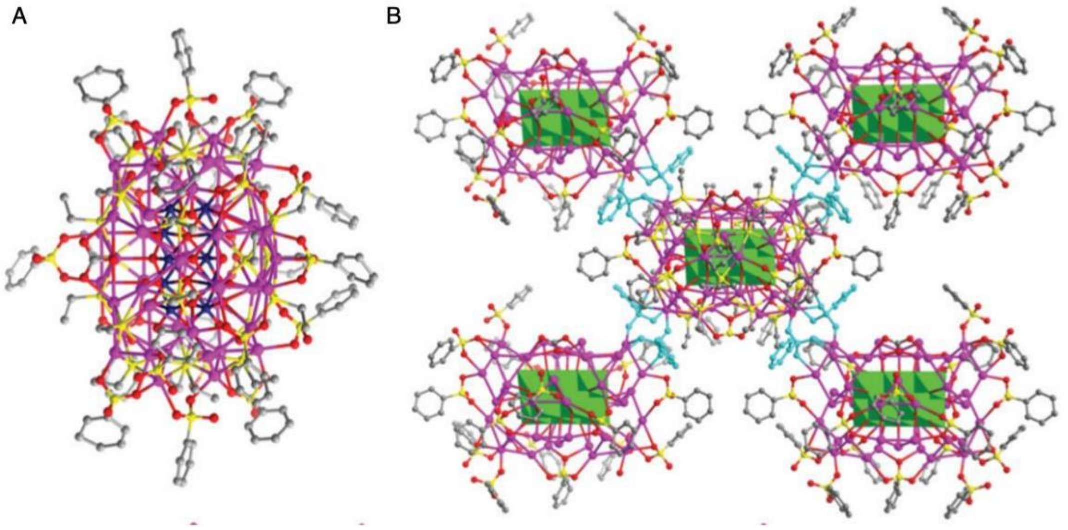

Figure 19. (**A**) Structure and (**B**) 2D extended layer structure of $Ag_{46}(V_{10}O_{28})(S\text{-}Et)_{23}(PhSO_3)_{15}(CO_3)$ with all bridging $PhSO_3^-$ ligands highlighted in cyan and $V_{10}O_{28}^{6-}$ shown as green polyhedra. Ag = purple, V = dark blue, S = yellow, C = gray, O = red. All H atoms are omitted. Reproduced with permission from Reference [149]. Copyright 2019 Royal Society of Chemistry.

Xu et al. [166], also in 2019, reported 2D CSs of $Ag_{11}Cl(N\text{-}L)_8(CF_3COO)_2{\cdot}2CHCl_3$ (Figure 20), $Ag_{11}Cl(N\text{-}L)_8(NO_3)_2{\cdot}2CHCl_3$, and $Ag_{11}Cl(N\text{-}L)_8(CF_3SO_3)_2{\cdot}2CHCl_3$ (N-L = 2-acetamido-5-methyl-1,3,4-thiadiazole, Scheme 1(19)), in which adjacent NCs are linked by Ag−O bonds. SR, alkyne, or phosphine ligands are generally used in metal NCs. In this study, their aim was to synthesize Ag NCs by using an N-donor ligand, which is not appropriate based on the hard/soft acid/base theory [167], and form corresponding CSs. The three kinds of 2D CSs obtained had similar frameworks regardless of the coordination ions (CF_3COO^-, NO_3^-, or $CF_3SO_3^-$), which means that the framework structure shown in Figure 20B is very rigid. It was found that $Ag_{11}Cl(N\text{-}L)_8(CF_3COO)_2{\cdot}2CHCl_3$ showed dual-emission behavior and that its PL peaks had different optimal excitation wavelengths.

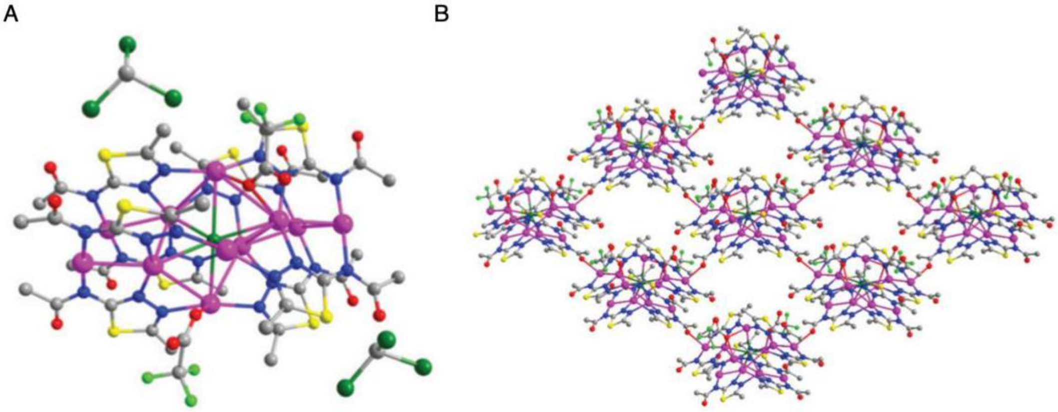

Figure 20. (**A**) Structure of $Ag_{11}Cl(N\text{-}L)_8(CF_3COO)_2{\cdot}2CHCl_3$ and (**B**) simplified 2D network featuring a four-connected topology. Ag = purple, S = yellow, O = red, C = gray, Cl = dark green, N = blue, F = neon green. Reproduced with permission from Reference [166]. Copyright 2019 Royal Society of Chemistry.

3.2. Introduction of Linker Molecules

As described below, in Section 4.3, in 2017, Zang et al. [168] reported the formation of a 3D CS in which $Ag_{12}(S\text{-}^tBu)_8(CF_3COO)_4$ NCs were linked by bpy. This was a pioneering study on the formation of an MOF, using Ag NCs as nodes, and has greatly influenced subsequent studies. In 2018, they synthesized a 2D CS consisting of Ag_{12} NCs and bpy [169]. The core structure of the node was changed (isomerized) by dissolving an $Ag_{12}(S\text{-}^tBu)_6(CF_3COO)_6$ NC MOF crystal in a mixed solvent consisting of *N*,*N*-dimethylethanamide (DMAC) and toluene, which changed the geometrical structure of the entire CS from 3D to 2D (Figure 21A,B). This result indicates that the solvent selection is important in the design of the structure of metal NCs and their CSs. In the 2D CS consisting of newly formed $Ag_{12}(S\text{-}^tBu)_6(CF_3COO)_6$ NCs, each $Ag_{12}(S\text{-}^tBu)_6(CF_3COO)_6$ NC was linked to six adjacent $Ag_{12}(S\text{-}^tBu)_6(CF_3COO)_6$ NCs via linkers to produce a highly symmetric 2D CS (Figure 21C). The layers were separated by 7.23 Å, with weak interactions between them. It was also revealed that the reversible structural transformation between 3D and 2D CSs could be induced by appropriate solvent selection (Figure 21A,B).

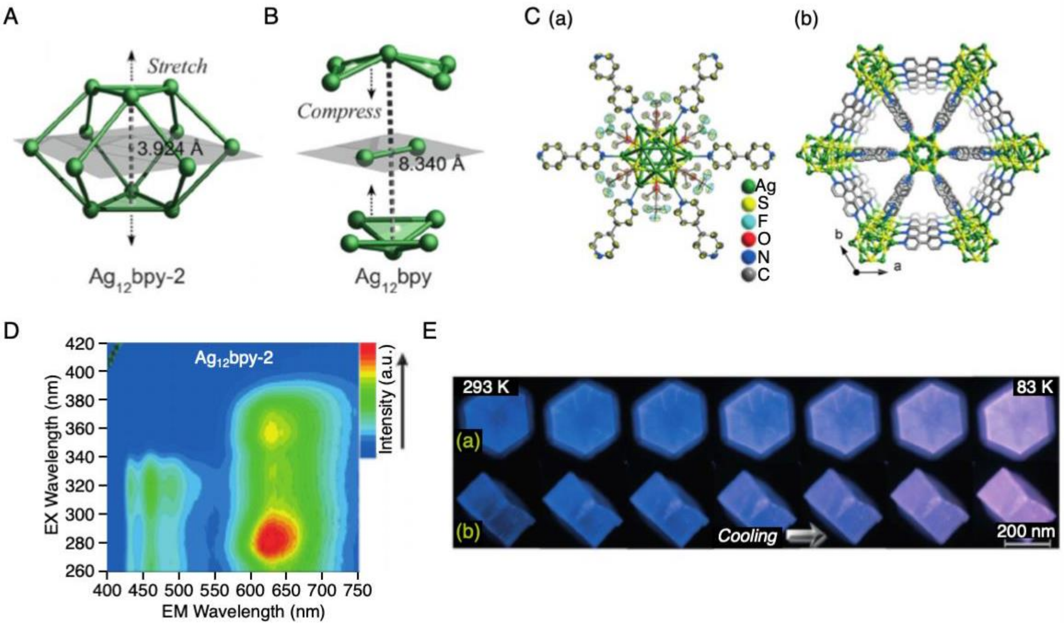

Figure 21. Comparison of the Ag_{12} core structures in (**A**) $Ag_{12}(S\text{-}^tBu)_6(CF_3COO)_6(bpy)_3$ (Ag_{12}bpy-2) and (**B**) $Ag_{12}(S\text{-}^tBu)_8(CF_3COO)_4(bpy)_4$ (Ag_{12}bpy). (**C**) (a) Perspective view of an $Ag_{12}S_6$ node with six pendant bpy linkers (ORTEP drawing at the 50% probability level). (b) Stacking of the 2D network structure of $Ag_{12}(S\text{-}^tBu)_6(CF_3COO)_6(bpy)_3$ viewed along the crystallographic *c*-axis. Ag = green, S = yellow, C = gray, N = blue; CF_3COO^-, ^tBu, and H atoms are omitted for clarity. (**D**) 3D-excitation emission matrix of $Ag_{12}(S\text{-}^tBu)_6(CF_3COO)_6(bpy)_3$ measured at −190 °C. (**E**) Thermochromic images of the (a) exterior {001} surfaces and (b) exposed interior {010}/{100} planes of $Ag_{12}(S\text{-}^tBu)_6(CF_3COO)_6(bpy)_3/NH_2\cdot$(bpy:bpy-$NH_2$ = 20:1) solvated single crystals under ultraviolet light irradiation. Reproduced with permission from Reference [169]. Copyright 2018 Wiley-VCH.

Structural deformation of the CSs also induced changes in their electronic structure and PL properties. For example, the 3D CS only showed PL at a single wavelength, regardless of temperature and excitation wavelength, whereas the 2D CS exhibited PL of two colors (blue and red), depending on the excitation wavelength (Figure 21D). To enhance the blue emission of the 2D CS, the researchers introduced bpy-NH_2, which itself emits blue light, as a linker, to fabricate a 2D CS containing two types of linkers, bpy and bpy-NH_2. The intensity ratio of the red and blue PL signals depended on the mixing ratio of linker molecules. At the optimum linker mixing ratio, the PL intensity ratio of the red and blue peaks depended on temperature. Therefore, this 2D CS containing two types of linkers could be used as a temperature sensor (Figure 21E).

In 2018, the same group also reported the formation of a 2D CS consisting of Ag_{14}(DT-*o*-C$)_6$ NCs [156]. The 2D CS with Ag_{14}(DT-*o*-C$)_6$, as a structural unit (Figure 22A), was fabricated by changing the linker structure from that used to form the 1D CS (Section 2.4 and Figure 13) to dipyridin-4-yl-diazene (Scheme 2(9)). The obtained 2D CS possessed a rhombic network structure with $Ag_{14}(DT\text{-}o\text{-}C)_6(CH_3CN)_4$ as nodes (Figure 22B).

Table 2. Connection modes, NCs, linkers, publication years, and references for 2D CS.

Connection Mode	NC	Linker	Year	Ref.
Formation of Ag–O, Ag–S, Ag–Cl bond, etc. (Figure 2B)	$Ag_{20}(CO_3)(S\text{-}i\text{Pr})_{10}(CF_3COO)_9(CF_3COOH)(CH_3OH)_2$	-	2017	[148]
	$Ag_{20}(CO_3)(S\text{-}Cy)_{10}(CF_3COO)_{10}(CF_3COOH)_2(H_2O)_2$	-		
	$Ag_{46}(V_{10}O_{28})(S\text{-}Et)_{23}(PhSO_3)_{15}(CO_3)$	-	2019	[149]
	$Ag_{11}Cl(N\text{-}L)_8(CF_3COO)_2{\cdot}2CHCl_3$	-	2019	[166]
	$Ag_{11}Cl(N\text{-}L)_8(NO_3)_2{\cdot}2CHCl_3$	-		
	$Ag_{11}Cl(N\text{-}L)_8(CF_3SO_3)_2{\cdot}2CHCl_3$	-		
Introduction of linker molecule (Figure 2D)	$Ag_{12}(S\text{-}^t\text{Bu})_6(CF_3COO)_6$	bpy ^{a}	2018	[169]
	$Ag_{14}(DT\text{-}o\text{-}C)_6$	dipyridin-4-yl-diazene ^{a}	2018	[156]
	$Ag_{12}(S\text{-}^t\text{Bu})_6(CF_3COO)_6$	TPPA ^{a}	2018	[170]
	$Ag_{12}(S\text{-}^t\text{Bu})_6(CF_3COO)_3$	TPyP ^{a}	2019	[171]
	$Ag_{14}Cl(S\text{-}^t\text{Bu})_8(CF_3COO)_5(DMF)$	bpy ^{a}	2019	[158]
	$Ag_{10}(CF_3COO)_4(S\text{-}^t\text{Bu})_6(CH_3CN)_4$	*m*-iah ^{a}	2019	[159]
	$Ag_{12}(S\text{-}^t\text{Bu})_6(CF_3COO)_6(CH_3CN)_6$	bpz-NH$_2$ ^{a}	2019	[172]

a See Scheme 2.

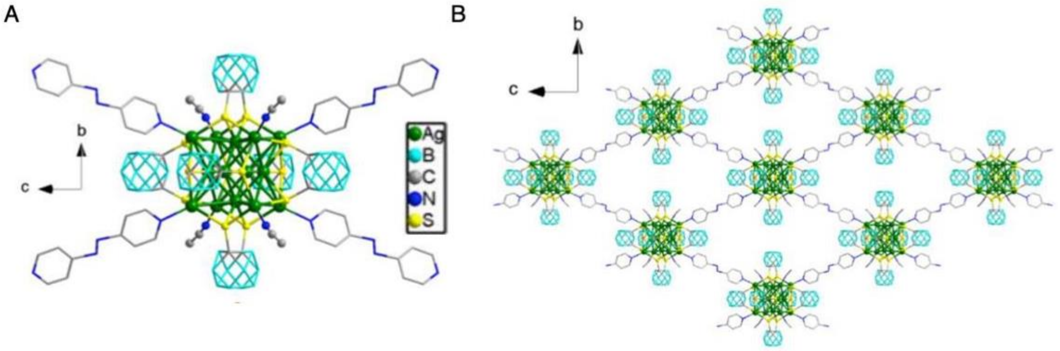

Figure 22. (**A**) Structural unit and (**B**) 2D CS of $Ag_{14}(DT\text{-}o\text{-}C)_6(CH_3CN)_4$(dipyridin-4-yl-diazene)$_2$. Reproduced with permission from Reference [156]. Copyright 2018 American Chemical Society.

In 2018, Zang et al. [170] reported the formation of a 2D CS consisting of $Ag_{12}(S\text{-}^t\text{Bu})_6(CF_3COO)_6$ and tris(4-pyridylphenyl)-amine (TPPA; Scheme 2(10) and Figure 23A). This structure is interesting because the distance between the 2D layers can be changed. In this 2D CS, DMAC used as a solvent existed between layers immediately after the synthesis and the 2D layers overlapped, as shown in Figure 23B(a),(d). When the DMAC was partially removed from this structure, the overlap of the 2D layers changed, as illustrated in Figure 23B(b),(e). Furthermore, when this structure was immersed again in the mother liquor, the structure changed to that depicted in Figure 23B(c),(f). It was also found that the size of the crystal and its emission characteristics changed in accordance with the overlap manner in the 2D CS.

Recently, this group also formed a 2D CS with $Ag_{12}(S^t\text{Bu})_6(CF_3COO)_3$ NCs as nodes by using 5,10,15,20-tetra(4-pyridyl)porphyrin (TPyP, Scheme 2(11)) as a linker (Figure 24A) [171]. TPyP has a photosensitizing effect. Therefore, the ability of the 2D CS to degrade the toxic substance 2-chloroethyl ethyl sulfide (CEES), also called mustard gas, was studied (Figure 24B). The obtained 2D CS showed higher photocatalytic activity than that of a reported MOF. This high photocatalytic activity was ascribed to the synergistic effect of Ag NCs and TPyP, promoting the production of singlet oxygen, which induced the degradation of CEES (Figure 24B). The 2D CS maintained its crystallinity after the photocatalytic reaction and was able to be used repeatedly. The authors pointed out that photocatalytic activity could be further increased by selecting appropriate Ag NCs and organic molecular linkers.

Two other types of 2D CSs were also reported in 2019. In their paper on 1D CS formation (Figure 15 and Section 2.4), Bakr et al. [158] also reported that a 2D CS with $Ag_{14}Cl(S\text{-}^t\text{Bu})_8(CF_3COO)_5(DMF)$ as nodes was formed by changing the concentration of bpy during synthesis (Figure 25A). This $Ag_{14}Cl$ core contained Cl^- at its center as an anion template. Compared with the $Ag_{15}Cl(S\text{-}^t\text{Bu})_8(CF_3COO)_{5.67}(NO_3)_{0.33}(DMF)_2$

node of the 1D CS, the node of the 2D CS ($Ag_{14}Cl(S\text{-}^tBu)_8(CF_3COO)_5(DMF)$) had one less Ag atom. However, the frameworks of these NCs were similar to each other (Figure 25B). The 2D CS showed higher thermal stability than those of individual Ag NCs and the 1D CS (Figure 15D). Unlike individual Ag NCs and the 1D CS, the 2D CS emitted green light with a strong intensity, even at room temperature (Figure 25C). Based on the results of a DFT calculation, it was interpreted that the enhancement of PL intensity was caused by a linker-to-cluster charge transfer excitation. In addition, Gao et al. [159] recently formed a 2D CS (Figure 26) with $Ag_{10}(CF_3COO)_4(S\text{-}^tBu)_6(CH_3CN)_4$ nodes, using 3-pyridine carboxylic hydrazide (*m*-iah, Scheme 2(12)) as a linker, which is the *meta* equivalent of *p*-iah and *o*-iah used to form 1D CSs (Figure 16).

Thus, 2D CS formation by using a linker leads to the assembly of a structure with high stability and quantum yield (QY). However, 2D CS formation decreases the solubility of NCs, which limits their processability and device applicability. Therefore, Zang et al. [172] recently established a method to polymerize 2D CS to overcome this problem and provide materials suitable for practical use (Figure 27A). In this study, $Ag_{12}(S\text{-}^tBu)_6(CF_3COO)_6$ NCs reported in their previous work (Figure 21) [168] were used as nodes. Moreover, 1,4-bis (pyrid-4-yl)benzenamine (bpz-NH_2, Scheme 2(13)) was used as the linker. The amino group of the bpz-NH_2 linker played an important role in polymerization. First, 2D CS crystals consisting of $Ag_{12}(S\text{-}^tBu)_6(CF_3COO)_6$ and bpz-NH_2 were fabricated (Figure 27B). The crystal size was limited to about 200–300 nm by quenching the reaction within 1 min. A 2D CS film was obtained by reacting the crystals with methacrylic anhydride (MA). MA bound to the amino group of bpz-NH_2 (Figure 27C) and was then polymerized with acrylate monomers butyl methacrylate (BMA) and triethylene glycol dimethacrylate (TEGDMA), as shown in Figure 27D.

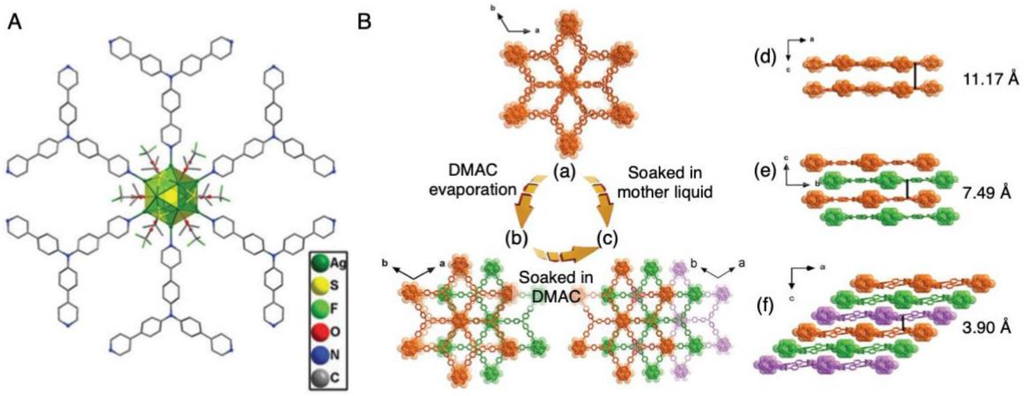

Figure 23. (**A**) Perspective view of an $Ag_{12}S_6$ subunit with six pendant TPPA linkers in each layer. (**B**) Stacking of the 2D network structure of $Ag_{12}(S\text{-}^tBu)_6(CF_3COO)_6$ by TPPA. AA stacking viewed along the (a) *c*-axis and (d) *b*-axis, AB stacking viewed along the (b) *c*-axis and (e) *a*-axis, and ABC stacking viewed along the (c) *c*-axis and (f) *a*-axis. Reproduced with permission from Reference [170]. Copyright 2018 Royal Society of Chemistry.

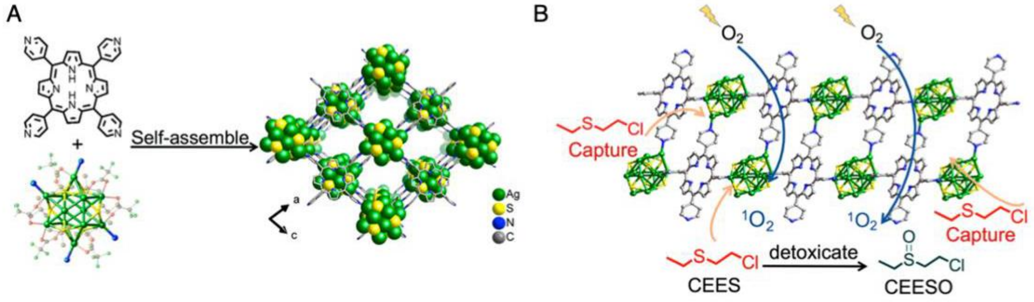

Figure 24. (**A**) Synthesis of $Ag_{12}(S\text{-}^tBu)_6(CF_3COO)_3(TPyP)$. (**B**) Schematic illustration of the capture and photodetoxification of CEES by $Ag_{12}(S\text{-}^tBu)_6(CF_3COO)_3(TPyP)$. Reproduced with permission from Reference [171]. Copyright 2019 American Chemical Society.

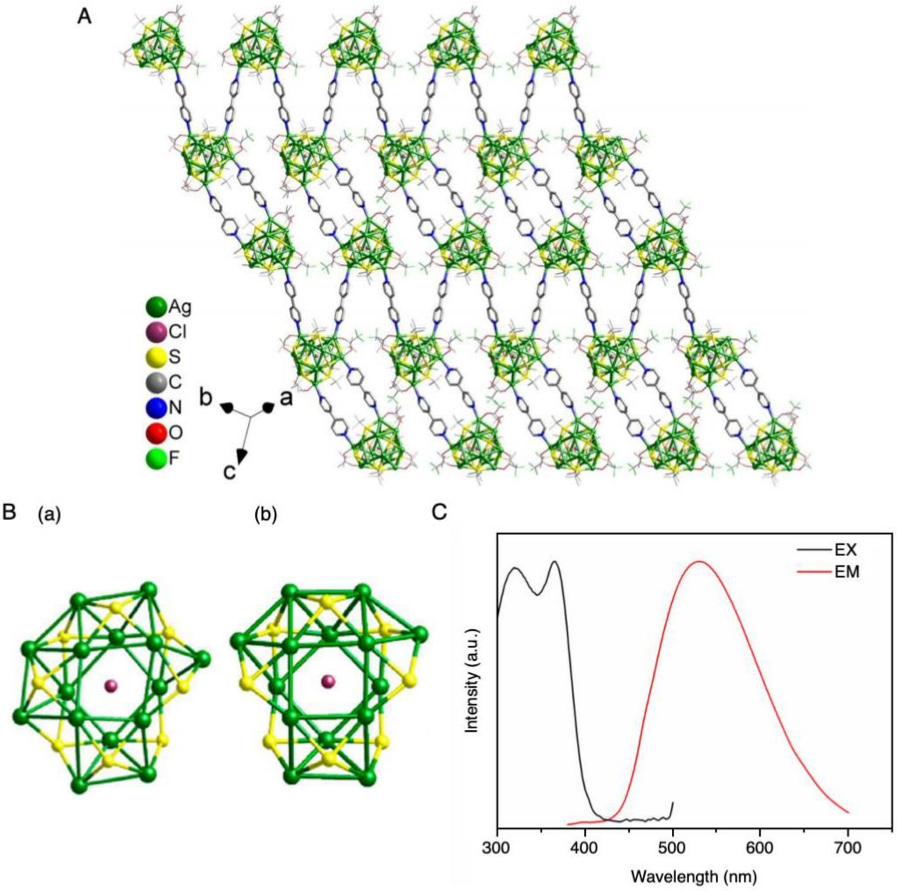

Figure 25. (**A**) Structure of $Ag_{14}Cl(S\text{-}^tBu)_8(CF_3COO)_5(DMF)(bpy)_2$. Free (co-crystallized) DMF molecules are not shown. (**B**) Top views of the core structures of (a) $Ag_{15}Cl(S\text{-}^tBu)_8(CF_3COO)_{5.67}(NO_3)_{0.33}(DMF)_2$ and (b) $Ag_{14}Cl(S\text{-}^tBu)_8(CF_3COO)_5(DMF)$. The green semitransparent spheres in the Ag NCs are shown as a visual guide. H atoms have been omitted for clarity. (**C**) Steady-state PL and excitation spectra of 2D CS crystals measured at room temperature (~25 °C). Emission spectra were measured under 365 nm excitation. Reproduced with permission from Reference [158]. Copyright 2019 American Chemical Society.

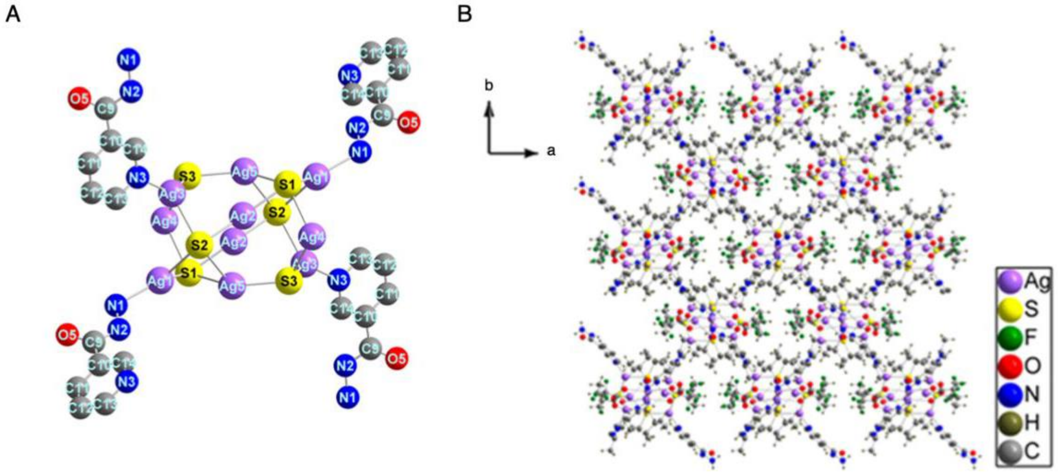

Figure 26. (**A**) Structural unit and (**B**) spatial stacking diagram of $Ag_{10}(CF_3COO)_4(S\text{-}^tBu)_6(CH_3CN)_4(m\text{-iah})_4$. Reproduced with permission from Reference [159]. Copyright 2019 American Chemical Society.

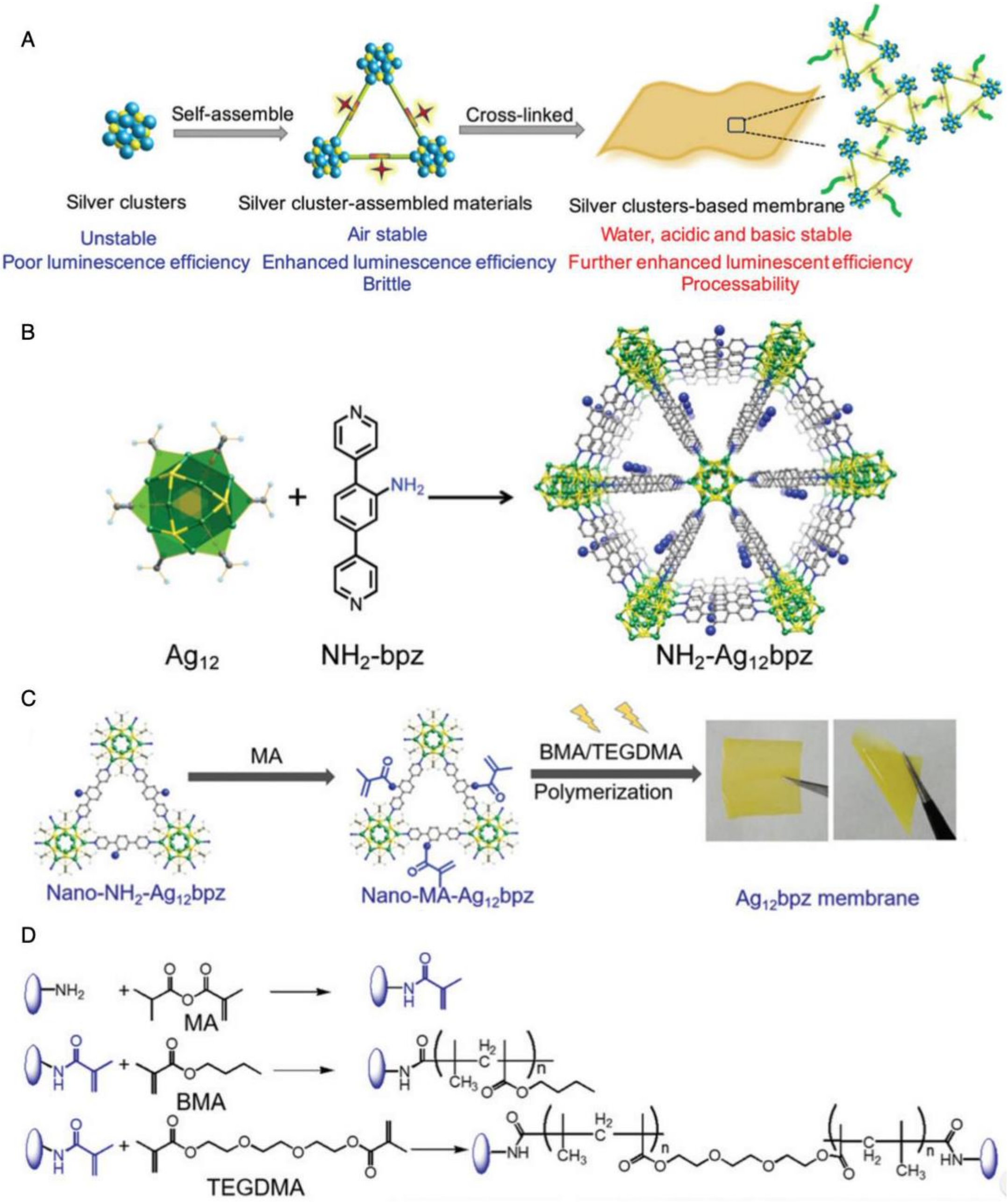

Figure 27. (**A**) Schematic illustration of the fabrication process of an Ag NC-based membrane. (**B**) Structure views of $Ag_{12}(S\text{-}^{t}Bu)_6(CF_3COO)_6(bpz\text{-}NH_2)_3$. (**C**) Fabrication process of the membrane. (**D**) Chemical reactions in the post-modification and cross-linking steps. Reproduced with permission from Reference [172]. Copyright 2019 Royal Society of Chemistry.

The resulting membrane exhibited PL with a QY of 14.8%, which was higher than that of the unpolymerized 2D CS crystals (Figure 28A(a)). The increased PL intensity was ascribed to the polymerization strengthening the structure of the 2D CS, which suppressed molecular vibrations and thus nonradiative decay. The membrane was stable in water regardless of pH (Figure 28A(b)). The researchers also attempted to use the membrane to sense the harmful substance nitrobenzene in solution. The results revealed that the membrane was able to detect nitrobenzene with a sensitivity of 3.19 ppb (Figure 28B). This membrane also displayed high reusability (Figure 28C). These results indicate that polymerizing 2D CSs is an effective approach to obtain Ag NCs suitable for applications.

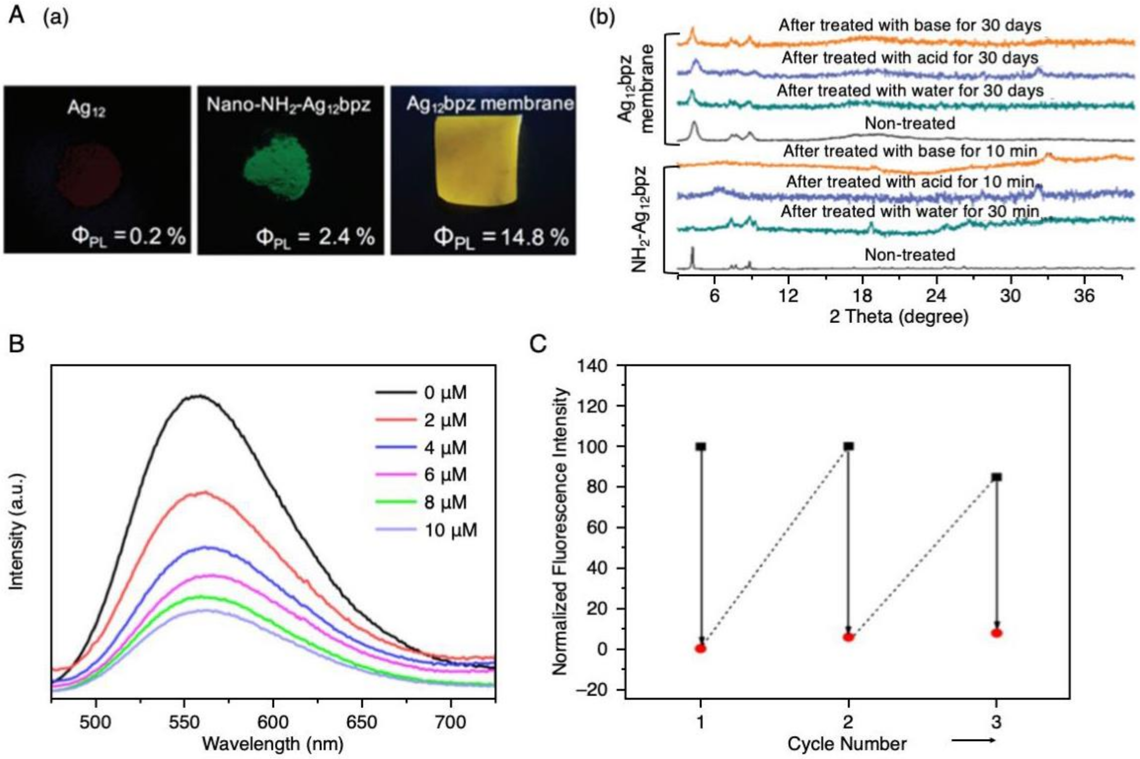

Figure 28. (**A**) (a) Photographs of the Ag_{12} clusters, nano-NH_2-Ag_{12}bpz, and an Ag_{12}bpz membrane under 365 nm ultraviolet light irradiation. (b) PXRD patterns of NH_2-Ag_{12}bpz and the Ag_{12}bpz membrane upon treatment with water, base, and acid for different periods. (**B**) Fluorescence spectra showing the response of the Ag_{12}bpz membrane to the incremental addition of a nitrobenzene solution. (**C**) Cycling test of the Ag_{12}bpz membrane upon exposure to nitrobenzene vapor. Reproduced with permission from Reference [172]. Copyright 2019 Royal Society of Chemistry.

4. Three-Dimensional Structures

Ag NCs are often used as nodes in 3D CSs. Because 3D CSs generally possess stronger frameworks than those of 2D CSs, the formation of 3D CSs is effective to enhance the stability of Ag NCs and thereby improve their physical properties. In 3D CS formation, the principles of NC assembly are similar to those in 1D and 2D CS formation, although the ligands used are often different. In Sections 4.1–4.3, we focus on the assembly of 3D CSs via the formation of Ag−O, Ag−S, or Ag−Cl bonds (Figure 2B), control of counterions (Figure 2C), and the introduction of linker molecules (Figure 2D), respectively. The metal NCs, connection modes, linker molecules, year reported, and reference numbers for these studies are summarized in Table 3. Several of the ligands used in 3D CSs are shown in Scheme 1. The organic molecules used as linkers are illustrated in Scheme 2.

4.1. Connection via Ag−O, Ag−S, or Ag−Cl Bonds

In 2017, Mak et al. [148] formed a 3D CS consisting of $Ag_{14}(S\text{-}i\mathrm{Pr})_6(CF_3COO)_{11}(H_2O)_3(CH_3OH)$ NCs (Figure 29A). The NCs were connected via O−Ag−O bonds formed between CF_3COO^- and Ag ions (Figure 29B,C). Each Ag NC was connected to six other NCs, thereby forming a distorted octahedral-like coordination structure. It was speculated that this 3D CS formed by the assembly of NCs after NC generation.

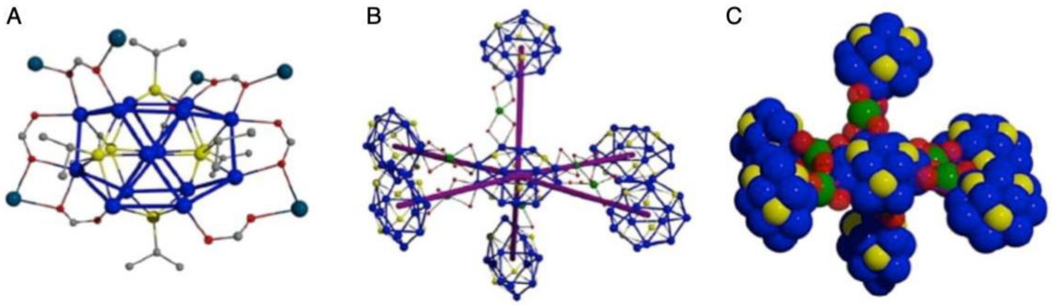

Figure 29. (**A**) Perspective view of $Ag_{14}(S\text{-}i Pr)_6(CF_3COO)_{11}(H_2O)_3(CH_3OH)Ag_3$. (**B**) Ball-and-stick and (**C**) space-filling diagrams showing the spatial arrangement of a central cluster surrounded by six adjacent clusters. Ag = blue, cyan, and green, S = yellow, O = red, C = gray. Reproduced with permission from Reference [148]. Copyright 2017 Wiley-VCH.

In 2019, Sun and colleagues also produced a 3D CS, and theirs consisted of $Ag_{44}(Mo_6O_{19})(S\text{-}Et)_{24}(SCl_4)_3$ NCs (Figure 30A) containing a POM as an anion template (Figure 30B); these NCs were reported in their paper on 1D CS (Figure 9) and 2D CS (Figure 19) formation [149]. In this 3D CS, $Mo_6O_{19}{}^{2-}$ was used as an anion template, which was different from the case of the 1D and 2D CSs, in which the POM $V_{10}O_{28}{}^{6-}$ was located in the center of the cluster. This was the first report in which $Mo_6O_{19}{}^{2-}$ was used as an anion template of Ag NCs. $Mo_6O_{19}{}^{2-}$ has octahedral symmetry, and thereby the outer $Ag_{44}(S\text{-}Et)_{24}$ layer also displayed high symmetry (Figure 30C). The Ag_{44} shell had six quadrangles and 24 pentagonal faces. Ag at the vertices of these six quadrangles was connected with one S atom and four Cl atoms, leading to the formation of a 3D CS consisting of $Ag_{44}(Mo_6O_{19})(S\text{-}Et)_{24}(SCl_4)_3$ (Figure 30D). The S and Cl atoms used in the connections were generated by the decomposition of S-Et and CH_2Cl_2 during the CS synthesis.

The 3D CS in which Ag NCs are linked by dithiocarb, reported in 2019 by Gao et al. [173], should also be included in this category. The researchers first synthesized an $Ag_{11}S(C_5NS_2H_{10})_9$ precursor ($C_5NS_2H_{10}$ = diethyldithiocarbamate, Scheme 1(20)) [174]. The obtained precursor was reacted under high pressure, in an autoclave, to form a 3D CS with $Ag_{17}(C_5NS_2H_{10})_{14}$ as a repeating unit. This structure consists of Ag_9 NCs bound to twelve $C_5NS_2H_{10}$ (Figure 31A) and Ag_5 NCs containing six $C_5NS_2H_{10}$ (Figure 31B). The 3D CS (Figure 31C) was formed by the sharing of S between the two types of NCs. In these structures, the Ag_9 NCs were the nodes for three-point bridges and the Ag_5 NCs were the nodes for four-point bridges.

Table 3. Connection modes, NCs, linkers, publication years, and references for 3D CS.

Connection Mode	NC or Metal Ion	Linker	Year	Ref.
Formation of Ag–O, Ag–S, Ag–Cl bond, etc. (Figure 2B)	$Ag_{14}(S\text{-}i Pr)_6(CF_3COO)_{11}(H_2O)_3(CH_3OH)$	-	2017	[148]
	$Ag_{44}(Mo_6O_{19})(S\text{-}Et)_{24}(SCl_4)_3$	-	2019	[149]
	$Ag_{17}(C_5NS_2H_{10})_{14}$	-	2019	[173]
Control of counter ion (Figure 2C)	$[Au_1Ag_{22}(S\text{-}Adm)_{12}Cl]^{2+}$	$SbF_6{}^-$	2020	[175]
	$[Au_1Ag_{22}(S\text{-}Adm)_{12}]^{3+}$	$SbF_6{}^-$		
Introduction of linker molecule (Figure 2D)	$Ag_{12}(S\text{-}{}^tBu)_8(CF_3COO)_4$	bpy [a]	2017	[168]
	$Ag_{14}(DT\text{-}o\text{-}C)_6$	1,4-bis(4- pyridyl)benzene [a]	2018	[156]
	$Ag_{10}(S\text{-}{}^tBu)_6(CF_3COO)_2(PhPO_3H)_2$	bpy [a]	2018	[176]
	$Ag_{12}(S\text{-}{}^tBu)_6(CF_3COO)_6$	CPPP [a]	2019	[177]
	$Ag_{12}(S\text{-}{}^tBu)_6(CF_3COO)_6$ $Ag_8(S\text{-}{}^tBu)_4(CF_3COO)_4$	tppe [a]	2019	[178]
	Ag^+	$[C(Au\text{-}mdppz)_6](BF_4)_2$ [a]	2014	[179]

[a] See Scheme 2.

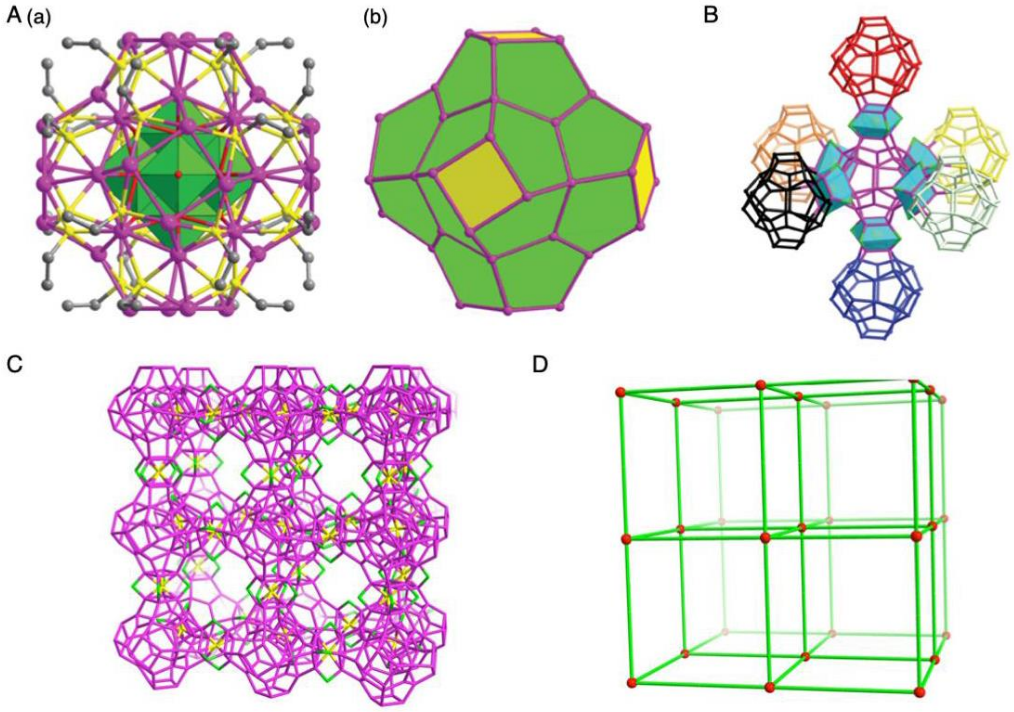

Figure 30. (**A**) Structure of (a) $Ag_{44}(Mo_6O_{19})(S\text{-}Et)_{24}(SCl_4)_3$ and (b) the $Mo_6O_{19}{}^{2-}$ anion template. Tetragons (yellow) and pentagons (green) in an Ag_{44} cage are shown. (**B**) Connections (cyan polyhedra) between Ag_{44} subunits (highlighted in different colors) in the 3D framework. (**C**) Framework and (**D**) simplified primitive cubic topology with the Ag_{44} subunit as a node (represented as red balls) of the $Ag_{44}(Mo_6O_{19})(S\text{-}Et)_{24}(SCl_4)_3$ 3D CS. Reproduced with permission from Reference [149]. Copyright 2019 Royal Society of Chemistry.

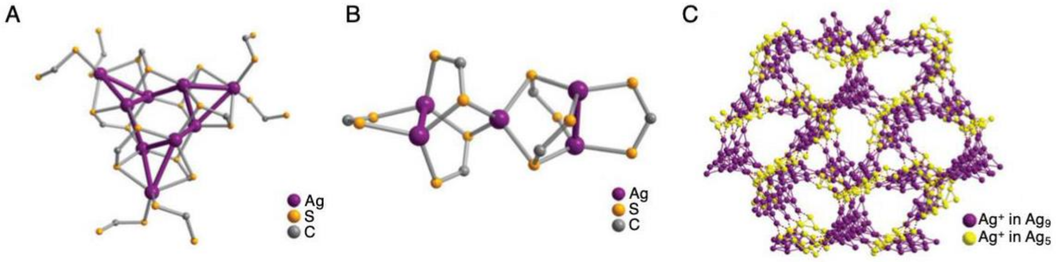

Figure 31. (**A**) Structures of the Ag_9 cluster, (**B**) Ag_5 subunits, and (**C**) 3D framework of $Ag_{17}(C_5NS_2H_{10})_{14}$. Reproduced with permission from Reference [173]. Copyright 2019 Royal Society of Chemistry.

4.2. Control of Counterions

Very recently, Zhu's group synthesized two types of 3D CSs in which $[Au_1Ag_{22}(S\text{-}Adm)_{12}]^{3+}$ NCs (S-Adm = 1-adamantanethiolate, Scheme 1(21)) were connected in three dimensions via hexafluoroantimonate ions ($SbF_6{}^-$) [175]. The $[Au_1Ag_{22}(S\text{-}Adm)_{12}]^{3+}$ node had a geometric structure in which an icosahedral Au_1Ag_{12} alloy core (Figure 32A(a)) was surrounded by an oligomer with a chemical composition of $Ag_{10}(S\text{-}Adm)_{12}$ (Figure 32A(b),(c)). The $[Au_1Ag_{22}(S\text{-}Adm)_{12}]^{3+}$ NCs formed as a pair of optical isomers, depending on the winding method of the oligomer (Figure 32A(b),(c)). In the first 3D CS, $[Au_1Ag_{22}(S\text{-}Adm)_{12}](SbF_6)_2Cl$ was a structural unit, and two $SbF_6{}^-$ were connected to $[Au_1Ag_{22}(S\text{-}Adm)_{12}]^{3+}$ via an Ag−F−Ag bond, to form the 3D CS (Figure 32A(d),(e)). This 3D CS possessed a diamondlike structure (Figure 32A(f)) consisting of interpenetrating clockwise and counterclockwise optical isomers (Figure 32A(g)), which led to a small pore diameter of 6.2 Å (Figure 32A(h)). In the second 3D CS, $[Au_1Ag_{22}(S\text{-}Adm)_{12}](SbF_6)_3$ was a structural unit, and the

3D CS was formed by connecting $[Au_1Ag_{22}(S\text{-}Adm)_{12}]^{3+}$ to three SbF_6^- via Ag−F−Ag bonds (Figure 32B(a)–(c)). This structure only contained clockwise or counterclockwise optical isomers (Figure 32B(d)). As a result, this 3D CS had a larger pore diameter (15 Å, Figure 32B(e)) than that of the first 3D CS (6.2 Å, Figure 32A).

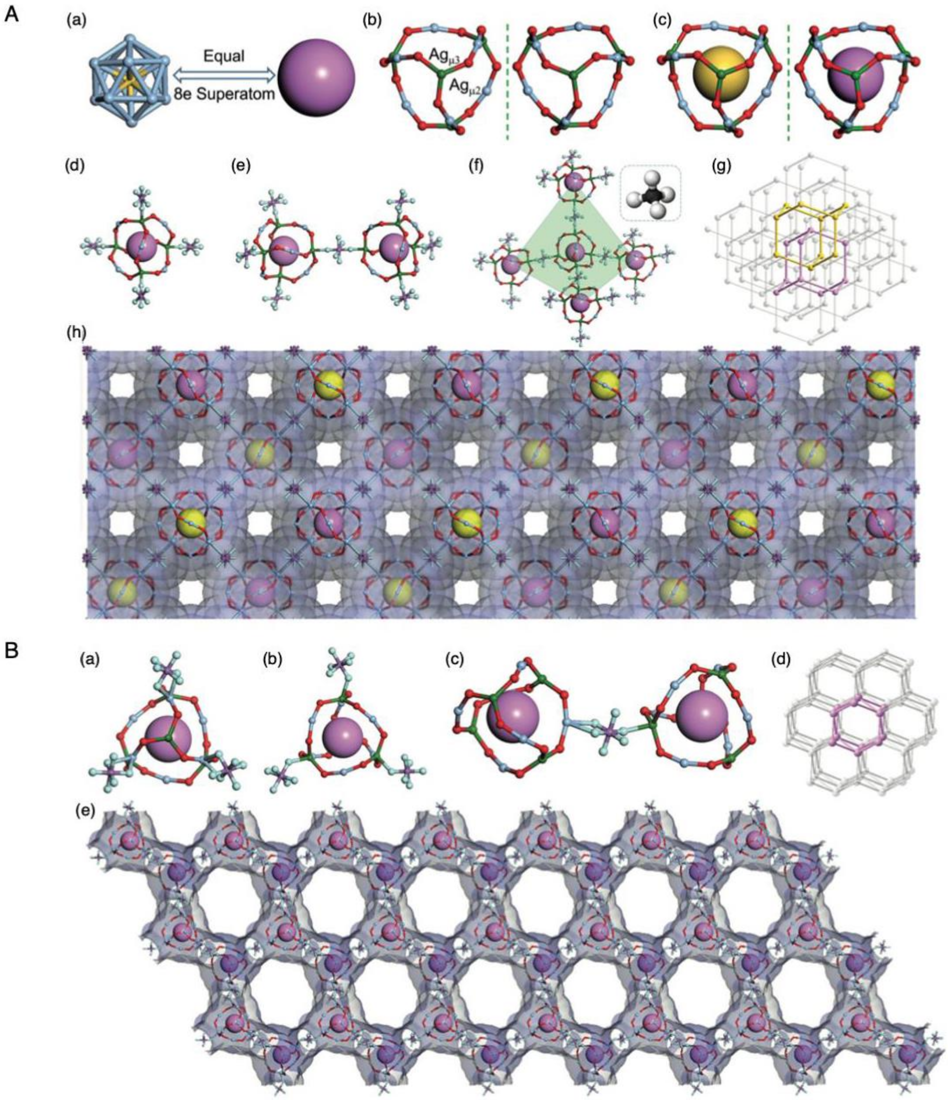

Figure 32. (**A**) Structure of the Au_1Ag_{22} superatom complex and interpenetrating 3D channel framework assembled from alloy NC monomers (for clarity, C and H atoms are omitted). (a) Icosahedral Au_1Ag_{12} core, (b) cage-like $Ag_{10}(SR)_{12}$ complex shell, (c) a pair of Au_1Ag_{22} isomers, (d) the connection of SbF_6^- and alloy NCs, (e) two alloy NCs connected by SbF_6^-, (f) tetrahedral structure of NC monomers (the inset shows methane), (g) topology of the diamond-like structure, and (h) interconnected channels of Au_1Ag_{22} along the *z*-axis. The left- and right-handed enantiomers in (c), (g), and (h) are highlighted in pink and yellow, respectively. Atoms are denoted in conventional colors: Au = gold, Ag in core and the Agμ2 motif = pale blue, Ag in the Agμ3 motif = green, S = red, F = light turquoise, Sb = purple. (**B**) Crystal and channel structure of left-handed chiral 3D channel framework (C and H atoms are omitted for clarity). (a) The connection of Ag and SbF_6^-, (b) the connection of Ag and SbF_6^-, (c) two alloy NCs linked by SbF_6^-, (d) illustration of the hexagonal network structure, and (e) schematic of the large hexagonal channel structure. Note that the packing pattern of the right-handed chiral 3D channel framework was the same as that of the left-handed chiral 3D channel framework. Reproduced with permission from Reference [175]. Copyright 2020 Wiley-VCH.

Study of the physical and chemical properties of the 3D CSs revealed that both exhibited red PL in the presence of polar solvents such as CH_3OH, ethanol, and water, which disappeared when the solvent was evaporated (Figure 33A). This behavior indicates that the obtained 3D CSs can function as sensors for polar solvents. The 3D CS composed of only the right- or left-handed enantiomer exhibited circularly polarized luminescence (CPL) (Figure 33B).

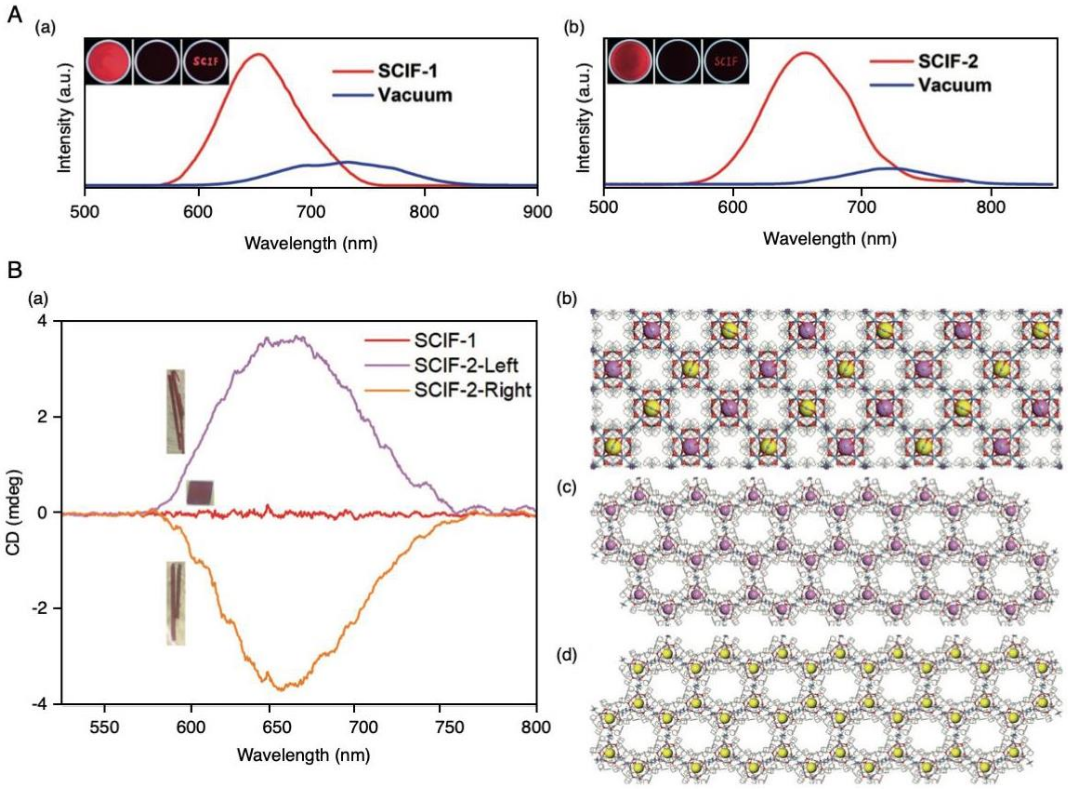

Figure 33. (**A**) Luminescence switching response to protic solvents. Fluorescence of films coated with (a) the interpenetrating 3D CS (SCIF-1) and (b) the left-handed 3D CS (SCIF-2) before and after solvent evaporation. Inset images show solvatochromic photographs of the corresponding films excited with 365 nm ultraviolet light before (left) and after desolvation (middle), and fluorescence recovery after treatment with *n*-hexane containing 5% ethanol (right). (**B**) CPL spectra of SCIF-1, SCIF-2 (left-handed), and SCIF-2 (right-handed) single crystals and the superstructures of these three crystal samples. (a) CPL spectra of SCIF-1, SCIF-2 (left-handed), and SCIF-2 (right-handed). Insets show photographs of the corresponding crystals. (b) Crystal structure of the SCIF-1 framework. (c) Crystal structure of the SCIF-2 (left-handed framework). (d) Crystal structure of the SCIF-2 (right-handed) framework. Reproduced with permission from Reference [175]. Copyright 2020 Wiley-VCH.

4.3. Introduction of Linker Molecules

The formation of 3D CSs by using linker molecules is a technique often used to fabricate molecular assemblies and MOFs. When a 3D CS composed of metal NCs is formed by such a method, in addition to increasing the stability of the NCs, it is also expected to adsorb gas molecules within its pores and behave as a catalyst with high selectivity because of the narrow pores. Furthermore, because the metal NCs, which are used as nodes, have more diversity in terms of coordination direction than that of metal ions, metal NC-based MOFs may have different connection modes from those of normal MOFs formed by using metal ions as nodes, and thereby they construct novel framework structures. Thus, metal NC-based MOFs possess not only the characteristics of individual metal NCs and MOFs, but also the possibility to produce new functions through synergistic effects.

Zang's group have been energetically researching 3D CSs with linkers, as well as the cases of 1D and 2D CSs. First, in 2017, Zang et al. [168] formed an Ag_{12} NC-based MOF ($Ag_{12}(S\text{-}^{t}Bu)_8(CF_3COO)_4(bpy)_4$)

in which $Ag_{12}(S\text{-}^tBu)_8(CF_3COO)_4$ was bridged by bpy (Figure 34A). The obtained Ag_{12} NC-based MOF possessed a bilayer structure (Figure 34B). The formation of such a 3D CS markedly improved the stability of the Ag_{12} NCs. For example, a crystal of the individual $Ag_{12}(S\text{-}^tBu)_6(CF_3COO)_6(CH_3CN)_6$ NCs discolored in just 30 min when left in the atmosphere. In contrast, the Ag_{12} NC-based MOF showed almost no change in crystallinity, even when left in the air for one year (Figure 34C). The 3D CS also showed high stability during long-term gas adsorption and irradiation with visible light for several hours.

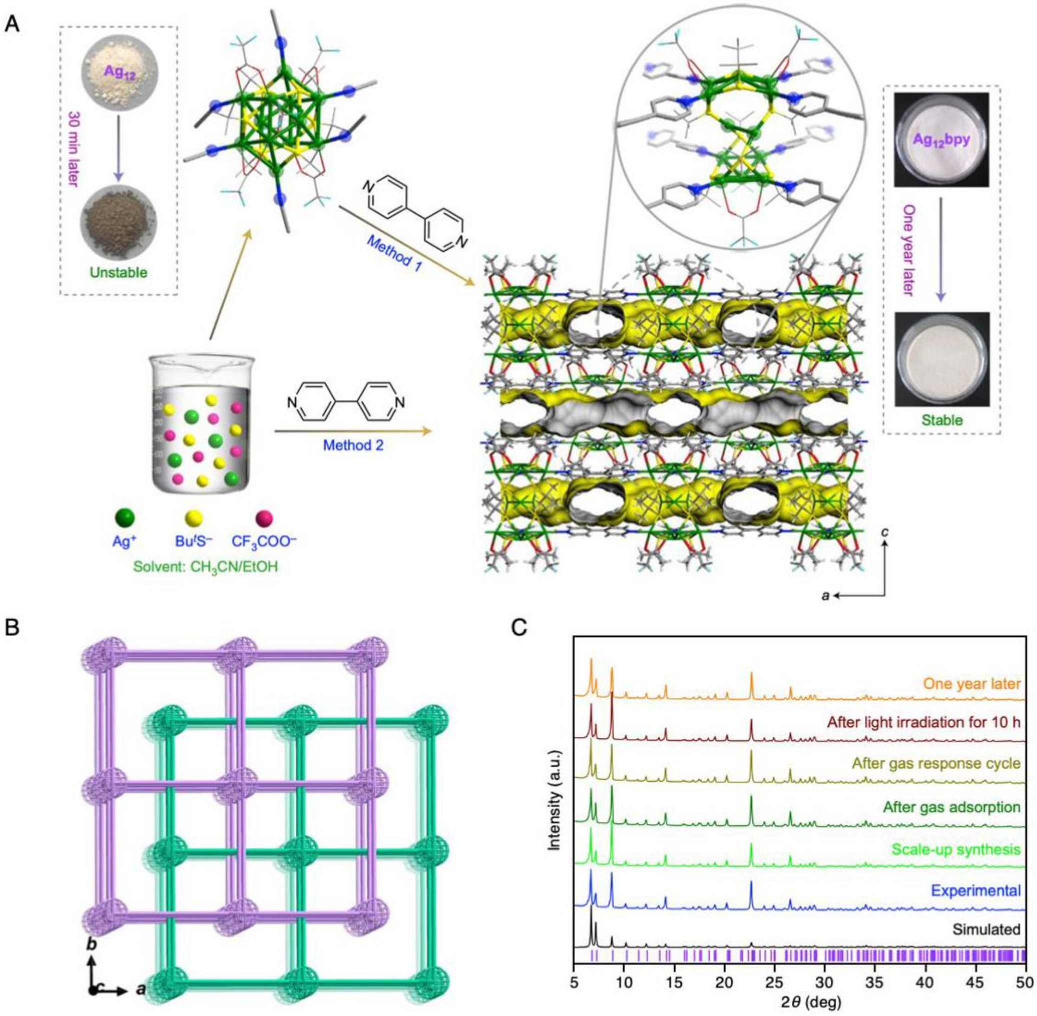

Figure 34. (**A**) Schematic representation of the ligand-exchange strategy used to obtain $Ag_{12}(S\text{-}^tBu)_8(CF_3COO)_4(bpy)_4$ crystals (Method 1, giving low yield) and one-pot synthesis (Method 2, for gram-quantity production) under identical conditions. Interconnected channels of $Ag_{12}(S\text{-}^tBu)_8(CF_3COO)_4(bpy)_4$ viewed along the *a* and *b* axes, where the yellow surface represents the pore surface. Ag = green, C = gray, O = red, S = yellow, F = turquoise. H atoms are omitted for clarity. Inset are photographs showing the changes of $Ag_{12}(S\text{-}^tBu)_6(CF_3COO)_6(CH_3CN)_6$ and $Ag_{12}(S\text{-}^tBu)_8(CF_3COO)_4(bpy)_4$ crystals under ambient conditions. (**B**) Schematic representation of the topology of $Ag_{12}(S\text{-}^tBu)_8(CF_3COO)_4(bpy)_4$ along the *c*-axis. The square windows in one double layer are blocked by Ag–S cluster nodes of adjacent layers. (**C**) PXRD patterns of $Ag_{12}(S\text{-}^tBu)_8(CF_3COO)_4(bpy)_4$ (in ascending order): simulated, experimental, gram-scale synthesis, after gas adsorption experiments (O_2, N_2, ethanol), after sensing experiments (O_2/N_2, O_2/vacuum, ethanol/air), after 10 h of visible-light irradiation under a Xe lamp equipped with a 420 nm cutoff filter, and the sample vial after one year under ambient conditions. Reproduced with permission from Reference [168]. Copyright 2017 Springer-Nature.

The formation of the 3D CS greatly changed the PL properties of the NCs. The individual Ag_{12} NCs exhibited red PL with low QY. Conversely, the Ag_{12} NC-based MOF exhibited green PL under vacuum, which was quenched by O_2 in the atmosphere (Figure 35A). The PL emission wavelength of the 3D CS under vacuum was independent of temperature and excitation wavelength, and its QY was 60 times higher than that of individual Ag_{12} NCs. The authors ascribed this high QY to the efficient suppression of nonradiative decay in the 3D CS. Moreover, the fact that the PL of the 3D CS is quenched by O_2 means that it is highly sensitive to O_2. The 3D CS showed a fast response to O_2 in experiments in which the atmosphere was repeatedly switched between air and N_2. No such O_2 response was observed for the individual Ag_{12} NCs. Based on these results, they suggested that the Ag_{12} NC-based MOF can be applied as an O_2 sensor. In addition, the Ag_{12} NC-based MOF was able to adsorb volatile organic compounds (VOCs) in its pores. The VOC-containing Ag_{12} NC-based MOF exhibited different PL colors, depending on the kind of VOC (Figure 35B). This indicates that the Ag_{12} NC-based MOF displays solvatochromism and therefore can be used for VOC detection.

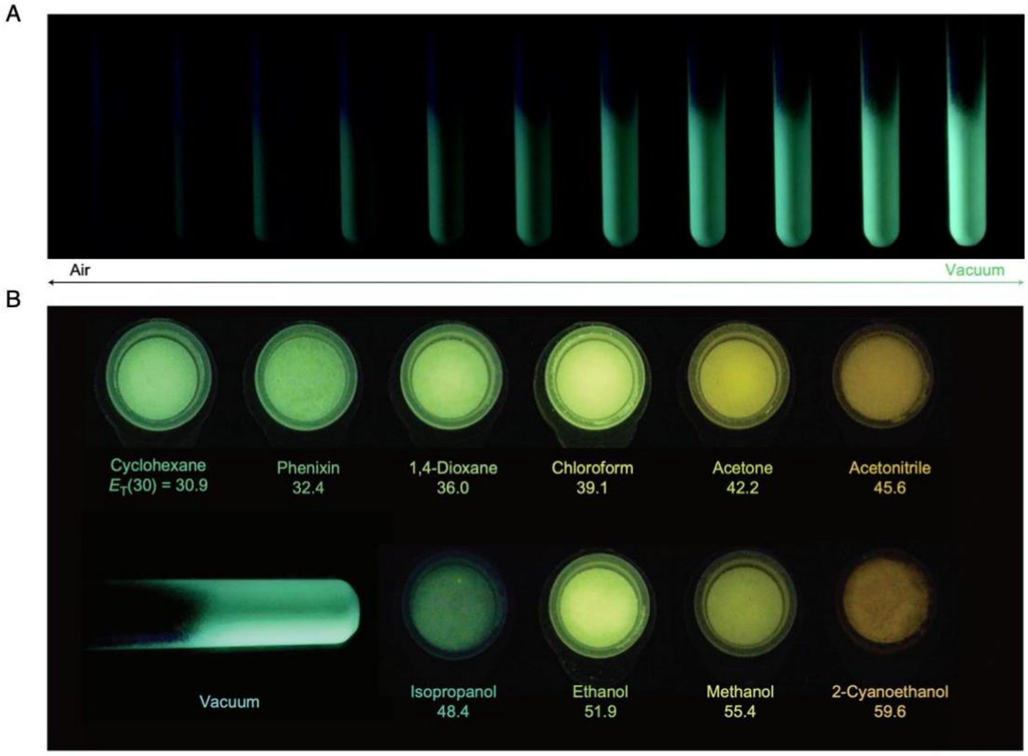

Figure 35. (**A**) Photographs of $Ag_{12}(S\text{-}^tBu)_8(CF_3COO)_4(bpy)_4$ excited by 365 nm light in a glass tube, beginning under vacuum and then filling with air (from left to right). (**B**) Photographs of the luminescence responses of $Ag_{12}(S\text{-}^tBu)_8(CF_3COO)_4(bpy)_4$ to different VOCs under 365 nm ultraviolet light irradiation. Reproduced with permission from Reference [168]. Copyright 2017 Springer-Nature.

In a paper on Ag_{14}(DT-*o*-C$)_6$ NCs published in 2018 (Figures 13 and 22), the same group reported that a 3D CS containing Ag_{14}(DT-*o*-C$)_6$ NCs formed when bpy was used as a linker (Figure 36A) [156]. The Ag_{14} NC nodes in the 3D CS had a face-centered cubic structure like that of other Ag_{14} NCs. This 3D CS was formed by connecting the eight vertices of each Ag_{14} NC with bpy linker molecules. However, this 3D CS was not stable after solvent evaporation, similar to the case of the corresponding 1D CS (Figure 13) and 2D CS (Figure 22) [156]. Therefore, they synthesized a 3D CS with an interpenetrating framework by using 1,4-bis(4-pyridyl)benzene (Scheme 2(14)) as a linker, in order to decrease the pore size and form a 3D CS with a strong framework (Figure 36B). The obtained 3D CS showed high thermal stability, remaining intact up to 220 °C (Figure 36C), and possessed pores with a diameter of about 1.12 nm (Figure 36D). This 3D CS showed optical absorption over a wide wavelength range and thermochromism (Figure 36E).

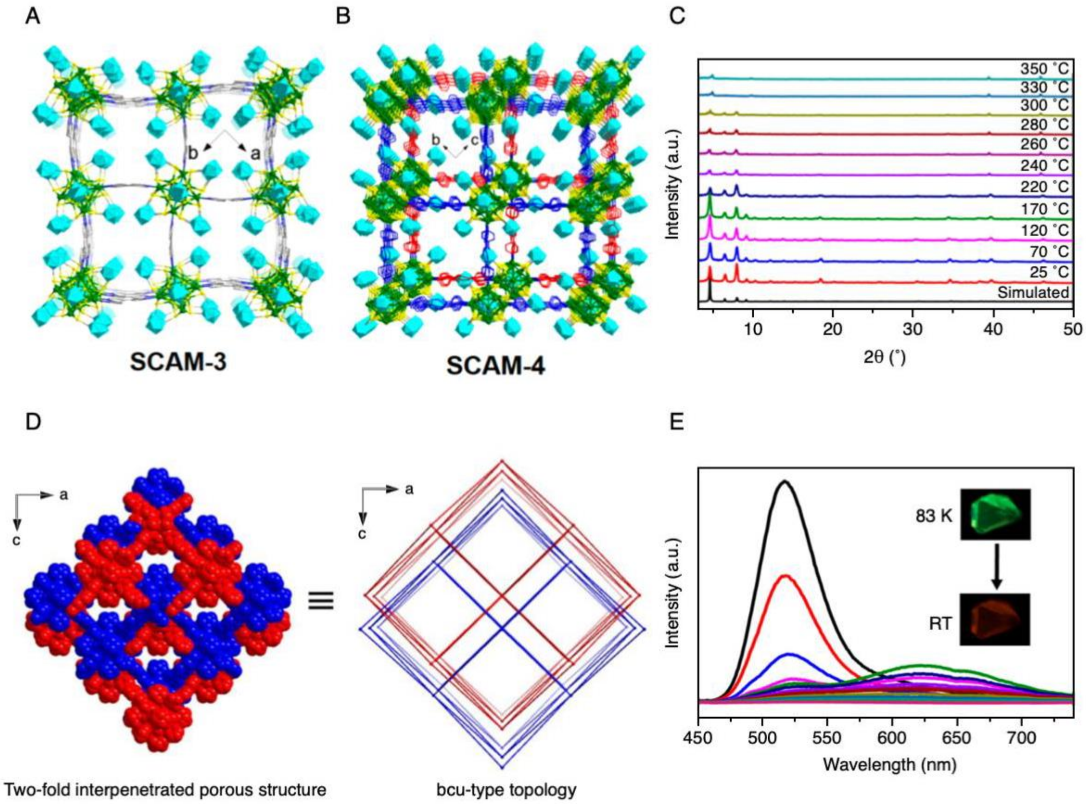

Figure 36. Three-dimensional CSs composed of (**A**) $Ag_{14}(DT\text{-}o\text{-}C)_6$ NCs and bpy (SCAM-3) and (**B**) $Ag_{14}(DT\text{-}o\text{-}C)_6$ NCs and 1,4-bis(4-pyridyl)benzene (SCAM-4). (**C**) Variable-temperature PXRD of SCAM-4 from 25 to 350 °C. (**D**) Different view of SCAM-4. (**E**) Evacuated SCAM-4 (excited at 380 nm) from −190 to 25 °C in air. Inset are corresponding photographs of SCAM-4 under 365 nm ultraviolet light irradiation. Reproduced with permission from Reference [156]. Copyright 2018 American Chemical Society.

Zang et al. [176] have also produced several other functional Ag NC-based MOFs. For example, in 2018, they reported the synthesis of a flexible Ag NC-based MOF. This structure consisted of 2D layers of $Ag_{10}(S\text{-}^tBu)_6(CF_3COO)_2(PhPO_3H)_2$ NCs linked via bpy, which were stacked through hydrogen bond (O-H···O) and C-H···O interactions, to form the 3D CS (Figure 37A,B). The 2D CS layers were thus linked by weak interactions, which facilitated the sliding of the layers, allowing the 3D CS to undergo structural deformation in response to guest organic molecules (Figure 37C). This Ag_{10} NC-based MOF exhibited green PL in air. Upon inclusion of guest organic molecules, it exhibited PL with an emission color depending on the guest organic molecule (Figure 37D). As such, this Ag_{10} NC-based MOF has potential as a sensor for distinguishing VOCs by its PL color. In 2019, they also formed a 3D CS consisting of $Ag_{12}(S\text{-}^tBu)_6(CF_3COO)_6$ NC nodes and 2,5-bis(4-cyanophenyl)-1,4-bis(4-(pyridine-4-yl)-phenyl)-1,4-dihydropyrrolo[3,2-b]pyrrole (CPPP, Scheme 2(15)) as a linker (Figure 38A) [177]. This was the first report in which a nitrile group (-CN) was used to link Ag NCs. The obtained 3D CS exhibited PL with a higher QY (61%) than that of CPPP in solution and solid states because the aggregation-induced quenching of CPPP was suppressed in the 3D CS (Figure 38B).

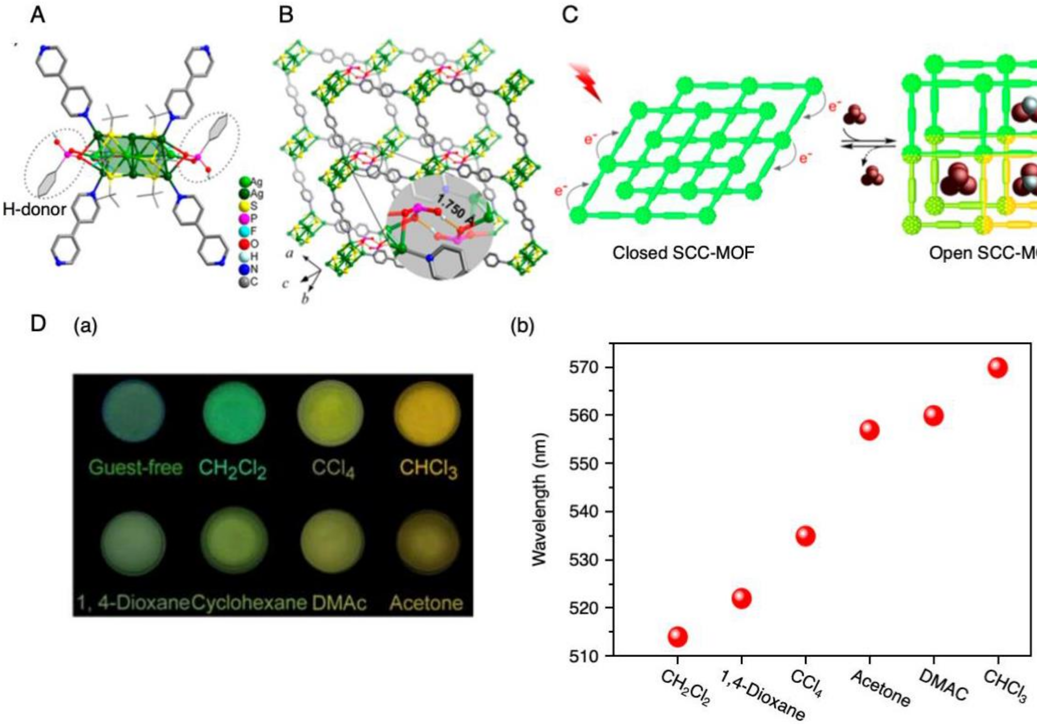

Figure 37. (**A**) Perspective view of the coordination environment of the $Ag_{10}(S\text{-}^tBu)_6$ core in $Ag_{10}(S\text{-}^tBu)_6(CF_3COO)_2(PhPO_3H)_2(bpy)_2$ at −173 °C. (**B**) Two-layer stack of the host framework of $Ag_{10}(S\text{-}^tBu)_6(CF_3COO)_2(PhPO_3H)_2(bpy)_2$ with complementary hydrogen bonding (O−H···O; the H···O distance is 1.750 Å) between interlayer $-PO_2OH$ moieties. (**C**) Illustration of reversible pore open/closed structural transformation induced by CH_2Cl_2, $CHCl_3$, and CCl_4 (represented as space-filling models) and switchable solvatochromism. (**D**) (a) Luminescence images of $Ag_{10}(S\text{-}^tBu)_6(CF_3COO)_2(PhPO_3H)_2(bpy)_2$/solvent (guest free, CH_2Cl_2, $CHCl_3$, CCl_4, 1,4-dioxane, cyclohexane, DMAC, and acetone) combinations under 365 nm ultraviolet light irradiation. (b) Emission maxima of various $Ag_{10}(S\text{-}^tBu)_6(CF_3COO)_2(PhPO_3H)_2(bpy)_2$/solvent combinations at room temperature. Reproduced with permission from Reference [176]. Copyright 2018 American Chemical Society.

In the above 3D CSs, the nodes consisted of only one kind of Ag NCs. Tang et al. [178] synthesized an Ag NC-based MOF that had two types of Ag NCs as nodes. This Ag NC-based MOF was composed of 1,1,2,2-tetrakis(4-(pyridin-4-yl)phenyl)-ethene (tppe, Scheme 2(16)), $Ag_{12}(S\text{-}^tBu)_6(CF_3COO)_6$, and $Ag_8(S\text{-}^tBu)_4(CF_3COO)_4$ (Figure 39). In the 3D CS, one $Ag_{12}(S\text{-}^tBu)_6(CF_3COO)_6$ NC and three $Ag_8(S\text{-}^tBu)_4(CF_3COO)_4$ NCs were bound to the four N atoms of tppe. The estimated pore volume of this Ag NC-based MOF was 40.9%. DMAC, which was used as a solvent in the synthesis, was present in the pores of the 3D CS immediately after synthesis (Figure 40A). When the obtained 3D CS was exposed to the atmosphere, DMAC was removed, while maintaining the framework of the 3D CS. The Ag NC-based MOF thus obtained exhibited PL in the visible region because tppe is a light-emitting molecule. The PL wavelength of the 3D CS depended on the presence or absence of DMAC in its pores (Figure 40B). When DMAC was present in the pores of the framework, intramolecular rotation of tppe was suppressed, which changed the excited-state dynamics of the 3D CS. The change in the emission behavior of the Ag NC-based MOF induced by DMAC was ascribed to this change of its excited-state characteristics (Figure 40C).

Wang and colleagues reported the formation of a 3D CS, using metal NCs as linkers, before the use of metal NCs as nodes was developed [179]. In 2014, they succeeded in forming an NbO-type MOF by using Ag ions as nodes and $[C(Au\text{-}mdppz)_6](BF_4)_2]$ (mdppz = 2-(3-methylpyrazinyl)diphenylphosphine, Scheme 2(17)) NCs as linkers (Figure 41). $[C(Au\text{-}mdppz)_6](BF_4)_2$ has a framework with C in the center

(Figure 41A) and is luminescent. The 3D CS was formed by the outer N atom of mdppz (Scheme 2(17)) binding to an Ag ion (Figure 41B,C). The obtained 3D CS consisted of two interpenetrating frameworks (Figure 41D,E) with a 1D channel in the *c*-axis direction (Figure 41C). Because a luminescent NC was used as the linker, the obtained MOF also showed green PL. The 3D CS displayed a PL QY of 25.6%, which was much higher than that of the luminescent NCs (1.5%). This increase of QY was caused by the strengthening of the framework of the linker NCs upon MOF formation and the excited-state perturbation induced by the coordination of Ag ions.

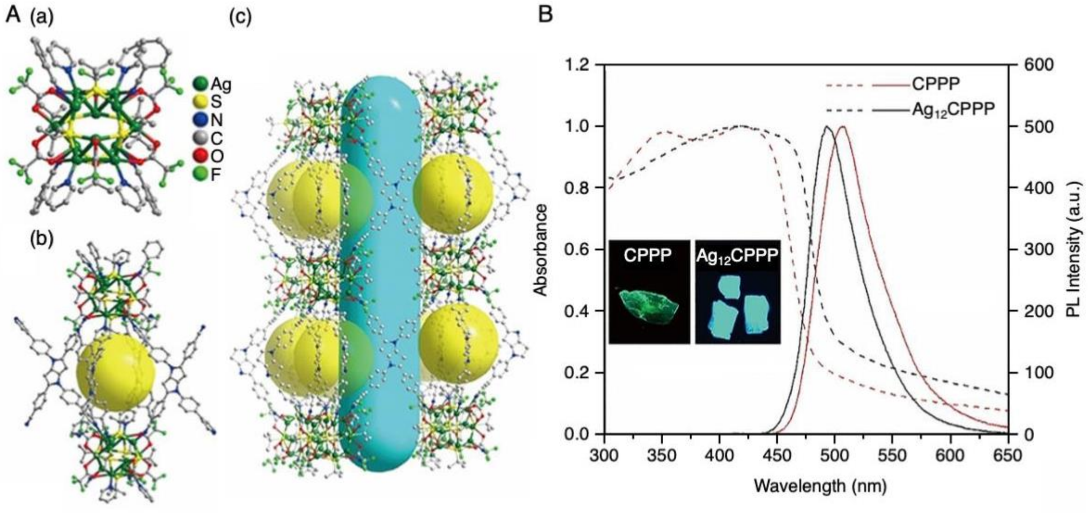

Figure 38. (**A**) Structures of (a) Ag chalcogenolate cluster nodes, (b) cage in $Ag_{12}(S\text{-}^{t}Bu)_6(CF_3COO)_6(CPPP)_2$ (Ag_{12}CPPP), and (c) distribution of the cages in Ag_{12}CPPP. All H atoms and guest solvent molecules are omitted for clarity. (**B**) Solid-state absorption (dashed lines) and emission (solid lines) spectra of Ag_{12}CPPP and CPPP at room temperature. Inset are photographs of the crystals of CPPP and Ag_{12}CPPP under 365 nm ultraviolet light irradiation. Reproduced with permission from Reference [177]. Copyright 2019 Wiley-VCH.

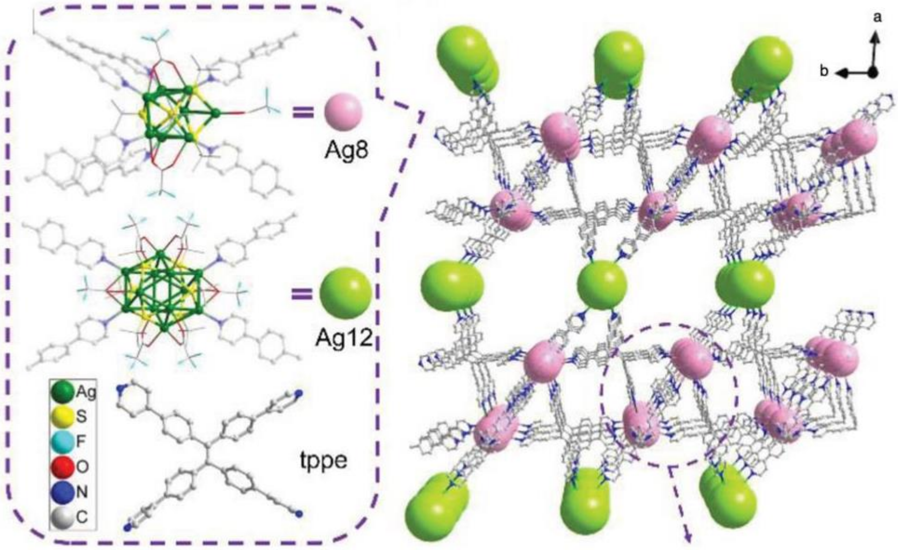

Figure 39. Structure of the Ag_8 cluster, Ag_{12} cluster, and tppe ligand, and single net of the $[Ag_{12}(S\text{-}^{t}Bu)_6(CF_3COO)_6]_{0.5}[Ag_8(S\text{-}^{t}Bu)_4(CF_3COO)_4](tppe)_2(DMAC)_{10}$ framework viewed along the *c*-axis. DMAC molecules are omitted for clarity. Reproduced with permission from Reference [178]. Copyright 2019 Wiley-VCH.

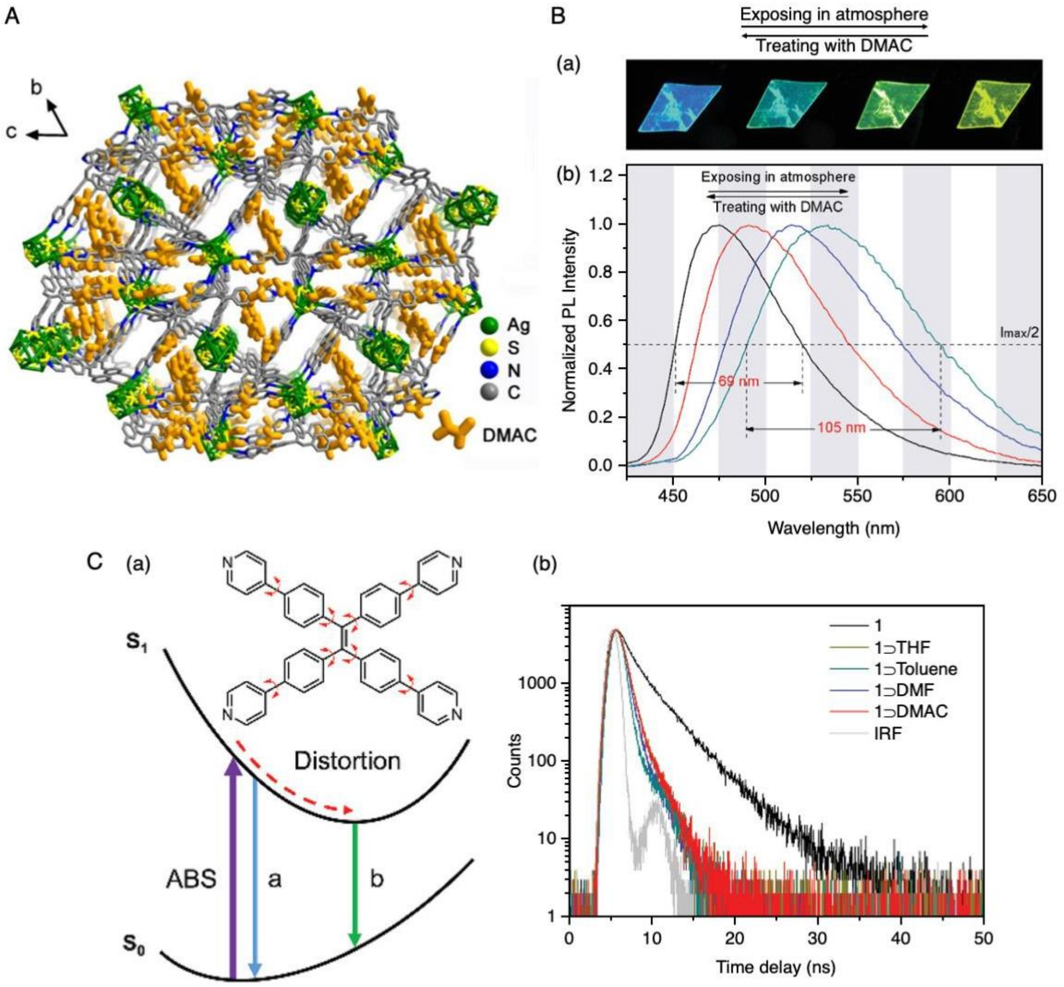

Figure 40. (**A**) Distribution of DMAC molecules in the $[Ag_{12}(S\text{-}^tBu)_6(CF_3COO)_6]_{0.5}[Ag_8(S\text{-}^tBu)_4(CF_3COO)_4](tppe)_2(DMAC)_{10}$ framework. (**B**) (a) Gradual fluorescence changes of the same $[Ag_{12}(S\text{-}^tBu)_6(CF_3COO)_6]_{0.5}[Ag_8(S\text{-}^tBu)_4(CF_3COO)_4](tppe)_2(DMAC)_{10}$ crystal under atmospheric exposure and (b) normalized fluorescence spectra of $[Ag_{12}(S\text{-}^tBu)_6(CF_3COO)_6]_{0.5}[Ag_8(S\text{-}^tBu)_4(CF_3COO)_4](tppe)_2(DMAC)_{10}$. (**C**) (a) Proposed fluorescence decay paths in $[Ag_{12}(S\text{-}^tBu)_6(CF_3COO)_6]_{0.5}[Ag_8(S\text{-}^tBu)_4(CF_3COO)_4](tppe)_2(DMAC)_{10}$ (path a) and $[Ag_{12}(S\text{-}^tBu)_6(CF_3COO)_6]_{0.5}[Ag_8(S\text{-}^tBu)_4(CF_3COO)_4](tppe)_2$ (**1**) (path b) and (b) fluorescence decay profiles of $[Ag_{12}(S\text{-}^tBu)_6(CF_3COO)_6]_{0.5}[Ag_8(S\text{-}^tBu)_4(CF_3COO)_4](tppe)_2$ in DMAC, THF, toluene, and DMF (denoted as $\mathbf{1}\supset\bigcap$DMAC, $\mathbf{1}\supset\bigcap$THF, $\mathbf{1}\supset\bigcap$Toluene, and $\mathbf{1}\supset\bigcap$DMF, respectively). Reproduced with permission from Reference [178]. Copyright 2019 Wiley-VCH.

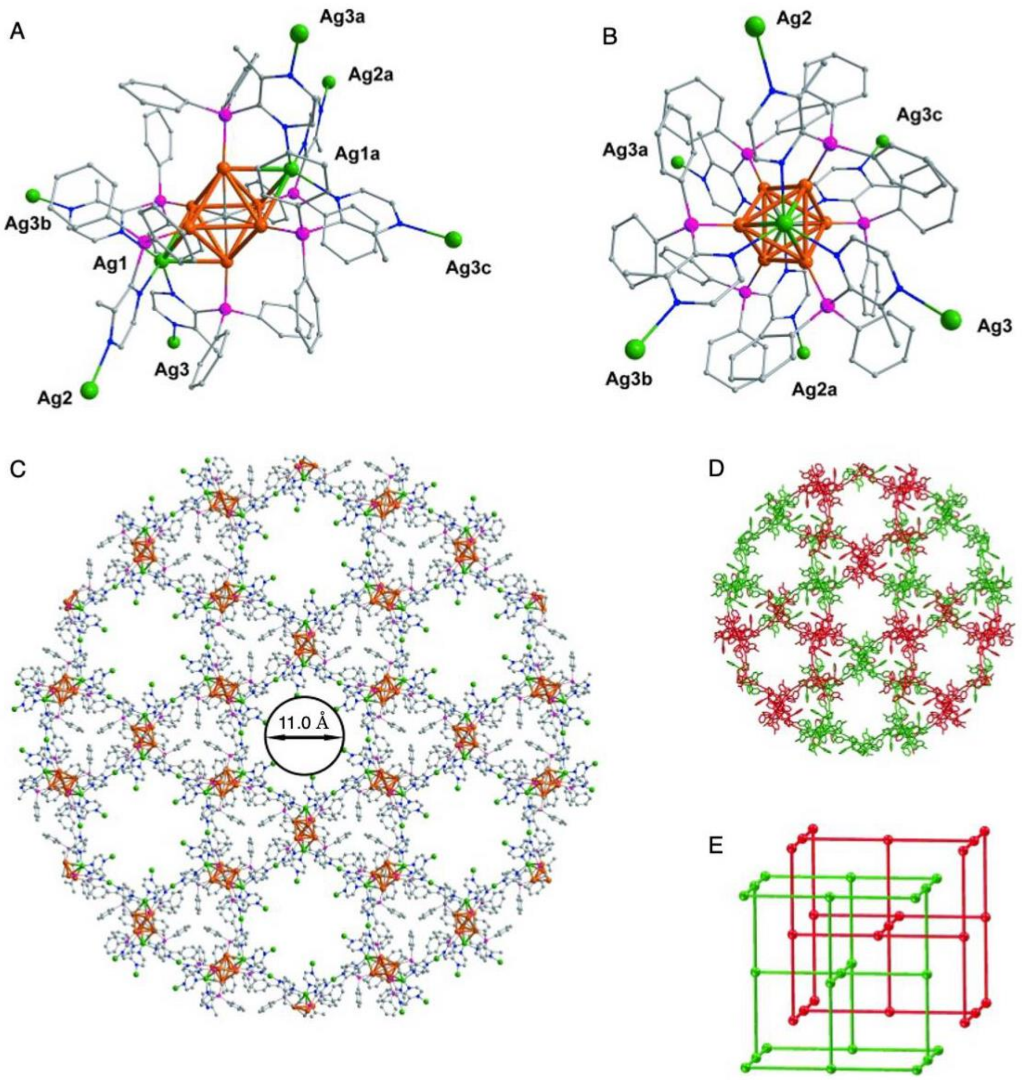

Figure 41. (**A**) Structure of [C(Au-mdppz)$_6$](BF$_4$)$_2$. (**B**) Four extensions: Ag3, Ag3a, Ag3b, and Ag3c. Note that Ag2 and Ag2a are not involved in the structural extension. (**C**) Perspective view of the 3D CS along the *c* direction. Au = orange, Ag = green, P = purple, N = blue, C = gray. (**D**) Two interpenetrating nets shown in different colors; anions and solvent molecules are omitted for clarity. (**E**) Schematic representation of NbO topology in the 3D CS. Reproduced with permission from Reference [179]. Copyright 2014 Wiley-VCH.

5. Summary

In this review, representative studies on the formation of 1D, 2D, and 3D CSs in which metal NCs were self-organized and regularly linked were summarized. From this summary, the following points became clear.

(1) **Methods.** The methods to connect metal NCs that have been reported to date can be roughly divided into the following five categories: (i) direct connection by formation of metal−metal bonds (Figure 2A); (ii) connection by Ag−O, Ag−S, or Ag−Cl bond formation (Figure 2B); (iii) connection by counterions (Figure 2C); (iv) connection by linker molecules (Figure 2D); and (v) connection by inter-ligand interactions (Figure 2E; not introduced in this review).

(2) **Diversity.** Among CSs produced by the above methods, there are many examples of the formation of 1D, 2D, and 3D CSs through the use of methods (ii) and (iv). An important point when constructing CSs by these methods is the design of the ligand of the NCs and linker,

respectively. It is presumed that the control of these species is relatively easy, which has led to the wider utilization of methods (ii) and (iv) than of the other methods. In particular, for method (iv), existing knowledge obtained in the study of normal MOFs can be considered.

(3) **Metal element.** To directly connect metal NCs, it is effective to use Au as a main element because it forms strong aurophilic interactions (intermetal interactions). In the connections involving metal−O or metal−Cl bonds, it is effective to use Ag as a main element because it readily bonds with O or Cl. Moreover, in the connections using bpy as a linker, Ag is attractive as the main element because of the high affinity of N and Ag.

(4) **Stability.** The formation of a CS generally improves the thermal stability of the component metal NCs regardless of the connection mode.

(5) **Electronic structure.** The formation of a CS often causes the band gap of the NC to narrow. This means that CS formation allows the use of a broader wavelength range of light, opening up the possibility of visible-light-driven photocatalysis by using CSs.

(6) **PL properties.** For 2D and 3D CS using linkers, CS formation often leads to an increase in PL emission intensity. When metal NCs are the PL source, there are many cases in which dual emission peaks appear upon connection with a linker. In addition, the PL color of a CS often changes depending on the kind of VOC trapped in its pores.

(7) **Electrical conduction.** The electron conductivity of CSs changes dramatically depending on the distance between each metal NC and the mode of connection; 1D CS formed by the direct connection via metal−metal bond shows the higher conductivity than 1D CS connected through counter ion.

(8) **Possible applications.** The reported CSs have potential applications in fields such as electronic devices, luminescent devices, gas and temperature sensing, and photocatalysis.

This review allowed us to obtain a common understanding of the CSs reported to date and their functions. We hope that the knowledge thus clarified will lead to clear design guidelines for developing new CSs with desired functions in the future.

6. Outlook

It is expected that the following studies will be conducted in the future, leading to new CSs.

(1) **Use of other metal elements.** At present, mostly Au and Ag are used as the metal element in CSs. This is largely related to the high stability of Au and Ag NCs. For Ag NCs, the good connectivity between Ag and linker molecules is also related to this fact. On the other hand, several syntheses of individual copper (Cu) NCs have been reported recently [10,180–183]. In addition, other metal ions are often used in normal MOFs with metal ions as nodes [153]. CS formation of NCs based on Cu or other metals may also lead to materials with high thermal stability. In the future, it is expected that many elements will be used in CSs, thereby realizing various functions and decreased cost of such materials.

(2) **Use of the alloying effect.** At present, there are few examples in which alloy NCs are connected to form CSs [142,143,146]. Mixing different elements leads to NCs with physical/chemical properties and functions that are different from those of monometal NCs. In fact, for individual metal NCs, many cases have been reported in which new physical properties/functions appeared because of mixing/synergistic effects [66,184–194]. The previous studies have established basic techniques for the formation of CSs consisting of Ag NCs. In the future, it is expected that more functional materials will be created by extending such CS formation techniques to Ag-based alloy NCs.

(3) **Connection of reported metal NCs.** Ag NC-based MOFs are interesting because they can be synthesized by a one-pot process. However, in CSs formed by such a method, metal NCs that are stable only in the CS are often found as nodes. For individual metal NCs, many NCs have already been synthesized with atomic precision [1–65]. In addition, much information has been

obtained on methods to generate novel functions in such NCs, including alloying [66–68]. In the future, it is expected that a method to more effectively utilize the reported metal NCs in CSs will be found. To achieve this, it may be necessary to establish new connection methods different from those described in this review (Figure 2).

(4) **Elucidation of electronic conductivity.** We believe that 1D CSs may be applied as nanodevices. However, at present, few experiments on the conductivity of 1D CSs have been reported [146,152]. In the future, it is expected that the conductivity of 1D CSs will be measured as a basic physical property. It is anticipated that the accumulation of such information will eventually lead to the production of nanodevices based on 1D CSs of metal NCs.

(5) **Exploration of other possible applications of connected structures.** Various applications, such as gas storage, gas separation, gas conversion, and reaction-selective catalysis, have been studied for normal MOFs with metal ions as nodes [117]. It has also been reported that, in the case of self-assembled complexes, a reaction different from that in the case of using an ordinary flask proceeds in the cage structure (i.e., the cage behaves as a nanoflask) [116]. In the future, it is expected that these possibilities will be investigated for metal NC-based MOFs and that their functions will be much higher than those of conventional MOFs and self-assembled complexes.

As mentioned in Section 1, the advance of bottom-up technology is essential for the further development of nanotechnology in the future. In previous research, multiple techniques to generate metal atoms on the molar scale in a solution and to self-organize them to form nanomaterials with the same number of constituent atoms and the same number of molecules have been studied; that is, precise synthesis techniques of metal NCs have been developed. However, to apply these metal NCs as devices and next-generation materials, developing techniques to assemble metal NCs to a size that is easy to handle is necessary (Figure 1). We hope that technologies that allow the self-organization of regularly arranged CSs composed of metal NCs will be further developed in the future. Ultimately, such nanotechnology is expected to enable resource conservation, energy conservation, decreased waste and environmental load, and the better use of time by human society.

Author Contributions: Y.N. constructed the structure of this review; T.K., S.O., and S.K. wrote Section 1, Section 5, and Section 6 and compiled figures and tables; A.E. wrote Sections 3 and 4; H.H. wrote Section 2; Y.N. and S.H. revised the entire draft before submission. All authors have read and agreed to the published version of the manuscript.

Funding: This work was supported by the Japan Society for the Promotion of Science (JSPS) KAKENHI (grant numbers JP16H04099, 16K21402, 20H02698, and 20H02552), Scientific Research on Innovative Areas "Coordination Asymmetry" (grant numbers 17H05385 and 19H04595), and Scientific Research on Innovative Areas "Innovations for Light-Energy Conversion" (grant numbers 18H05178 and 20H05115). Funding from the Asahi Glass Foundation, TEPCO Memorial Foundation Research Grant (Basic Research), and Kato Foundation for Promotion of Science (grant number KJ-2904) is also gratefully acknowledged.

Conflicts of Interest: There are no conflicts to declare.

References

1. Pradeep, T. *Nano: The Essentials*, 3rd ed.; Tata McGraw-Hill Education: New Delhi, India, 2008.
2. Jin, R.; Zeng, C.; Zhou, M.; Chen, Y. Atomically Precise Colloidal Metal Nanoclusters and Nanoparticles: Fundamentals and Opportunities. *Chem. Rev.* **2016**, *116*, 10346–10413. [CrossRef] [PubMed]
3. Nasaruddin, R.R.; Chen, T.; Yan, N.; Xie, J. Roles of Thiolate Ligands in the Synthesis, Properties and Catalytic Application of Gold Nanoclusters. *Coord. Chem. Rev.* **2018**, *368*, 60–79. [CrossRef]
4. Du, Y.; Sheng, H.; Astruc, D.; Zhu, M. Atomically Precise Noble Metal Nanoclusters as Efficient Catalysts: A Bridge between Structure and Properties. *Chem. Rev.* **2020**, *120*, 526–622. [CrossRef] [PubMed]
5. Sakthivel, N.A.; Dass, A. Aromatic Thiolate-Protected Series of Gold Nanomolecules and a Contrary Structural Trend in Size Evolution. *Acc. Chem. Res.* **2018**, *51*, 1774–1783. [CrossRef]
6. Kawasaki, H.; Kumar, S.; Li, G.; Zeng, C.; Kauffman, D.R.; Yoshimoto, J.; Iwasaki, Y.; Jin, R. Generation of Singlet Oxygen by Photoexcited $Au_{25}(SR)_{18}$ Clusters. *Chem. Mater.* **2014**, *26*, 2777–2788. [CrossRef]

7. Yamamoto, K.; Imaoka, T.; Tanabe, M.; Kambe, T. New Horizon of Nanoparticle and Cluster Catalysis with Dendrimers. *Chem. Rev.* **2020**, *120*, 1397–1437. [CrossRef]
8. Whetten, R.L.; Weissker, H.-C.; Pelayo, J.J.; Mullins, S.M.; López-Lozano, X.; Garzón, I.L. Chiral-Icosahedral (*I*) Symmetry in Ubiquitous Metallic Cluster Compounds (145A,60X): Structure and Bonding Principles. *Acc. Chem. Res.* **2019**, *52*, 34–43. [CrossRef] [PubMed]
9. Bakar, M.A.; Sugiuchi, M.; Iwasaki, M.; Shichibu, Y.; Konishi, K. Hydrogen Bonds to Au Atoms in Coordinated Gold Clusters. *Nat. Commun.* **2017**, *8*, 576. [CrossRef]
10. Sharma, S.; Chakrahari, K.K.; Saillard, J.-Y.; Liu, C.W. Structurally Precise Dichalcogenolate-Protected Copper and Silver Superatomic Nanoclusters and Their Alloys. *Acc. Chem. Res.* **2018**, *51*, 2475–2483. [CrossRef]
11. Brust, M.; Walker, M.; Bethell, D.; Schiffrin, D.J.; Whyman, R. Synthesis of Thiol-derivatised Gold Nanoparticles in a Two-Phase Liquid-Liquid System. *J. Chem. Soc. Chem. Commun.* **1994**, *801–802*. [CrossRef]
12. Whetten, R.L.; Khoury, J.T.; Alvarez, M.M.; Murthy, S.; Vezmar, I.; Wang, Z.L.; Stephens, P.W.; Cleveland, C.L.; Luedtke, W.D.; Landman, U. Nanocrystal Gold Molecules. *Adv. Mater.* **1996**, *8*, 428–433. [CrossRef]
13. Schaaff, T.G.; Shafigullin, M.N.; Khoury, J.T.; Vezmar, I.; Whetten, R.L.; Cullen, W.G.; First, P.N.; Gutiérrez-Wing, C.; Ascensio, J.; Jose-Yacamán, M.J. Isolation of Smaller Nanocrystal Au Molecules: Robust Quantum Effects in Optical Spectra. *J. Phys. Chem. B* **1997**, *101*, 7885–7891. [CrossRef]
14. Donkers, R.L.; Lee, D.; Murray, R.W. Synthesis and Isolation of the Molecule-Like Cluster $Au_{38}(PhCH_2CH_2S)_{24}$. *Langmuir* **2004**, *20*, 1945–1952. [CrossRef]
15. Ingram, R.S.; Hostetler, M.J.; Murray, R.W.; Schaaff, T.G.; Khoury, J.T.; Whetten, R.L.; Bigioni, T.P.; Guthrie, D.K.; First, P.N. 28 kDa Alkanethiolate-Protected Au Clusters Give Analogous Solution Electrochemistry and STM Coulomb Staircases. *J. Am. Chem. Soc.* **1997**, *119*, 9279–9280. [CrossRef]
16. Schaaff, T.G.; Shafigullin, M.N.; Khoury, J.T.; Vezmar, I.; Whetten, R.L. Properties of a Ubiquitous 29 kDa Au:SR Cluster Compound. *J. Phys. Chem. B* **2001**, *105*, 8785–8796. [CrossRef]
17. Murthy, S.; Bigioni, T.P.; Wang, Z.L.; Khoury, J.T.; Whetten, R.L. Liquid-Phase Synthesis of Thiol-Derivatized Silver Nanocrystals. *Mater. Lett.* **1997**, *30*, 321–325. [CrossRef]
18. Link, S.; Beeby, A.; FitzGerald, S.; El-Sayed, M.A.; Schaaff, T.G.; Whetten, R.L. Visible to Infrared Luminescence from a 28-Atom Gold Cluster. *J. Phys. Chem. B* **2002**, *106*, 3410–3415. [CrossRef]
19. Hostetler, M.J.; Wingate, J.E.; Zhong, C.-J.; Harris, J.E.; Vachet, R.W.; Clark, M.R.; Londono, J.D.; Green, S.J.; Stokes, J.J.; Wignall, G.D.; et al. Alkanethiolate Gold Cluster Molecules with Core Diameters from 1.5 to 5.2 nm: Core and Monolayer Properties as a Function of Core Size. *Langmuir* **1998**, *14*, 17–30. [CrossRef]
20. Hostetler, M.J.; Stokes, J.J.; Murray, R.W. Infrared Spectroscopy of Three-Dimensional Self-Assembled Monolayers: *N*-Alkanethiolate Monolayers on Gold Cluster Compounds. *Langmuir* **1996**, *12*, 3604–3612. [CrossRef]
21. Terrill, R.H.; Postlethwaite, T.A.; Chen, C.-H.; Poon, C.-D.; Terzis, A.; Chen, A.; Hutchison, J.E.; Clark, M.R.; Wignall, G.; Londono, J.D.; et al. Monolayers in Three Dimensions: NMR, SAXS, Thermal, and Electron Hopping Studies of Alkanethiol Stabilized Gold Clusters. *J. Am. Chem. Soc.* **1995**, *117*, 12537–12548. [CrossRef]
22. Schaaff, T.G.; Knight, G.; Shafigullin, M.N.; Borkman, R.F.; Whetten, R.L. Isolation and Selected Properties of a 10.4 kDa Gold: Glutathione Cluster Compound. *J. Phys. Chem. B* **1998**, *102*, 10643–10646. [CrossRef]
23. Schaaff, T.G.; Whetten, R.L. Giant Gold–Glutathione Cluster Compounds: Intense Optical Activity in Metal-Based Transitions. *J. Phys. Chem. B* **2000**, *104*, 2630–2641. [CrossRef]
24. Alvarez, M.M.; Chen, J.; Plascencia-Villa, G.; Black, D.M.; Griffith, W.P.; Garzón, I.L.; José-Yacamán, M.; Demeler, B.; Whetten, R.L. Hidden Components in Aqueous "Gold-144" Fractionated by PAGE: High-Resolution Orbitrap ESI-MS Identifies the Gold-102 and Higher All-Aromatic Au-*p*MBA Cluster Compounds. *J. Phys. Chem. B* **2016**, *120*, 6430–6438. [CrossRef]
25. Plascencia-Villa, G.; Demeler, B.; Whetten, R.L.; Griffith, W.P.; Alvarez, M.; Black, D.M.; José-Yacamán, M. Analytical Characterization of Size-Dependent Properties of Larger Aqueous Gold Nanoclusters. *J. Phys. Chem. C* **2016**, *120*, 8950–8958. [CrossRef]
26. Bootharaju, M.S.; Burlakov, V.M.; Besong, T.M.D.; Joshi, C.P.; AbdulHalim, L.G.; Black, D.M.; Whetten, R.L.; Goriely, A.; Bakr, O.M. Reversible Size Control of Silver Nanoclusters via Ligand-Exchange. *Chem. Mater.* **2015**, *27*, 4289–4297. [CrossRef]
27. Heaven, M.W.; Dass, A.; White, P.S.; Holt, K.M.; Murray, R.W. Crystal Structure of the Gold Nanoparticle $[N(C_8H_{17})_4]$ $[Au_{25}(SCH_2CH_2Ph)_{18}]$. *J. Am. Chem. Soc.* **2008**, *130*, 3754–3755. [CrossRef] [PubMed]

28. Negishi, Y.; Sakamoto, C.; Ohyama, T.; Tsukuda, T. Synthesis and the Origin of the Stability of Thiolate-Protected Au_{130} and Au_{187} Clusters. *J. Phys. Chem. Lett.* **2012**, *3*, 1624–1628. [CrossRef]
29. Negishi, Y.; Nakazaki, T.; Malola, S.; Takano, S.; Niihori, Y.; Kurashige, W.; Yamazoe, S.; Tsukuda, T.; Häkkinen, H. A Critical Size for Emergence of Nonbulk Electronic and Geometric Structures in Dodecanethiolate-Protected Au Clusters. *J. Am. Chem. Soc.* **2015**, *137*, 1206–1212. [CrossRef]
30. Negishi, Y.; Kurashige, W.; Niihori, Y.; Iwasa, T.; Nobusada, K. Isolation, Structure, and Stability of a Dodecanethiolate-Protected Pd_1Au_{24} Cluster. *Phys. Chem. Chem. Phys.* **2010**, *12*, 6219–6225. [CrossRef]
31. Negishi, Y.; Iwai, T.; Ide, M. Continuous Modulation of Electronic Structure of Stable Thiolate-Protected Au_{25} Cluster by Ag Doping. *Chem. Commun.* **2010**, *46*, 4713–4715. [CrossRef]
32. Negishi, Y.; Kurashige, W.; Kobayashi, Y.; Yamazoe, S.; Kojima, N.; Seto, M.; Tsukuda, T. Formation of a Pd@Au_{12} Superatomic Core in $Au_{24}Pd_1(SC_{12}H_{25})_{18}$ Probed by ^{197}Au Mössbauer and Pd K-Edge EXAFS Spectroscopy. *J. Phys. Chem. Lett.* **2013**, *4*, 3579–3583. [CrossRef]
33. Negishi, Y.; Munakata, K.; Ohgake, W.; Nobusada, K. Effect of Copper Doping on Electronic Structure, Geometric Structure, and Stability of Thiolate-Protected Au_{25} Nanoclusters. *J. Phys. Chem. Lett.* **2012**, *3*, 2209–2214. [CrossRef] [PubMed]
34. Niihori, Y.; Matsuzaki, M.; Pradeep, T.; Negishi, Y. Separation of Precise Compositions of Noble Metal Clusters Protected with Mixed Ligands. *J. Am. Chem. Soc.* **2013**, *135*, 4946–4949. [CrossRef] [PubMed]
35. Niihori, Y.; Matsuzaki, M.; Uchida, C.; Negishi, Y. Advanced Use of High-Performance Liquid Chromatography for Synthesis of Controlled Metal Clusters. *Nanoscale* **2014**, *6*, 7889–7896. [CrossRef]
36. Niihori, Y.; Kikuchi, Y.; Kato, A.; Matsuzaki, M.; Negishi, Y. Understanding Ligand Exchange Reactions on Thiolate-Protected Gold Clusters by Probing Isomer Distributions Using Reversed-Phase High-Performance Liquid Chromatography. *ACS Nano* **2015**, *9*, 9347–9356. [CrossRef]
37. Niihori, Y.; Eguro, M.; Kato, A.; Sharma, S.; Kumar, B.; Kurashige, W.; Nobusada, K.; Negishi, Y. Improvements in the Ligand-Exchange Reactivity of Phenylethanethiolate-Protected Au_{25} Nanocluster by Ag or Cu Incorporation. *J. Phys. Chem. C* **2016**, *120*, 14301–14309. [CrossRef]
38. Niihori, Y.; Koyama, Y.; Watanabe, S.; Hashimoto, S.; Hossain, S.; Nair, L.V.; Kumar, B.; Kurashige, W.; Negishi, Y. Atomic and Isomeric Separation of Thiolate-Protected Alloy Clusters. *J. Phys. Chem. Lett.* **2018**, *9*, 4930–4934. [CrossRef] [PubMed]
39. Niihori, Y.; Hashimoto, S.; Koyama, Y.; Hossain, S.; Kurashige, W.; Negishi, Y. Dynamic Behavior of Thiolate-Protected Gold–Silver 38-Atom Alloy Clusters in Solution. *J. Phys. Chem. C* **2019**, *123*, 13324–13329. [CrossRef]
40. Niihori, Y.; Kikuchi, Y.; Shima, D.; Uchida, C.; Sharma, S.; Hossain, S.; Kurashige, W.; Negishi, Y. Separation of Glutathionate-Protected Gold Clusters by Reversed-Phase Ion-Pair High-Performance Liquid Chromatography. *Ind. Eng. Chem. Res.* **2017**, *56*, 1029–1035. [CrossRef]
41. Niihori, Y.; Shima, D.; Yoshida, K.; Hamada, K.; Nair, L.V.; Hossain, S.; Kurashige, W.; Negishi, Y. High-Performance Liquid Chromatography Mass Spectrometry of Gold and Alloy Clusters Protected by Hydrophilic Thiolates. *Nanoscale* **2018**, *10*, 1641–1649. [CrossRef]
42. Murayama, H.; Narushima, T.; Negishi, Y.; Tsukuda, T. Structures and Stabilities of Alkanethiolate Monolayers on Palladium Clusters As Studied by Gel Permeation Chromatography. *J. Phys. Chem. B* **2004**, *108*, 3496–3503. [CrossRef]
43. Tsunoyama, H.; Negishi, Y.; Tsukuda, T. Chromatographic Isolation of "Missing" Au_{55} Clusters Protected by Alkanethiolates. *J. Am. Chem. Soc.* **2006**, *128*, 6036–6037. [CrossRef] [PubMed]
44. Negishi, Y.; Arai, R.; Niihori, Y.; Tsukuda, T. Isolation and Structural Characterization of Magic Silver Clusters Protected by 4-(*tert*-butyl) benzyl mercaptan. *Chem. Commun.* **2011**, *47*, 5693–5695. [CrossRef] [PubMed]
45. Kurashige, W.; Yamazoe, S.; Yamaguchi, M.; Nishido, K.; Nobusada, K.; Tsukuda, T.; Negishi, Y. Au_{25} Clusters Containing Unoxidized Tellurolates in the Ligand Shell. *J. Phys. Chem. Lett.* **2014**, *5*, 2072–2076. [CrossRef]
46. Negishi, Y.; Takasugi, Y.; Sato, S.; Yao, H.; Kimura, K.; Tsukuda, T. Structures, Stabilities and Physicochemical Properties of Organometallic Hybrid Clusters. *J. Am. Chem. Soc.* **2004**, *126*, 6518–6519. [CrossRef]
47. Shichibu, Y.; Negishi, Y.; Tsunoyama, H.; Kanehara, M.; Teranishi, T.; Tsukuda, T. Extremely High Stability of Glutathionate-Protected Au_{25} Clusters Against Core Etching. *Small* **2007**, *3*, 835–839. [CrossRef]
48. Shichibu, Y.; Negishi, Y.; Tsukuda, T.; Teranishi, T. Large-Scale Synthesis of Thiolated Au_{25} Clusters via Ligand Exchange Reactions of Phosphine-Stabilized Au_{11} Clusters. *J. Am. Chem. Soc.* **2005**, *127*, 13464–13465. [CrossRef]

49. Ikeda, K.; Kobayashi, Y.; Negishi, Y.; Seto, M.; Iwasa, T.; Nobusada, K.; Tsukuda, T.; Kojima, N. Thiolate-Induced Structural Reconstruction of Gold Clusters Probed by ^{197}Au Mössbauer Spectroscopy. *J. Am. Chem. Soc.* **2007**, *129*, 7230–7231. [CrossRef]
50. Negishi, Y.; Takasugi, Y.; Sato, S.; Yao, H.; Kimura, K.; Tsukuda, T. Kinetic Stabilization of Growing Gold Clusters by Passivation with Thiolates. *J. Phys. Chem. B* **2006**, *110*, 12218–12221. [CrossRef]
51. Omoda, T.; Takano, S.; Yamazoe, S.; Koyasu, K.; Negishi, Y.; Tsukuda, T. An $Au_{25}(SR)_{18}$ Cluster with a Face-Centered Cubic Core. *J. Phys. Chem. C* **2018**, *122*, 13199–13204. [CrossRef]
52. Jadzinsky, P.D.; Calero, G.; Ackerson, C.J.; Bushnell, D.A.; Kornberg, R.D. Structure of a Thiol Monolayer-Protected Gold Nanoparticle at 1.1 Å Resolution. *Science* **2007**, *318*, 430–433. [CrossRef] [PubMed]
53. Zhu, M.; Aikens, C.M.; Hollander, F.J.; Schatz, G.C.; Jin, R. Correlating the Crystal Structure of a Thiol-Protected Au_{25} Cluster and Optical Properties. *J. Am. Chem. Soc.* **2008**, *130*, 5883–5885. [CrossRef]
54. Qian, H.; Eckenhoff, W.T.; Zhu, Y.; Pintauer, T.; Jin, R. Total Structure Determination of Thiolate-Protected Au_{38} Nanoparticles. *J. Am. Chem. Soc.* **2010**, *132*, 8280–8281. [CrossRef] [PubMed]
55. Chen, Y.; Zeng, C.; Liu, C.; Kirschbaum, K.; Gayathri, C.; Gil, R.R.; Rosi, N.L.; Jin, R. Crystal Structure of Barrel-Shaped Chiral $Au_{130}(p\text{-MBT})_{50}$ Nanocluster. *J. Am. Chem. Soc.* **2015**, *137*, 10076–10079. [CrossRef]
56. Desireddy, A.; Conn, B.E.; Guo, J.; Yoon, B.; Barnett, R.N.; Monahan, B.M.; Kirschbaum, K.; Griffith, W.P.; Whetten, R.L.; Landman, U.; et al. Ultrastable Silver Nanoparticles. *Nature* **2013**, *501*, 399–402. [CrossRef] [PubMed]
57. Yang, H.; Wang, Y.; Huang, H.; Gell, L.; Lehtovaara, L.; Malola, S.; Häkkinen, H.; Zheng, N. All-Thiol-Stabilized Ag_{44} and $Au_{12}Ag_{32}$ Nanoparticles with Single-Crystal Structures. *Nat. Commun.* **2013**, *4*, 2422. [CrossRef]
58. Joshi, C.P.; Bootharaju, M.S.; Alhilaly, M.J.; Bakr, O.M. $[Ag_{25}(SR)_{18}]^{-}$: The "Golden" Silver Nanoparticle. *J. Am. Chem. Soc.* **2015**, *137*, 11578–11581. [CrossRef]
59. Lei, Z.; Wan, X.-K.; Yuan, S.-F.; Guan, Z.-J.; Wang, Q.-M. Alkynyl Approach toward the Protection of Metal Nanoclusters. *Acc. Chem. Res.* **2018**, *51*, 2465–2474. [CrossRef]
60. Kwak, K.; Lee, D. Electrochemistry of Atomically Precise Metal Nanoclusters. *Acc. Chem. Res.* **2019**, *52*, 12–22. [CrossRef]
61. Kurashige, W.; Hayashi, R.; Wakamatsu, K.; Kataoka, Y.; Hossain, S.; Iwase, A.; Kudo, A.; Yamazoe, S.; Negishi, Y. Atomic-Level Understanding of the Effect of Heteroatom Doping of the Cocatalyst on Water-Splitting Activity in AuPd or AuPt Alloy Cluster-Loaded $BaLa_4Ti_4O_{15}$. *ACS Appl. Energy Mater.* **2019**, *2*, 4175–4187. [CrossRef]
62. Wang, S.; Meng, X.; Das, A.; Li, T.; Song, Y.; Cao, T.; Zhu, X.; Zhu, M.; Jin, R. A 200-Fold Quantum Yield Boost in the Photoluminescence of Silver-Doped Ag_xAu_{25-x} Nanoclusters: The 13 th Silver Atom Matters. *Angew. Chem. Int. Ed.* **2014**, *53*, 2376–2380. [CrossRef]
63. Li, Z.; Yang, X.; Liu, C.; Wang, J.; Li, G. Effects of Doping in 25-Atom Bimetallic Nanocluster Catalysts for Carbon–Carbon Coupling Reaction of Iodoanisole and Phenylacetylene. *Prog. Nat. Sci. Mater. Int.* **2016**, *26*, 477–482. [CrossRef]
64. Liu, Y.; Chai, X.; Cai, X.; Chen, M.; Jin, R.; Ding, W.; Zhu, Y. Central Doping of a Foreign Atom into the Silver Cluster for Catalytic Conversion of CO_2 toward C–C Bond Formation. *Angew. Chem. Int. Ed.* **2018**, *57*, 9775–9779. [CrossRef]
65. Tsukuda, T. Toward an Atomic-Level Understanding of Size-Specific Properties of Protected and Stabilized Gold Clusters. *Bull. Chem. Soc. Jpn.* **2012**, *85*, 151–168. [CrossRef]
66. Hossain, S.; Niihori, Y.; Nair, L.V.; Kumar, B.; Kurashige, W.; Negishi, Y. Alloy Clusters: Precise Synthesis and Mixing Effects. *Acc. Chem. Res.* **2018**, *51*, 3114–3124. [CrossRef]
67. Takano, S.; Hasegawa, S.; Suyama, M.; Tsukuda, T. Hydride Doping of Chemically Modified Gold-Based Superatoms. *Acc. Chem. Res.* **2018**, *51*, 3074–3083. [CrossRef]
68. Yan, J.; Teo, B.K.; Zheng, N. Surface Chemistry of Atomically Precise Coinage—Metal Nanoclusters: From Structural Control to Surface Reactivity and Catalysis. *Acc. Chem. Res.* **2018**, *51*, 3084–3093. [CrossRef]
69. Gan, Z.; Xia, N.; Wu, Z. Discovery, Mechanism, and Application of Antigalvanic Reaction. *Acc. Chem. Res.* **2018**, *51*, 2774–2783. [CrossRef]
70. Niihori, Y.; Kurashige, W.; Matsuzaki, M.; Negishi, Y. Remarkable Enhancement in Ligand-Exchange Reactivity of Thiolate-Protected Au_{25} Nanoclusters by Single Pd Atom Doping. *Nanoscale* **2013**, *5*, 508–512. [CrossRef]

71. Xie, S.; Tsunoyama, H.; Kurashige, W.; Negishi, Y.; Tsukuda, T. Enhancement in Aerobic Alcohol Oxidation Catalysis of Au$_{25}$ Clusters by Single Pd Atom Doping. *ACS Catal.* **2012**, *2*, 1519–1523. [CrossRef]
72. Negishi, Y.; Igarashi, K.; Munakata, K.; Ohgake, W.; Nobusada, K. Palladium Doping of Magic Gold Cluster Au$_{38}$(SC$_2$H$_4$Ph)$_{24}$: Formation of Pd$_2$Au$_{36}$(SC$_2$H$_4$Ph)$_{24}$ with Higher Stability than Au$_{38}$(SC$_2$H$_4$Ph)$_{24}$. *Chem. Commun.* **2012**, *48*, 660–662. [CrossRef]
73. Yamazoe, S.; Kurashige, W.; Nobusada, K.; Negishi, Y.; Tsukuda, T. Preferential Location of Coinage Metal Dopants (M = Ag or Cu) in [Au$_{25-x}$M$_x$(SC$_2$H$_4$Ph)$_{18}$]$^-$ (x~1) As Determined by Extended X-ray Absorption Fine Structure and Density Functional Theory Calculations. *J. Phys. Chem. C* **2014**, *118*, 25284–25290. [CrossRef]
74. Hossain, S.; Ono, T.; Yoshioka, M.; Hu, G.; Hosoi, M.; Chen, Z.; Nair, L.V.; Niihori, Y.; Kurashige, W.; Jiang, D.-E.; et al. Thiolate-Protected Trimetallic Au$_{\sim20}$Ag$_{\sim4}$Pd and Au$_{\sim20}$Ag$_{\sim4}$Pt Alloy Clusters with Controlled Chemical Composition and Metal Positions. *J. Phys. Chem. Lett.* **2018**, *9*, 2590–2594. [CrossRef]
75. Sharma, S.; Kurashige, W.; Nobusada, K.; Negishi, Y. Effect of Trimetallization in Thiolate-Protected Au$_{24-n}$Cu$_n$Pd Clusters. *Nanoscale* **2015**, *7*, 10606–10612. [CrossRef]
76. Sharma, S.; Yamazoe, S.; Ono, T.; Kurashige, W.; Niihori, Y.; Nobusada, K.; Tsukuda, T.; Negishi, Y. Tuning the Electronic Structure of Thiolate-Protected 25-Atom Clusters by Co-Substitution with Metals Having Different Preferential Sites. *Dalton Trans.* **2016**, *45*, 18064–18068. [CrossRef]
77. Nair, L.V.; Hossain, S.; Takagi, S.; Imai, Y.; Hu, G.; Wakayama, S.; Kumar, B.; Kurashige, W.; Jiang, D.-E.; Negishi, Y. Hetero-Biicosahedral [Au$_{24}$Pd(PPh$_3$)$_{10}$(SC$_2$H$_4$Ph)$_5$Cl$_2$]$^+$ Nanocluster: Selective Synthesis and Optical and Electrochemical Properties. *Nanoscale* **2018**, *10*, 18969–18979. [CrossRef] [PubMed]
78. Kurashige, W.; Yamaguchi, M.; Nobusada, K.; Negishi, Y. Ligand-Induced Stability of Gold Nanoclusters: Thiolate Versus Selenolate. *J. Phys. Chem. Lett.* **2012**, *3*, 2649–2652. [CrossRef]
79. Kurashige, W.; Munakata, K.; Nobusada, K.; Negishi, Y. Synthesis of Stable Cu$_n$Au$_{25-n}$ Nanoclusters (n = 1–9) Using Selenolate Ligands. *Chem. Commun.* **2013**, *49*, 5447–5449. [CrossRef]
80. Hossain, S.; Imai, Y.; Negishi, Y. Precise Synthesis of Platinum and Alloy Clusters and Elucidation of Their Structures. *AIP Conf. Proc.* **2019**, *2186*, 030018.
81. Kawawaki, T.; Negishi, Y.; Kawasaki, H. Photo/Electrocatalysis and Photosensitization Using Metal Nanoclusters for Green Energy and Medical Applications. *Nanoscale Adv.* **2020**, *2*, 17–36. [CrossRef]
82. Hossain, S.; Imai, Y.; Suzuki, D.; Choi, W.; Chen, Z.; Suzuki, T.; Yoshioka, M.; Kawawaki, T.; Lee, D.; Negishi, Y. Elucidating Ligand Effects in Thiolate-Protected Metal Clusters Using Au$_{24}$Pt(TBBT)$_{18}$ as a Model Cluster. *Nanoscale* **2019**, *11*, 22089–22098. [CrossRef]
83. Ito, S.; Takano, S.; Tsukuda, T. Alkynyl-Protected Au$_{22}$(C≡CR)$_{18}$ Clusters Featuring New Interfacial Motifs and R-Dependent Photoluminescence. *J. Phys. Chem. Lett.* **2019**, *10*, 6892–6896. [CrossRef]
84. Briant, C.E.; Theobald, B.R.C.; White, J.W.; Bell, L.K.; Mingos, D.M.P.; Welch, A.J. Synthesis and *X*-ray Structural Characterization of the Centred Icosahedral Gold Cluster Compound [Au$_{13}$(PMe$_2$Ph)$_{10}$Cl$_2$](PF$_6$)$_3$; the Realization of a Theoretical Prediction. *J. Chem. Soc. Chem. Commun.* **1981**, *201–202*. [CrossRef]
85. Schmid, G.; Pfeil, R.; Boese, R.; Bandermann, F.; Meyer, S.; Calis, G.H.M.; Van der Velden, J.W.A. Au$_{55}$[P(C$_6$H$_5$)$_3$]$_{12}$CI$_6$-Ein Goldcluster Ungewöhnlicher Größe. *Chem. Ber.* **1981**, *114*, 3634–3642. [CrossRef]
86. Kurasov, S.S.; Eremenko, N.K.; Slovokhotov, Y.L.; Struchkov, Y.T. High-Nuclearity Icosahedral Carbonylphosphineplatinum Clusters: Synthesis and Crystal Structure of Pt$_{17}$(μ_2-CO)$_4$(CO)$_8$(PEt$_3$)$_8$. *J. Organomet. Chem.* **1989**, *361*, 405–408. [CrossRef]
87. McPartlin, M.; Mason, R.; Malatesta, L. Novel Cluster Complexes of Gold(0)-Gold(I). *J. Chem. Soc. D* **1969**, *7*, 334. [CrossRef]
88. Mednikov, E.G.; Dahl, L.F. Syntheses, Structures and Properties of Primarily Nanosized Homo/Heterometallic Palladium CO/PR$_3$-Ligated Clusters. *Philos. Trans. R. Soc. A* **2010**, *368*, 1301–1332. [CrossRef]
89. Schmid, G. Large Clusters and Colloids. Metals in the Embryonic State. *Chem. Rev.* **1992**, *92*, 1709–1727. [CrossRef]
90. Schulz-Dobrick, M.; Jansen, M. Characterization of Gold Clusters by Crystallization with Polyoxometalates: The Intercluster Compounds [Au$_9$(dpph)$_4$] [Mo$_8$O$_{26}$], [Au$_9$(dpph)$_4$] [PW$_{12}$O$_{40}$] and [Au$_{11}$(PPh$_3$)$_8$Cl$_2$]$_2$[W$_6$O$_{19}$]. *Z. Anorg. Allg. Chem.* **2007**, *633*, 2326–2331. [CrossRef]
91. Teo, B.K.; Shi, X.; Zhang, H. Pure Gold Cluster of 1:9:9:1:9:9:1 Layered Structure: A Novel 39-Metal-Atom Cluster [(Ph$_3$P)$_{14}$Au$_{39}$Cl$_6$]Cl$_2$ with an Interstitial Gold Atom in a Hexagonal Antiprismatic Cage. *J. Am. Chem. Soc.* **1992**, *114*, 2743–2745. [CrossRef]

92. Vollenbroek, F.A.; Bour, J.J.; van der Veden, J.W.A. *Gold-Phosphine Cluster Compounds*: The Reactions of $[Au_9L_8]^{3+}$ (L = PPh_3) with L, SCN^- and Cl^- to $[Au_8L_8]^{2+}$ $(Au_{11}L_8(SCN)_2]^+$ and $[Au_{11}L_8Cl_2]^+$. *Recueil des Travaux Chimiques des Pays-Bas* **1980**, *99*, 137–141. [CrossRef]
93. Chini, P. Large Metal Carbonyl Clusters (LMCC). *J. Organomet. Chem.* **1980**, *200*, 37–61. [CrossRef]
94. Roth, J.D.; Lewis, G.J.; Safford, L.K.; Jiang, X.; Dahl, L.F.; Weaver, M.J. Exploration of the Ionizable Metal Cluster-Electrode Surface Analogy: Infrared Spectroelectrochemistry of $[Pt_{24}(CO)_{30}]^n$, $[Pt_{26}(CO)_{32}]^n$, and $[Pt_{38}(CO)_{44}]^n$ (n = 0 to −10) and Comparisons with Potential-Dependent Spectra of CO Adlayers on Platinum Surfaces. *J. Am. Chem. Soc.* **1992**, *114*, 6159–6169. [CrossRef]
95. Ceriotti, A.; Masciocchi, N.; Macchi, P.; Longoni, G. $[Pt_{19}(CO)_{21}(NO)]^{3-}$ and $[Pt_{38}(CO)_{44}]^{2-}$: Nitrosyl Bending through Intramolecular Electron Transfer as an Intermediate Step in the Nucleation Process from Polydecker to *ccp* Platinum Carbonyl Clusters. *Angew. Chem. Int. Ed.* **1999**, *38*, 3724–3727. [CrossRef]
96. Ciabatti, I.; Femoni, C.; Iapalucci, M.C.; Longoni, G.; Zacchini, S. Platinum Carbonyl Clusters Chemistry: Four Decades of Challenging Nanoscience. *J. Clust. Sci.* **2014**, *25*, 115–146. [CrossRef]
97. Negishi, Y.; Shimizu, N.; Funai, K.; Kanako, R.; Wakamatsu, K.; Harasawa, A.; Hossain, S.; Schuster, M.E.; Ozkaya, D.; Kurashige, W.; et al. γ-Alumina-Supported Pt_{17} Cluster: Controlled Loading, Geometrical Structure, and Size-Specific Catalytic Activity for Carbon Monoxide and Propylene Oxidation. *Nanoscale Adv.* **2020**, *2*, 669–678. [CrossRef]
98. Hao, L.; Spivak, G.J.; Xiao, J.; Vittal, J.J.; Puddephatt, R.J. First Octahedral Platinum Cluster: Structure as a Function of Electron Count in Pt_6 Clusters. *J. Am. Chem. Soc.* **1995**, *117*, 7011–7012. [CrossRef]
99. Cattabriga, E.; Ciabatti, I.; Femoni, C.; Funaioli, T.; Iapalucci, M.C.; Zacchini, S. Syntheses, Structures, and Electrochemistry of the Defective *ccp* $[Pt_{33}(CO)_{38}]^{2-}$ and the *bcc* $[Pt_{40}(CO)_{40}]^{6-}$ Molecular Nanoclusters. *Inorg. Chem.* **2016**, *55*, 6068–6079. [CrossRef]
100. Cesari, C.; Ciabatti, I.; Femoni, C.; Iapalucci, M.C.; Mancini, F.; Zacchini, S. Heteroleptic Chini-Type Platinum Clusters: Synthesis and Characterization of Bis-Phospine Derivatives of $[Pt_{3n}(CO)_{6n}]^{2-}$ (n = 2–4). *Inorg. Chem.* **2017**, *56*, 1655–1668. [CrossRef]
101. Kawawaki, T.; Negishi, Y. Gold Nanoclusters as Electrocatalysts for Energy Conversion. *Nanomaterials* **2020**, *10*, 238. [CrossRef]
102. Xie, J.; Zheng, Y.; Ying, J.Y. Highly selective and ultrasensitive detection of Hg^{2+} based on fluorescence quenching of Au nanoclusters by Hg^{2+}–Au^+ interactions. *Chem. Commun.* **2010**, *46*, 961–963. [CrossRef]
103. Li, G.; Jin, R. Atomically Precise Gold Nanoclusters as New Model Catalysts. *Acc. Chem. Res.* **2013**, *46*, 1749–1758. [CrossRef]
104. Kurashige, W.; Kumazawa, R.; Ishii, D.; Hayashi, R.; Niihori, Y.; Hossain, S.; Nair, L.V.; Takayama, T.; Iwase, A.; Yamazoe, S.; et al. Au_{25}-Loaded $BaLa_4Ti_4O_{15}$ Water-Splitting Photocatalyst with Enhanced Activity and Durability Produced Using New Chromium Oxide Shell Formation Method. *J. Phys. Chem. C* **2018**, *122*, 13669–13681. [CrossRef]
105. Negishi, Y.; Matsuura, Y.; Tomizawa, R.; Kurashige, W.; Niihori, Y.; Takayama, T.; Iwase, A.; Kudo, A. Controlled Loading of Small Au_n Clusters (n = 10–39) onto $BaLa_4Ti_4O_{15}$ Photocatalysts: Toward an Understanding of Size Effect of Cocatalyst on Water-Splitting Photocatalytic Activity. *J. Phys. Chem. C* **2015**, *119*, 11224–11232. [CrossRef]
106. Kurashige, W.; Mori, Y.; Ozaki, S.; Kawachi, M.; Hossain, S.; Kawawaki, T.; Shearer, C.J.; Iwase, A.; Metha, G.F.; Yamazoe, S.; et al. Activation of Water-Splitting Photocatalysts by Loading with Ultrafine Rh–Cr Mixed-Oxide Cocatalyst Nanoparticles. *Angew. Chem. Int. Ed.* **2020**, *59*, 7076–7082. [CrossRef]
107. Chen, Y.-S.; Choi, H.; Kamat, P.V. Metal-Cluster-Sensitized Solar Cells. A New Class of Thiolated Gold Sensitizers Delivering Efficiency Greater Than 2%. *J. Am. Chem. Soc.* **2013**, *135*, 8822–8825. [CrossRef]
108. Sakai, N.; Tatsuma, T. Photovoltaic Properties of Glutathione-Protected Gold Clusters Adsorbed on TiO_2 Electrodes. *Adv. Mater.* **2010**, *22*, 3185–3188. [CrossRef]
109. Teranishi, T.; Sugawara, A.; Shimizu, T.; Miyake, M. Planar Array of 1D Gold Nanoparticles on Ridge-and-Valley Structured Carbon. *J. Am. Chem. Soc.* **2002**, *124*, 4210–4211. [CrossRef]
110. Yonezawa, T.; Onoue, S.-Y.; Kimizuka, N. Metal Coating of DNA Molecules by Cationic, Metastable Gold Nanoparticles. *Chem. Lett.* **2002**, *31*, 1172–1173. [CrossRef]
111. Negishi, Y.; Tsunoyama, H.; Yanagimoto, Y.; Tsukuda, T. Subnanometer-sized Gold Clusters with Dual Molecular Receptors: Synthesis and Assembly in One-dimensional Arrangements. *Chem. Lett.* **2005**, *34*, 1638–1639. [CrossRef]

112. Yokoyama, T.; Hirata, N.; Tsunoyama, H.; Negishi, Y.; Nakajima, A. Characterization of Floating-Gate Memory Device with Thiolate-Protected Gold and Gold-Palladium Nanoclusters. *AIP Adv.* **2018**, *8*, 065002. [CrossRef]
113. Zhang, H.; Yasutake, Y.; Shichibu, Y.; Teranishi, T.; Majima, Y. Tunneling Resistance of Double-Barrier Tunneling Structures with an Alkanethiol-Protected Au Nanoparticle. *Phys. Rev. B* **2005**, *72*, 205441. [CrossRef]
114. Yoon, B.; Luedtke, W.D.; Barnett, R.N.; Gao, J.; Desireddy, A.; Conn, B.E.; Bigioni, T.; Landman, U. Hydrogen-Bonded Structure and Mechanical Chiral Response of a Silver Nanoparticle Superlattice. *Nat. Mater.* **2014**, *13*, 807–811. [CrossRef]
115. Zeng, C.; Chen, Y.; Kirschbaum, K.; Lambright, K.J.; Jin, R. Emergence of Hierarchical Structural Complexities in Nanoparticles and Their Assembly. *Science* **2016**, *354*, 1580–1584. [CrossRef]
116. Yoshizawa, M.; Tamura, M.; Fujita, M. Diels-Alder in Aqueous Molecular Hosts: Unusual Regioselectivity and Efficient Catalysis. *Science* **2006**, *312*, 251–254. [CrossRef]
117. Kitao, T.; Zhang, Y.; Kitagawa, S.; Wang, B.; Uemura, T. Hybridization of MOFs and Polymers. *Chem. Soc. Rev.* **2017**, *46*, 3108–3133. [CrossRef]
118. Kang, X.; Zhu, M. Intra-Cluster Growth Meets Inter-Cluster Assembly: The Molecular and Supramolecular Chemistry of Atomically Precise Nanoclusters. *Coord. Chem. Rev.* **2019**, *394*, 1–38. [CrossRef]
119. Wu, Z.; Yao, Q.; Zang, S.; Xie, J. Directed Self-Assembly of Ultrasmall Metal Nanoclusters. *ACS Mater. Lett.* **2019**, *1*, 237–248. [CrossRef]
120. Wu, Z.; Du, Y.; Liu, J.; Yao, Q.; Chen, T.; Cao, Y.; Zhang, H.; Xie, J. Aurophilic Interactions in the Self-Assembly of Gold Nanoclusters into Nanoribbons with Enhanced Luminescence. *Angew. Chem. Int. Ed.* **2019**, *58*, 8139–8144. [CrossRef]
121. Goswami, N.; Lin, F.; Liu, Y.; Leong, D.T.; Xie, J. Highly Luminescent Thiolated Gold Nanoclusters Impregnated in Nanogel. *Chem. Mater.* **2016**, *28*, 4009–4016. [CrossRef]
122. Nardi, M.D.; Antonello, S.; Jiang, D.-E.; Pan, F.; Rissanen, K.; Ruzzi, M.; Venzo, A.; Zoleo, A.; Maran, F. Gold Nanowired: A Linear $(Au_{25})_n$ Polymer from Au_{25} Molecular Clusters. *ACS Nano* **2014**, *8*, 8505–8512. [CrossRef] [PubMed]
123. Negishi, Y.; Nobusada, K.; Tsukuda, T. Glutathione-Protected Gold Clusters Revisited: Bridging the Gap between Gold (I)–Thiolate Complexes and Thiolate-Protected Gold Nanocrystals. *J. Am. Chem. Soc.* **2005**, *127*, 5261–5270. [CrossRef]
124. Kang, X.; Chong, H.; Zhu, M. $Au_{25}(SR)_{18}$: The Captain of the Great Nanocluster Ship. *Nanoscale* **2018**, *10*, 10758–10834. [CrossRef]
125. Luo, Z.; Nachammai, V.; Zhang, B.; Yan, N.; Leong, D.T.; Jiang, D.-E.; Xie, J. Toward Understanding the Growth Mechanism: Tracing All Stable Intermediate Species from Reduction of Au(I)–Thiolate Complexes to Evolution of Au_{25} Nanoclusters. *J. Am. Chem. Soc.* **2014**, *136*, 10577–10580. [CrossRef]
126. Dharmaratne, A.C.; Krick, T.; Dass, A. Nanocluster Size Evolution Studied by Mass Spectrometry in Room Temperature $Au_{25}(SR)_{18}$ Synthesis. *J. Am. Chem. Soc.* **2009**, *131*, 13604–13605. [CrossRef] [PubMed]
127. Parker, J.F.; Fields-Zinna, C.A.; Murray, R.W. The Story of a Monodisperse Gold Nanoparticle: $Au_{25}L_{18}$. *Acc. Chem. Res.* **2010**, *43*, 1289–1296. [CrossRef] [PubMed]
128. Shibu, E.S.; Muhammed, M.A.H.; Tsukuda, T.; Pradeep, T. Ligand Exchange of $Au_{25}SG_{18}$ Leading to Functionalized Gold Clusters: Spectroscopy, Kinetics, and Luminescence. *J. Phys. Chem. C* **2008**, *112*, 12168–12176. [CrossRef]
129. Ni, T.W.; Tofanelli, M.A.; Phillips, B.D.; Ackerson, C.J. Structural Basis for Ligand Exchange on $Au_{25}(SR)_{18}$. *Inorg. Chem.* **2014**, *53*, 6500–6502. [CrossRef]
130. Dainese, T.; Antonello, S.; Gascón, J.A.; Pan, F.; Perera, N.V.; Ruzzi, M.; Venzo, A.; Zoleo, A.; Rissanen, K.; Maran, F. $Au_{25}(SEt)_{18}$, a Nearly Naked Thiolate-Protected Au_{25} Cluster: Structural Analysis by Single Crystal X-ray Crystallography and Electron Nuclear Double Resonance. *ACS Nano* **2014**, *8*, 3904–3912. [CrossRef]
131. Jiang, D.-E.; Kühn, M.; Tang, Q.; Weigend, F. Superatomic Orbitals under Spin–Orbit Coupling. *J. Phys. Chem. Lett.* **2014**, *5*, 3286–3289. [CrossRef]
132. Liu, C.; Lin, S.; Pei, Y.; Zeng, X.C. Semiring Chemistry of $Au_{25}(SR)_{18}$: Fragmentation Pathway and Catalytic Active site. *J. Am. Chem. Soc.* **2013**, *135*, 18067–18079. [CrossRef] [PubMed]
133. Tlahuice-Flores, A.; Whetten, R.L.; Jose-Yacaman, M. Ligand Effects on the Structure and the Electronic Optical Properties of Anionic $Au_{25}(SR)_{18}$ Clusters. *J. Phys. Chem. C* **2013**, *117*, 20867–20875. [CrossRef]

134. Zhang, P. X-ray Spectroscopy of Gold–Thiolate Nanoclusters. *J. Phys. Chem. C* **2014**, *118*, 25291–25299. [CrossRef]
135. Chong, H.; Li, P.; Wang, S.; Fu, F.; Xiang, J.; Zhu, M.; Li, Y. Au_{25} Clusters as Electron-Transfer Catalysts Induced the Intramolecular Cascade Reaction of 2-nitrobenzonitrile. *Sci. Rep.* **2013**, *3*, 3214. [CrossRef]
136. Kwak, K.; Kumar, S.S.; Pyo, K.; Lee, D. Ionic Liquid of a Gold Nanocluster: A Versatile Matrix for Electrochemical Biosensors. *ACS Nano* **2014**, *8*, 671–679. [CrossRef]
137. Wu, Z.; Jiang, D.-E.; Mann, A.K.P.; Mullins, D.R.; Qiao, Z.-A.; Allard, L.F.; Zeng, C.; Jin, R.; Overbury, S.H. Thiolate Ligands as a Double-Edged Sword for CO Oxidation on CeO_2 Supported $Au_{25}(SCH_2CH_2Ph)_{18}$ Nanoclusters. *J. Am. Chem. Soc.* **2014**, *136*, 6111–6122. [CrossRef] [PubMed]
138. Stamplecoskie, K.G.; Kamat, P.V. Size-Dependent Excited State Behavior of Glutathione-Capped Gold Clusters and Their Light-Harvesting Capacity. *J. Am. Chem. Soc.* **2014**, *136*, 11093–11099. [CrossRef] [PubMed]
139. Negishi, Y. Toward the Creation of Functionalized Metal Nanoclusters and Highly Active Photocatalytic Materials Using Thiolate-Protected Magic Gold Clusters. *Bull. Chem. Soc. Jpn.* **2014**, *87*, 375–389. [CrossRef]
140. Antonello, S.; Dainese, T.; Pan, F.; Rissanen, K.; Maran, F. Electrocrystallization of Monolayer-Protected Gold Clusters: Opening the Door to Quality, Quantity, and New Structures. *J. Am. Chem. Soc.* **2017**, *139*, 4168–4174. [CrossRef]
141. Fei, W.; Antonello, S.; Dainese, T.; Dolmella, A.; Lahtinen, M.; Rissanen, K.; Venzo, A.; Maran, F. Metal Doping of $Au_{25}(SR)_{18}{}^{-}$ Clusters: Insights and Hindsights. *J. Am. Chem. Soc.* **2019**, *141*, 16033–16045. [CrossRef]
142. Hossain, S.; Imai, Y.; Motohashi, Y.; Chen, Z.; Suzuki, D.; Suzuki, T.; Kataoka, Y.; Hirata, M.; Ono, T.; Kurashige, W.; et al. Understanding and Designing One-Dimensional Assemblies of Ligand-Protected Metal Nanoclusters. *Mater. Horiz.* **2020**, *7*, 796–803. [CrossRef]
143. Chen, J.; Liu, L.; Liu, X.; Liao, L.; Zhuang, S.; Zhou, S.; Yang, J.; Wu, Z. Gold-Doping of Double-Crown Pd Nanoclusters. *Chem. Eur. J.* **2017**, *23*, 18187–18192. [CrossRef]
144. Jiang, D.-E.; Dai, S. From Superatomic $Au_{25}(SR)_{18}{}^{-}$ to Superatomic $M@Au_{24}(SR)_{18}{}^{q}$ Core–Shell Clusters. *Inorg. Chem.* **2009**, *48*, 2720–2722. [CrossRef] [PubMed]
145. Qian, H.; Jiang, D.-E.; Li, G.; Gayathri, C.; Das, A.; Gil, R.R.; Jin, R. Monoplatinum Doping of Gold Nanoclusters and Catalytic Application. *J. Am. Chem. Soc.* **2012**, *134*, 16159–16162. [CrossRef] [PubMed]
146. Yuan, P.; Zhang, R.; Selenius, E.; Ruan, P.; Yao, Y.; Zhou, Y.; Malola, S.; Häkkinen, H.; Teo, B.K.; Cao, Y.; et al. Solvent-Mediated Assembly of Atom-Precise Gold–Silver Nanoclusters to Semiconducting One-Dimensional Materials. *Nat. Commun.* **2020**, *11*, 2229. [CrossRef]
147. Zhou, K.; Qin, C.; Wang, X.-L.; Shao, K.-Z.; Yan, L.-K.; Su, Z.-M. Unexpected 1D Self-Assembly of Carbonate-Templated Sandwich-Like Macrocycle-Based $Ag_{20}S_{10}$ Luminescent Nanoclusters. *CrystEngComm* **2014**, *16*, 7860–7864. [CrossRef]
148. Chen, Z.-Y.; Tam, D.Y.S.; Zhang, L.L.-M.; Mak, T.C.W. Silver Thiolate Nano-Sized Molecular Clusters and Their Supramolecular Covalent Frameworks: An Approach Toward Pre-Templated Synthesis. *Chem. Asian J.* **2017**, *12*, 2763–2769. [CrossRef]
149. Wang, Z.; Sun, Y.-M.; Qu, Q.-P.; Liang, Y.-X.; Wang, X.-P.; Liu, Q.-Y.; Kurmoo, M.; Su, H.-F.; Tung, C.-H.; Sun, D. Enclosing Classical Polyoxometallates in Silver Nanoclusters. *Nanoscale* **2019**, *11*, 10927–10931. [CrossRef]
150. Wen, Z.-R.; Guan, Z.-J.; Zhang, Y.; Lin, Y.-M.; Wang, Q.-M. $[Au_7Ag_9(dppf)_3(CF_3CO_2)_7BF_4]_n$: A Linear Nanocluster Polymer from Molecular Au_7Ag_8 Clusters Covalently Linked by Silver Atoms. *Chem. Commun.* **2019**, *55*, 12992–12995. [CrossRef]
151. Li, Q.; Luo, T.-Y.; Taylor, M.G.; Wang, S.; Zhu, X.; Song, Y.; Mpourmpakis, G.; Rosi, N.L.; Jin, R. Molecular "Surgery" on a 23-Gold-Atom Nanoparticle. *Sci. Adv.* **2017**, *3*, e1603193. [CrossRef]
152. Li, Q.; Russell, J.C.; Luo, T.-Y.; Roy, X.; Rosi, N.L.; Zhu, Y.; Jin, R. Modulating the Hierarchical Fibrous Assembly of Au Nanoparticles with Atomic Precision. *Nat. Commun.* **2018**, *9*, 3871. [CrossRef] [PubMed]
153. AbdulHalim, L.G.; Bootharaju, M.S.; Tang, Q.; Gobbo, S.D.; AbdulHalim, R.G.; Eddaoudi, M.; Jiang, D.-E.; Bakr, O.M. $Ag_{29}(BDT)_{12}(TPP)_4$: A Tetravalent Nanocluster. *J. Am. Chem. Soc.* **2015**, *137*, 11970–11975. [CrossRef] [PubMed]
154. Wei, X.; Kang, X.; Yuan, Q.; Qin, C.; Jin, S.; Wang, S.; Zhu, M. Capture of Cesium Ions with Nanoclusters: Effects on Inter- and Intramolecular Assembly. *Chem. Mater.* **2019**, *31*, 4945–4952. [CrossRef]
155. Kitagawa, S.; Kitaura, R.; Noro, S.-I. Functional Porous Coordination Polymers. *Angew. Chem. Int. Ed.* **2004**, *43*, 2334–2375. [CrossRef]

156. Wang, Z.-Y.; Wang, M.-Q.; Li, Y.-L.; Luo, P.; Jia, T.-T.; Huang, R.-W.; Zang, S.-Q.; Mak, T.C.W. Atomically Precise Site-Specific Tailoring and Directional Assembly of Superatomic Silver Nanoclusters. *J. Am. Chem. Soc.* **2018**, *140*, 1069–1076. [CrossRef]
157. Ma, X.-H.; Wang, J.-Y.; Guo, J.-J.; Wang, Z.-Y.; Zang, S.-Q. Reversible Wide-Range Tuneable Luminescence of a Dual-Stimuli-Responsive Silver Cluster-Assembled Material. *Chin. J. Chem.* **2019**, *37*, 1120–1124. [CrossRef]
158. Alhilaly, M.J.; Huang, R.-W.; Naphade, R.; Alamer, B.; Hedhili, M.N.; Emwas, A.-H.; Maity, P.; Yin, J.; Shkurenko, A.; Mohammed, O.F.; et al. Assembly of Atomically Precise Silver Nanoclusters into Nanocluster-Based Frameworks. *J. Am. Chem. Soc.* **2019**, *141*, 9585–9592. [CrossRef]
159. Lu, S.-H.; Li, Y.; Yang, S.-X.; Zhao, R.-D.; Lu, Z.-X.; Liu, X.-L.; Qin, Y.; Zheng, L.-Y.; Cao, Q.-E. Three Silver Coordination Polymers with Diverse Architectures Constructed from Pyridine Carboxylic Hydrazide Ligands. *Inorg. Chem.* **2019**, *58*, 11793–11800. [CrossRef]
160. Wang, Z.-K.; Sheng, M.-M.; Qin, S.-S.; Shi, H.-T.; Strømme, M.; Zhang, Q.-F.; Xu, C. Assembly of Discrete Chalcogenolate Clusters into a One-Dimensional Coordination Polymer with Enhanced Photocatalytic Activity and Stability. *Inorg. Chem.* **2020**, *59*, 2121–2126. [CrossRef]
161. Xu, C.; Hedin, N.; Shi, H.-T.; Zhang, Q.-F. A Semiconducting Microporous Framework of $Cd_6Ag_4(SPh)_{16}$ Clusters Interlinked Using Rigid and Conjugated Bipyridines. *Chem. Commun.* **2014**, *50*, 3710–3712. [CrossRef]
162. Xu, C.; Sheng, M.-M.; Shi, H.-T.; Strømme, M.; Zhang, Q.-F. Interlinking Supertetrahedral Chalcogenolate Clusters with Bipyridines to Form Two-Dimensional Coordination Polymers for Photocatalytic Degradation of Organic Dye. *Dalton Trans.* **2019**, *48*, 5505–5510. [CrossRef]
163. Ghosh, A.; Mohammed, O.F.; Bakr, O.M. Atomic-Level Doping of Metal Clusters. *Acc. Chem. Res.* **2018**, *51*, 3094–3103. [CrossRef] [PubMed]
164. Bhattarai, B.; Zaker, Y.; Atnagulov, A.; Yoon, B.; Landman, U.; Bigioni, T.P. Chemistry and Structure of Silver Molecular Nanoparticles. *Acc. Chem. Res.* **2018**, *51*, 3104–3113. [CrossRef] [PubMed]
165. Chakraborty, I.; Pradeep, T. Atomically Precise Clusters of Noble Metals: Emerging Link between Atoms and Nanoparticles. *Chem. Rev.* **2017**, *117*, 8208–8271. [CrossRef]
166. Li, X.-Y.; Su, H.-F.; Xu, J. A 2D Layer Network Assembled from an Open Dendritic Silver Cluster $Cl@Ag_{11}N_{24}$ and an N-Donor Ligand. *Inorg. Chem. Front.* **2019**, *6*, 3539–3544. [CrossRef]
167. Pearson, R.G. Hard and Soft Acids and Bases. *J. Am. Chem. Soc.* **1963**, *85*, 3533–3539. [CrossRef]
168. Huang, R.-W.; Wei, Y.-S.; Dong, X.-Y.; Wu, X.-H.; Du, C.-X.; Zang, S.-Q.; Mak, T.C.W. Hypersensitive Dual-Function Luminescence Switching of a Silver-Chalcogenolate Cluster-Based Metal–Organic Framework. *Nat. Chem.* **2017**, *9*, 689–697. [CrossRef]
169. Huang, R.-W.; Dong, X.-Y.; Yan, B.-J.; Du, X.-S.; Wei, D.-H.; Zang, S.-Q.; Mak, T.C.W. Tandem Silver Cluster Isomerism and Mixed Linkers to Modulate the Photoluminescence of Cluster-Assembled Materials. *Angew. Chem. Int. Ed.* **2018**, *57*, 8560–8566. [CrossRef]
170. Du, X.-S.; Yan, B.-J.; Wang, J.-Y.; Xi, X.-J.; Wang, Z.-Y.; Zang, S.-Q. Layer-Sliding-Driven Crystal Size and Photoluminescence Change in a Novel SCC-MOF. *Chem. Commun.* **2018**, *54*, 5361–5364. [CrossRef]
171. Cao, M.; Pang, R.; Wang, Q.-Y.; Han, Z.; Wang, Z.-Y.; Dong, X.-Y.; Li, S.-F.; Zang, S.-Q.; Mak, T.C.W. Porphyrinic Silver Cluster Assembled Material for Simultaneous Capture and Photocatalysis of Mustard-Gas Simulant. *J. Am. Chem. Soc.* **2019**, *141*, 14505–14509. [CrossRef]
172. Wang, Y.-M.; Zhang, J.-W.; Wang, Q.-Y.; Li, H.-Y.; Dong, X.-Y.; Wang, S.; Zang, S.-Q. Fabrication of Silver Chalcogenolate Cluster Hybrid Membranes with Enhanced Structural Stability and Luminescence Efficiency. *Chem. Commun.* **2019**, *55*, 14677–14680. [CrossRef] [PubMed]
173. Wu, T.; Yin, D.; Hu, X.; Yang, B.; Liu, H.; Xie, Y.-P.; Liu, S.-X.; Ma, L.; Gao, G.-G. A Disulfur Ligand Stabilization Approach to Construct a Silver(I)-Cluster-Based Porous Framework as a Sensitive SERS Substrate. *Nanoscale* **2019**, *11*, 16293–16298. [CrossRef]
174. Su, W.; Hong, M.; Jiang, F.; Liu, H.; Zhou, Z.; Wu, D.; Mak, T.C.W. A Cleavage of the S–C Bond in 2-aminothiophenal: Synthesis and Crystal Structure of $[Ag_{11}(\mu_5\text{-}S)(\mu_4\text{-}S_2CNEt_2)_6(\mu_3\text{-}S_2CNEt_2)_3]$. *Polyhedron* **1996**, *15*, 4047–4051. [CrossRef]
175. Chen, S.; Du, W.; Qin, C.; Liu, D.; Tang, L.; Liu, Y.; Wang, S.; Zhu, M. Assembly of the Thiolated $[Au_1Ag_{22}(S\text{-}Adm)_{12}]^{3+}$ Superatom Complex into a Framework Material through Direct Linkage by SbF_6^- Anions. *Angew. Chem. Int. Ed.* **2020**, *59*, 7542–7547. [CrossRef]
176. Dong, X.-Y.; Huang, H.-L.; Wang, J.-Y.; Li, H.-Y.; Zang, S.-Q. A Flexible Fluorescent SCC-MOF for Switchable Molecule Identification and Temperature. *Chem. Mater.* **2018**, *30*, 2160–2167. [CrossRef]

177. Wei, Z.; Wu, X.-H.; Luo, P.; Wang, J.-Y.; Li, K.; Zang, S.-Q. Matrix Coordination Induced Emission in a Three-Dimensional Silver Cluster-Assembled Material. *Chem. Eur. J.* **2019**, *25*, 2750–2756. [CrossRef]
178. Wu, X.-H.; Luo, P.; Wei, Z.; Li, Y.-Y.; Huang, R.-W.; Dong, X.-Y.; Li, K.; Zang, S.-Q.; Tang, B.Z. Guest-Triggered Aggregation-Induced Emission in Silver Chalcogenolate Cluster Metal–Organic Frameworks. *Adv. Sci.* **2019**, *6*, 1801304. [CrossRef]
179. Lei, Z.; Pei, X.-L.; Jiang, Z.-G.; Wang, Q.-M. Cluster Linker Approach: Preparation of a Luminescent Porous Framework with NbO Topology by Linking Silver Ions with Gold(I) Clusters. *Angew. Chem. Int. Ed.* **2014**, *53*, 12771–12775. [CrossRef]
180. Nguyen, T.-A.D.; Jones, Z.R.; Goldsmith, B.R.; Buratto, W.R.; Wu, G.; Scott, S.L.; Hayton, T.W. A Cu_{25} Nanocluster with Partial Cu(0) Character. *J. Am. Chem. Soc.* **2015**, *137*, 13319–13324. [CrossRef]
181. Cook, A.W.; Jones, Z.R.; Wu, G.; Scott, S.L.; Hayton, T.W. An Organometallic Cu_{20} Nanocluster: Synthesis, Characterization, Immobilization on Silica, and "Click" Chemistry. *J. Am. Chem. Soc.* **2018**, *140*, 394–400. [CrossRef]
182. Nguyen, T.-A.D.; Jones, Z.R.; Leto, D.F.; Wu, G.; Scott, S.L.; Hayton, T.W. Ligand-Exchange-Induced Growth of an Atomically Precise Cu_{29} Nanocluster from a Smaller Cluster. *Chem. Mater.* **2016**, *28*, 8385–8390. [CrossRef]
183. Chakrahari, K.K.; Liao, J.-H.; Kahlal, S.; Liu, Y.-C.; Chiang, M.-H.; Saillard, J.-Y.; Liu, C.W. $[Cu_{13}\{S_2CN^nBu_2\}_6(\text{acetylide})_4]^+$: A Two-Electron Superatom. *Angew. Chem. Int. Ed.* **2016**, *55*, 14704–14708. [CrossRef] [PubMed]
184. Negishi, Y.; Kurashige, W.; Niihori, Y.; Nobusada, K. Toward the Creation of Stable, Functionalized Metal Clusters. *Phys. Chem. Chem. Phys.* **2013**, *15*, 18736–18751. [CrossRef]
185. Puls, A.; Jerabek, P.; Kurashige, W.; Förster, M.; Molon, M.; Bollermann, T.; Winter, M.; Gemel, C.; Negishi, Y.; Frenking, G.; et al. A Novel Concept for the Synthesis of Multiply Doped Gold Clusters $[(M@Au_nM'_m)L_k]^{q+}$. *Angew. Chem. Int. Ed.* **2014**, *53*, 4327–4331. [CrossRef]
186. Kurashige, W.; Niihori, Y.; Sharma, S.; Negishi, Y. Recent Progress in the Functionalization Methods of Thiolate-Protected Gold Clusters. *J. Phys. Chem. Lett.* **2014**, *5*, 4134–4142. [CrossRef]
187. Kurashige, W.; Niihori, Y.; Sharma, S.; Negishi, Y. Precise Synthesis, Functionalization and Application of Thiolate-Protected Gold Clusters. *Coord. Chem. Rev.* **2016**, *320–321*, 238–250. [CrossRef]
188. Niihori, Y.; Hossain, S.; Kumar, B.; Nair, L.V.; Kurashige, W.; Negishi, Y. Perspective: Exchange Reactions in Thiolate-Protected Metal Clusters. *APL Mater.* **2017**, *5*, 053201. [CrossRef]
189. Niihori, Y.; Hossain, S.; Sharma, S.; Kumar, B.; Kurashige, W.; Negishi, Y. Understanding and Practical Use of Ligand and Metal Exchange Reactions in Thiolate-Protected Metal Clusters to Synthesize Controlled Metal Clusters. *Chem. Rec.* **2017**, *17*, 473–484. [CrossRef]
190. Kumar, B.; Kawawaki, T.; Shimizu, N.; Imai, Y.; Suzuki, D.; Hossain, S.; Nair, L.V.; Negishi, Y. Gold Nanoclusters as Electrocatalysts: Size, Ligands, Heteroatom Doping, and Charge Dependences. *Nanoscale* **2020**, *12*, 9969–9979. [CrossRef]
191. Zhang, H.; Watanabe, T.; Okumura, M.; Haruta, M.; Toshima, N. Catalytically Highly Active Top Gold Atom on Palladium Nanocluster. *Nat. Mater.* **2012**, *11*, 49–52. [CrossRef]
192. Kusada, K.; Yamauchi, M.; Kobayashi, H.; Kitagawa, H.; Kubota, Y. Hydrogen-Storage Properties of Solid-Solution Alloys of Immiscible Neighboring Elements with Pd. *J. Am. Chem. Soc.* **2010**, *132*, 15896–15898. [CrossRef] [PubMed]
193. Akutsu, M.; Koyasu, K.; Atobe, J.; Hosoya, N.; Miyajima, K.; Mitsui, M.; Nakajima, A. Experimental and Theoretical Characterization of Aluminum-Based Binary Superatoms of $Al_{12}X$ and Their Cluster Salts. *J. Phys. Chem. A* **2006**, *110*, 12073–12076. [CrossRef] [PubMed]
194. Negishi, Y.; Nakamura, Y.; Nakajima, A.; Kaya, K. Photoelectron Spectroscopy of Gold–Silver Binary Cluster Anions ($Au_nAg_m^-$; $2 \leq n + m \leq 4$). *J. Chem. Phys.* **2001**, *115*, 3657. [CrossRef]